BremHLR
Kompetenzzentrum für Höchstleistungsrechnen Bremen

Statusbericht 2017
des
Kompetenzzentrums
für
Höchstleistungsrechnen Bremen
–BremHLR–

Bremen, Juli 2018

Universität Bremen
JACOBS UNIVERSITY
ALFRED-WEGENER-INSTITUT HELMHOLTZ-ZENTRUM FÜR POLAR- UND MEERESFORSCHUNG
Hochschule Bremerhaven

HLRN
Norddeutscher Verbund für Hoch- und Höchstleistungsrechnen

www.bremhlr.uni-bremen.de

Das Berichtsjahr 2017 in Stichpunkten

- Stabile Bremer Nutzung der Ressourcen des Norddeutschen Verbunds für Hoch- und Höchstleistungsrechnen (HLRN)
- Erfolgreicher 12. BremHLR Workshop zur Einführung in die parallele Programmierung
- Stabiler Produktionsbetrieb des derzeitigen Rechnersystems HLRN-III
- Beschaffungsverfahren des Nachfolgesystems HLRN-IV

Inhaltsverzeichnis

1 BremHLR: Aufgaben und organisatorische Struktur

1.1 Aufgaben

Das Land Bremen beteiligt sich am Norddeutschen Verbund für Hoch- und Höchstleistungsrechnen – HLRN – um an dem rasanten Fortschritt der Computer- und Softwaretechnologie Teil zu haben. Das Kompetenzzentrum für Höchstleistungsrechnen Bremen – BremHLR – unterstützt dazu Wissenschaftler im wissenschaftlichen Rechnen insbesondere im Land Bremen. Die Fachberater des BremHLR leisten Unterstützung für Projekte sowohl in der Konzeption, der Antragstellung als auch der Durchführung. Der Schwerpunkt der Unterstützung liegt hierbei auf Projekten auf dem HLRN-System. Seit 2005 wurde die Betreuung aber auch auf Rechenprojekte an den nationalen Höchstleistungsrechenzentren wie z. B. dem Jülich Supercomputing Centre (JSC) ausgeweitet.

Als Bestandteil im Kompetenznetzwerk des HLRN beteiligt sich BremHLR unter anderem an der fachspezifischen Nutzerberatung, der Pflege von Software-Paketen und der Veranstaltung überregionaler Nutzerworkshops. Die Geschäftsstelle des BremHLR ist an der Universität Bremen im Zentrum für Technomathematik angesiedelt.

Das BremHLR wurde am 1. Juli 2003 als Kooperation zwischen der Universität Bremen (UB), der Jacobs University Bremen (JUB) und dem Alfred-Wegener-Institut für Polar- und Meeresforschung (AWI) gegründet. Seit April 2008 ist auch die Hochschule Bremerhaven (HBHV) Kooperationspartner des BremHLR. Das Kompetenzzentrum wird von den beteiligten Kooperationspartnern sowie der Bremer Senatorin für Wissenschaft, Gesundheit und Verbraucherschutz (SfWGV) anteilig finanziell getragen. Seit Januar 2014 ist die JUB als ideelles Mitglied beitragsfrei gestellt.

1.2 Struktur

Dem Lenkungsausschuss des BremHLR als oberstes beschlussfassendes und steuerndes Gremium gehören in der Berichtsperiode folgende Vertreter der kooperierenden Einrichtungen an. Im Einzelnen sind dies:

- Prof. Dr. Alfred Schmidt (UB/Zentrum für Technomathematik ZeTeM)
- Prof. Dr. Wolfgang Hiller (AWI/Rechenzentrum, UB/FB3)
- Prof. Dr. Ulrich Kleinekathöfer (JUB)
- Prof. Dr. Stephan Frickenhaus (HBHV)
- Helmuth Wolf (SfWGV)

Die fachspezifische Betreuung der Projekte am Norddeutschen Verbund für Hoch- und Höchstleistungsrechnen (HLRN) sowie von Projekten an anderen nationalen Höchstleistungsrechenzentren wird von den Fachberatern des BremHLR geleistet, die ebenfalls den Einrichtungen der Kooperationspartner angehören. Im Berichtszeitraum waren folgende Fachberater tätig:

- Dr. Lars Nerger (AWI/Rechenzentrum, UB/ZeTeM, Leiter Geschäftsstelle)
- Thorsten Coordes (UB/ZARM)
- Dr. Achim Geleßus (JUB/CLAMV)
- Dr. Natalja Rakowsky (AWI/Rechenzentrum)

Die Geschäftsstelle ist verantwortlich für die Organisation der Workshops (siehe Abschnitt Veranstaltungen) und die Unterstützung der Nutzer, insbesondere im Antragsverfahren. Das Sekretariat der Geschäftsstelle wird betreut von

- Julitta von Deetzen.

2 Tätigkeitsprofil des BremHLR im Berichtszeitraum

2.1 Unterstützung der HLRN-Nutzung im Land Bremen

Ein Schwerpunkt der Aktivitäten des BremHLR lag auch in diesem Berichtszeitraum in der Unterstützung der HLRN-Nutzung. Neben den Tätigkeiten von Prof. Dr. Wolfgang Hiller als Mitglied der Technischen Kommission sowie Prof. Dr. Alfred Schmidt als Mitglied des Wissenschaftlichen Ausschusses bestand die Unterstützung des HLRN durch das BremHLR hauptsächlich in der Fachberatung für Bremer Projekte am HLRN von der Antragstellung bis zur Begleitung rechenintensiver Projekte während der gesamten Projektlaufzeit.

Eine wesentliche Aufgabe im Berichtsjahr war die weitere Unterstützung der Bremer Nutzer des HLRN bei der effizienten Nutzung des HLRN-III Hochleistungsrechnersystems. Des Weiteren waren Mitglieder des BremHLR am Beschaffungsverfahren des Nachfolgesystems HLRN-IV beteiligt, dass als EU-weite Ausschreibung durchgeführt wurde. Das System soll voraussichtlich in 2018 installiert werden, die Beschaffung hat aufgrund der Größe des Rechnersystems aber einige Vorlaufzeit. So haben Mitglieder des BremHLR an der Auswertung der Benchmark-Ergebnisse und an Verhandlungsterminen teilgenommen.

2.2 Weitere Aktivitäten des BremHLR

Im Veranstaltungsjahr 2017 wurde vom BremHLR der *12. Workshop zur Einführung in die parallele Programmierung mit MPI und OpenMP* organisiert und durchgeführt. Mit 39 Teilnehmern war dieser Workshop wieder sehr gut besucht.

Der Workshop wurde in der Zeit vom 9. bis zum 13. Januar 2017 an der JUB abgehalten. Als Referent konnte wie bereits bei bisherigen Workshops Dr. Hinnerk Stüben vom Regionalen Rechenzentrum der Universität Hamburg gewonnen werden, der den Workshop gemeinsam mit dem BremHLR-Fachberater Dr. Lars Nerger abhielt. Für die Studenten der JUB wurde der Workshop auch wieder als offizielle Lehrveranstaltung angeboten. Durch die Bearbeitung eines abschließend bewerteten Programmierprojekts konnten die Studenten Kreditpunkte für ihr Bachelor- und Masterstudium erlangen.

Der sehr gute Zuspruch und der große Erfolg der Veranstaltungen zeigt deutlich den dringenden Bedarf zur Ausbildung im Hoch- und Höchstleistungsrechnen und gibt Anlass dazu solche Workshops auch weiterhin als regelmäßige Ausbildungs- und Schulungs-maßnahme anzubieten.

Neben dem Workshop zur Einführung in die parallele Programmierungbeteiligten sich Fachberater des BremHLR an Fachberaterworkshops des HLRN-Kompetenznetzwerks in Göttingen und Hamburg. Bei diesen Workshops wurden unterschiedliche Themen des HLRN-Betriebs und der Nutzerbetreuung besprochen. Eine Übersicht über die Veranstaltungen ist in Abschnitt 4 zu finden.

3 Statistische Angaben zu den Bremer Höchstleistungsprojekten

Auch im Jahr 2017wurde der HLRN intensiv durch Bremer Projekte genutzt. Im Jahresdurchschnitt wurde auf dem HLRN-III System ein prozentualer Anteil von 16,3 % an der gesamten am HLRN-III abgenommenen Rechenleistung erreicht. Dieses liegt deutlich über dem investiven Anteil von etwa 3,5% des Landes Bremen am HLRN. Über die gesamte Laufzeit seit Einrichtung des HLRN-Verbunds wurde durch Bremer Projekte ein Anteil von 7,8% der verfügbaren Rechenzeit abgenomen.

Wie schon das Jahr 2016 war auch das Jahr 2017durch einen stabilen Betrieb des HLRN-III Systems ohne längere Ausfallzeiten geprägt.

Insgesamt wurden im Jahr 2017 etwa 7.000.000 NPL[1] durch Bremer Projekte am HLRN-III System abgenommen. Abbildung 3.1 zeigt den monatlichen Verbrauch der Bremer Projekte am HLRN-III System. Deutlich sichbar ist die starke Zunahme der genutzen Rechenzeit die durch die Verfügbarkeit der zweiten Ausbaustufe von HLRN-III im Jahr 2015 möglich wurde und sich im Jahr 2016 fortgesetzt hat. Im Jahr 2017 hat sich die genutzte Rechenzeit dann stabilisiert.

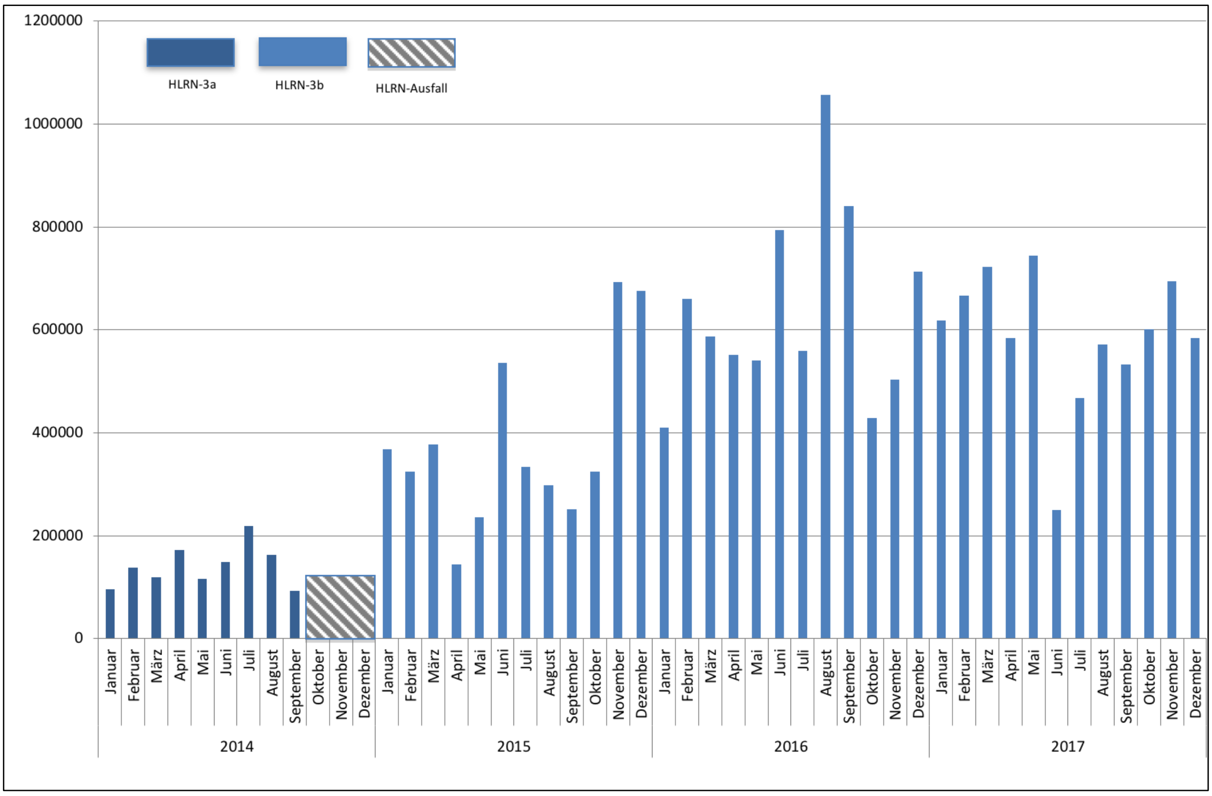

Abbildung 3.1: Monatliche Rechenzeitnutzung der Bremer HLRN-Großprojekteseit Januar 2014 auf dem HLRN-III System in der HLRN-Leistungseinheit NPL. Die Farben zeigen die Verfügbarkeit der unterschiedlichen Ausbaustufen des HLRN-Systems. Von Oktober bis Dezember 2014 waren die HLRN-Systeme nicht bzw. nur teilweise nutzbar.

---

[1] Norddeutsche Parallelrechner-Leistungseinheit: Auf den Systemen der ersten Ausbaustufe des HLRN-III entspricht 1 NPL einer halben CPU-h auf einem Knoten mit je 24 Prozessorkernen. Auf den Systemen der zweiten Ausbaustufe entspricht die Nutzung einer Knotens über eine Stunde 2,4 NPL.

Eine Übersicht zu allen vom BremHLR betreuten Projekten gibt Tabelle 3.1. Im Jahr 2017 wurden vom BremHLR 40 Projekte am HLRN betreut. Die Projekte werden von über 100 akkreditierten Nutzern durchgeführt. 15 neue Projekte mit teilweise sehr großem Rechenzeitbedarf wurden im Jahr 2017 beantragt und vom Wissenschaftlichen Ausschuss des HLRN bewilligt. 13 Projekte wurden im Berichtsjahr beendet.

4 Veranstaltungen mit Beteiligung des BremHLR

11. BremHLR-Workshop *Einführung in die Programmierung mit MPI und OpenMP*

Veranstalter: BremHLR

Datum: 9. – 13. Januar 2017

Ort: Jacobs University Bremen

Beschreibung: In dem Workshop wurden die Grundlagen der parallelen Programmierung vermittelt. Der Schwerpunkt lag auf den Programmiermodellen MPI und OpenMP. Praktische Übungen bildeten einen wesentlichen Teil des Workshops.

Referenten: Dr. Hinnerk Stüben (Regionales Rechenzentrum der Universität Hamburg) und Dr. Lars Nerger (BremHLR).

Teilnehmerzahl: 39

Teilnehmende Institutionen: AWI, BSH, GEOMAR, IOW, JUB, UB (Informatik, MARUM, Physik, TZI), TU Braunschweig, Uni Göttingen, Uni Hamburg, Uni Hannover, Uni Oldenburg, Uni Potsdam

31. HLRN-Fachberater-Workshop

Veranstalter: Uni Oldenburg

Datum: 26. – 27. April 2017

Ort: Uni Oldenburg

Teilnehmerzahl: 22

Teilnehmende Institutionen: BremHLR (ZARM), BTU Cottbus-Senftenberg, GWDG Göttingen, IOW, RRZ Uni Hamburg, LUIS Uni Hannover, TU Hamburg-Harburg, Uni Kiel, Uni Oldenburg, Uni Rostock, ZIB

32. HLRN-Fachberater-Workshop

Veranstalter: Uni Potsdam

Datum: 28. – 29. November 2017

Ort: Uni Potsdam

Teilnehmerzahl: 28

Teilnehmende Institutionen: BremHLR (AWI, ZARM), BTU Cottbus-Senftenberg, GWDG Göttingen, HU Berlin, IOW, LUIS Uni Hannover, RRZ Uni Hamburg, Uni Hamburg, Uni Rostock, Uni Kiel, Uni Potsdam, ZIB

Tabelle 3.1: Übersicht der Bremer HPC-Projekte, die innerhalb des Berichtszeitraums vom BremHLR betreut wurden. Status: F = Fortsetzung, E = Erstantrag; kNPL: Kontingent in tausend NPL im Jahr 2017

Kennung	Projektleiter	Institut	Laufzeit	kNPL	Status
hbc00012	Prof. Dr. L. Colombi-Ciacchi	UB/BCCMS	IV/12 – I/17	55	F
hbc00013	Dr. J. Larrucea	UB/BCCMS	IV/12 – I/17	60	F
hbc00017	Prof. Dr. P. Deák	UB/BCCMS	IV/15 – IV/17	160	F
hbc00020	Dr. M. Delle Piane	UB/BCCMS	III/16 – III/17	80	E
hbc00023	Dr. M. Delle Piane	UB/BCCMS	III/17 – II/18	80	E
hbc00025	Prof. Dr. L. Colombi-Ciacchi	UB/BCCMS	III/17 – II/18	116	E
hbi00024	Dr.-Ing. R. Groll	UB/ZARM	II/14 – III/17	96	F
hbi00026	Dr.-Ing. R. Groll	UB/ZARM	II/15 – I/18	104	F
hbi00027	Dr.-Ing. R. Groll	UB/ZARM	IV/15 – II/18	120	F
hbi00030	Dr.-Ing. R. Groll	UB/ZARM	II/16 – I/18	105	E
hbi00032	Dr.-Ing. R. Groll	UB/ZARM	III/16 – II/17	80	E
hbi00033	Prof. Dr. M. Avila	UB/ZARM	I/17 – IV/17	100	E
hbi00035	Prof. Dr. M. Avila	UB/ZARM	I/17 – I/18	460	E
hbi00036	Prof. Dr. U. Fritsching	UB/FB4	II/17 – I/18	60	E
hbi00037	Prof. Dr. U. Fritsching	UB/FB4	II/17 – I/18	90	E
hbk00018	Dr. K. Weigel	UB/IUP	I/11 – III/17	230	F
hbk00028	Prof. Dr. P. Lemke	AWI & UB	IV/11 – I/17	20	F
hbk00032	Prof. Dr. T. Jung	AWI & UB	II/12 – II/18	1100	F
hbk00034	Prof. Dr. T Kanzow	AWI & UB	III/13 – III/18	820	F
hbk00038	Prof. Dr. T. Kanzow	AWI & UB	III/14 – III/18	265	F
hbk00042	Prof. Dr. G. Lohmann	AWI & UB	I/15 – IV/17	400	F
hbk00044	Prof. Dr. T. Jung	AWI & UB	II/15 – II/18	383	F
hbk00045	Dr. A. Rozanov	UB/IUP	IV/15 – III/18	136	F
hbk00055	Prof. Dr. A. Bracher	AWI & UB	III/16 – III/18	122	E
hbk00056	Prof. Dr. M. Schulz	UB/MARUM	III/16 – II/17	246	E
hbk00057	Dr. A. Rozanov	UB/IUP	I/17 – IV/18	300	E
hbk00058	Prof. Dr. M. Schulz	UB/MARUM	III/17 – II/18	315	E
hbk00059	Prof. Dr. M. Schulz	UB/MARUM	III/17 – II/18	120	E
hbk00060	Prof. Dr. G. Lohmann	AWI & UB	III/17 – II/18	316	E
hbk00061	Prof Dr. M. Schulz	UB/MARUM	IV/17 – III/18	15	E
hbk00062	Dr. A. Rozanov	UB/IUP	IV/17 – III/18	150	E
hbp00028	Prof. Dr. T. Frauenheim	UB/BCCMS	III/15 – II/17	44	F
hbp00029	Dr. M. Lorke	UB/Physik	IV/15 – I/18	323	F
hbp00030	Prof. Dr. T. Wehling	UB/Physik	IV/15 – III/17	90	F
hbp00034	Dr. B. Shao	UB/BCCMS	I/16 – I/17	41	E
hbp00035	Prof. Dr. C. Lämmerzahl	UB/ZARM	I/16 – I/18	120	F
hbp00038	Dr. M. Lorke	UB/Physik	II/16 – II/18	171	F
hbp00041	Prof. Dr. C. Lämmerzahl, Prof. Dr. S. Rosswog	UB/ZARM	I/17 – IV/17	180	E
hbp00045	Prof. Dr. T. Wehling	UB/Physik	II/17 – I/18	81	E
hbp00046	Prof. Dr. T. Wehling	UB/Physik	IV/17 – III/18	17	E

5 Projektberichte[2]

5.1 HLRN Projects of the Hybrid Materials Interfaces Group (HMI)

Technical Details:

HLRN Project ID:	**hbc00012**
Title:	All-atom moleculardynamic investigations of the adhesion mechanisms at the contact interface of TiO_2 nanoparticles in films and aggregates
Run time:	IV/2012 – I/2017
Project Leader:	Prof. Dr. Lucio Colombi Ciacchi
Project Scientists:	Jens Laube, Valentin Baric, Dr. Julian Schneider

HLRN Project ID:	**hbc00013**
Title:	Fabrication of multishaped magnetic structures via a knowledge based biomimetic approach
Run time:	IV/2012 – I/2017
Project Leader:	Dr. Susan Köppen
Project Scientists:	Steffen Lid

HLRN Project ID:	**hbc00020**
Title:	Silica: both friend and foe. Is molecular regognition the answer?
Run time:	III/2016 – III/2017
Project Leader:	Dr. Massimo Delle Piane
Project Scientists:	Prof. Dr. Lucio Colombi Ciacchi, Lennart v. Germersheim, Joschka Cors, Sebastian Potthoff

---

[2] Für den Inhalt der Projektberichte sind ausschließlich die genannten Projektleiter bzw. die Projektbearbeiter verantwortlich.

HLRN Project ID: **hbc00023**

Title: Adsorption of binding peptides on ZnO. Towards a quantitative understanding of organic-inorganic interactions

Run time: III/2017 – II/2018

Project Leader: Dr. Massimo Delle Piane

Project Scientists: Monika Michaelis, Steffen Lid, André Wark

HLRN Project ID: **hbc00025**

Title: Polymer hybrid materials – Atomistic Modelling of the Formation of a Thermo-set/Thermoplastic Interphase during Co-Curing

Run time: III/2017 – II/2018

Project Leader: Prof. Dr. Lucio Colombi Ciacchi

Project Scientists: Dr. Massimo Delle Piane, Magdalena Laurien, Nils Hildebrand

Affiliation: Hybrid Materials Interfaces Group, Bremen Center for Computational Materials Science, Faculty of Production Engineering, University of Bremen, Germany

hbc00020: Silica: both friend and foe. Is molecular regognition the answer?

Overview

The interaction of silica (SiO_2) with biological systems is complex and contradictory. On the one hand, silica is at the basis of several biomineralization processes (e.g. in sponges). On the other hand, silica nanoparticles and dust may lead to silicosis and, at the cellular level, hemolysis. These toxic responses are strongly dependent on the silica polymorph and their root causes are still under debate. We hypothesize that both silica biomineralization and silica-induced nanotoxicity could be related to similar mechanisms of molecular recognition between epitopes of the cellular membranes with specific patterns on the SiO2 particles' surfaces. This project aim is to investigate these interactions using all-atom MD simulations, coupled to techniques that enable a computational prediction of free energy profiles across hybrid interfaces, to achieve an atomistic picture of the interactions between different types of silica nanoparticles and the membrane of human cells.

Current results

This project has run through its first application period. We modeled cell membranes of various compositions targeting a realistic representation of the lipid composition of a red blood cell membrane, given its relevance to nano-toxicology, with particular interest in the effect of cholesterol. Models for small silica clusters of increasing size and complexity were generated, through extraction from an amorphous silica bulk. Well-tempered metadynamics (wt-metaD) allowed to overcome the time-scale limits of standard all-atom MD and to sample the full configurational space of the silica nanoclusters (in both the water and lipid phases and at the interface), providing free energy profiles of the molecules across the lipid bilayer. These profiles allowed us, in turn, to predict the energetics of the silica-membrane interaction, in the form of crossing barrier, $\Delta G^{\ddagger}$, free energy of partition, ΔG_{part}, between the water and lipid phases, and free energy of adsorption, ΔG_{ads}, at the water-lipid interface, also investigating their dependence on particle size, particle charge and membrane composition.These results showed that silica nanoclusters are highly hydrated hydrophilic molecules that must overcome high barriers to cross the water-lipid interface already at nuclearities of a few Si atoms. However, the barriers encountered by individual water or silica molecules are of nearly equal height, strongly suggesting that either can cross the membrane with roughly the same probability. Analyzing the trajectories, we found evidence of a possible direct translocation mechanism (Fig. 1), in which silica nanoclusters elicit both local and large-scale effects on the membrane dynamics and stability. This gives hints on possible pathways for silica nanotoxicity based on nanoparticle-induced membrane perforation.

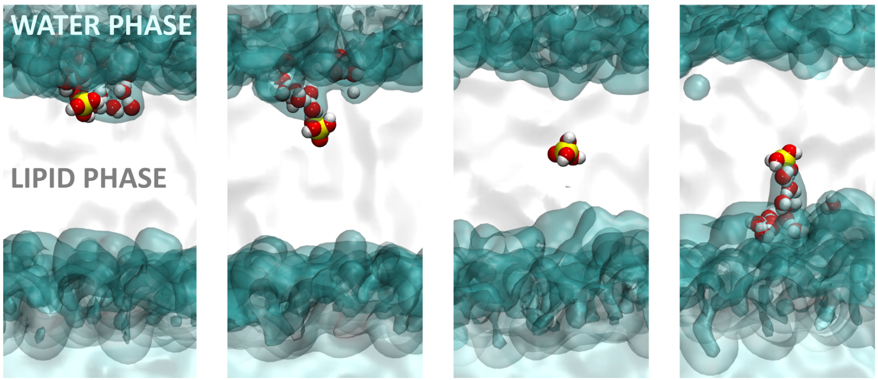

Fig. 1: Snapshots displaying the crossing of a lipid bilayer by silicicacid. The water and lipid phases are visualized as transparent isosurfaces (cyan and white, respectively), while the silica molecule and water molecules close to it are reported in ball and stick models.

Outlook

Further work is needed to extend these simulations to larger nanoparticles models with varied morphologies, taking into account in particular both Stöber-like and fumed-like silica. Finally, other components of the cell membrane should be included in the simulations, with particular reference to membrane proteins, that may play an important role in nanoparticle/cell interactions, especially when nanoparticle incorporation occurs via endocytosis rather than passive translocation.

hbc00023: Adsorption of binding peptides on ZnO. Towards a quantitative understanding of organic-inorganic interactions

Overview

The specific binding of peptides to biomolecular receptors is key to the regulation of biological processes such as cell adhesion or antibody recognition. The concept of molecular recognition can be extended to the field of materials science with individual peptide sequences that selectively bind to inorganic mineral phases. Extending this concept further, sequences that recognize certain materials classes, inorganic compounds or even crystallographic facets of the same material have been identified, leading to highly promising applications in bio-nanotechnology. In this project we focus on zinc oxide (ZnO), aiming at a quantitative determination of the binding characteristics (binding free energy, adhesion forces) of ZnO-binding peptides interacting with the non-polar (10-10) surface of ZnO. The results will be interpreted in terms of both the primary peptide structures and of changes of peptide conformation (secondary structure) after adsorption.

Current results

This project is running through its first application period. We prepared realistic models of the ZnO(10-10)/MeOHand the ZnO(10-10)/H_2O, interfaces. We then focused on five different peptides in our simulations, which have been identified by our experimental coworker using Phage display. The five ZnO-binding peptide structures were created using *De novo* secondary structure prediction tools. Their conformational space was investigated through Molecular Dynamics coupled with Replica Exchange with Solute Tempering (REST) in both explicit MeOH and water, to investigate the influence of the different solvent polarity on the structural ensemble of the peptides. We then used these trajectories to calculate the CD spectra for comparison with experiments and reconstruct the Boltzmann distribution to analyze the secondary structure of the peptides in solution.

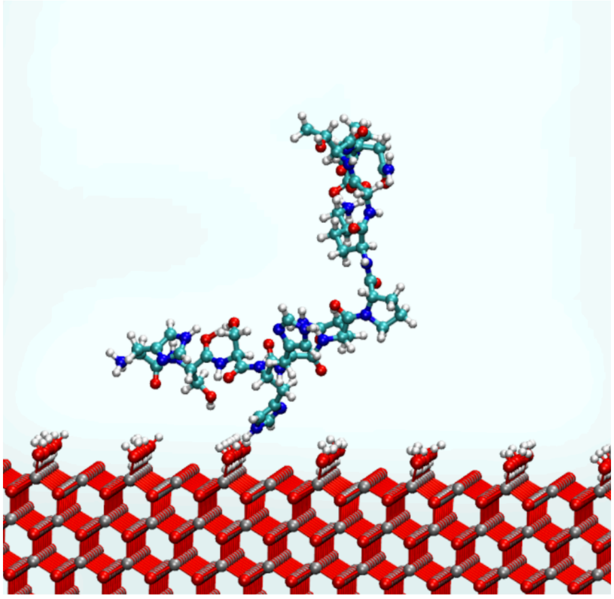

Fig. 2: Input structure of a zinc oxide binding peptide approaching the ZnO(10-10) surface in water.

Outlook

The present step consists in placing the peptide structures above the ZnO (10-10) surface (Fig. 2). A modeling method based on REST in combination with Metadynamics (RESTMetaD) is employed, where the collective variable is the distance between surface and peptide, to extract and estimation of ΔG_{ads} for the five binding peptides, to compare with experimental values, obtained in our group with both single molecule force spectroscopy and fluecescence-based methods. We believe that these simulations will help us elucidate the influence of the primary peptide structures and of changes of peptide conformation (secondary structure) upon the interaction with the non-polar ZnO surface (10-10) and allow the quantification of the interactions at the interface.

hbc00025: Polymer hybrid materials – Atomistic Modelling of the Formation of a Thermo-set/Thermoplastic Interphase during Co-Curing

Overview

The high cost of joining fiber-reinforced plastics is the driving motivation for development of new joining techniques. A promising joining technique is thermoplastic welding, that can also be applied to thermosetting polymers if they are covered with a thermoplastic layer. The thermoplastic layer is applied to the thermosetting polymer via co-curing. However, the molecular mechanisms guiding the adhesion strength upon co-curing are not yet well understood. In this project we aimed at developing a procedure for creating a thermoset/thermoplastic interphase with classical molecular dynamics simulations, by creating atomistic models of a thermoplastic and an epoxy system, testing their thermo-mechanical properties and then creating slabs of the materials, stacking them in one simulation supercell allowing interdiffusion and the formation of an interphase.

Current results

This project is running through its first application period. A thermoset/thermoplastic interphase was modelled via all-atom classical MD techniques. As example system, a combination of a thermosetting diamino-epoxy resin and the thermoplastic polymer polyvinylidene fluoride (PVDF) was chosen to reproduce a typical system for thermoset welding. The bulk systems were produced using packing and densification algorithms and equilibrated with a several-step

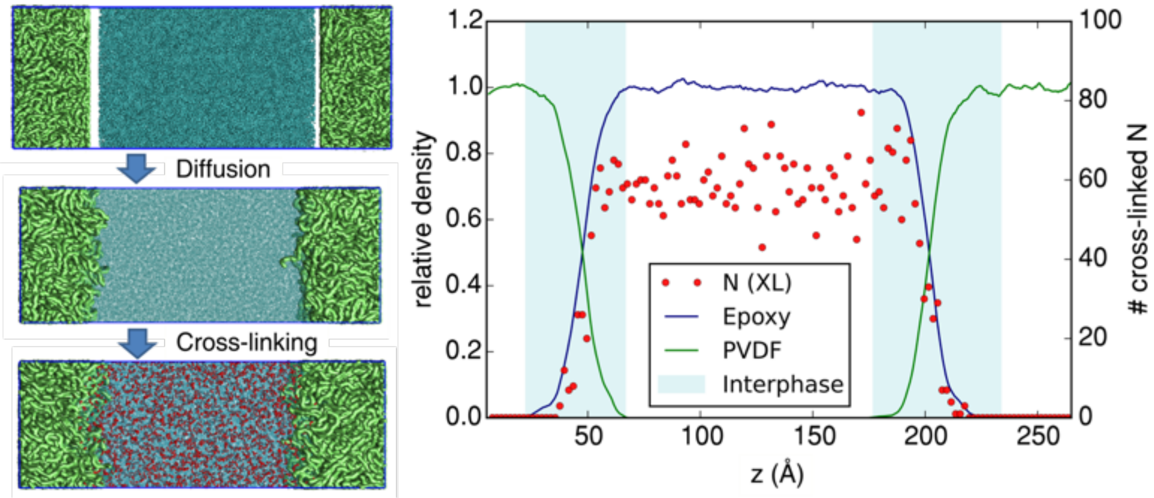

Fig. 3: Left*:* Scheme of the interface generation procedure. Right: Final distribution of cross-linked nitrogen atoms at 93% of total conversion along the *z* axis perpendicular to the interfaces, averaged in 2Å-wide intervals (red dots) superimposed to the density profiles of PVDF and Epoxy normalized to their bulk densities at 500 K (1.55 g/cm^3 and 1.05 g/cm^3, respectively)

equilibration procedure at high temperatures and pressures. The thermal and tensile properties of the bulk systems were examined and found to be in good agreement with experimental data. For interphase formation, slabs of both bulk systems were placed in a large simulation box and allowed to diffuse during equilibration at elevated temperatures and pressures. After equilibration we observed diffusion zones of 35-40 Å width. After diffusion the epoxy component was cross-linked using a dynamic, cut-off based cross-linking protocol (Fig. 3). Further, we observed the formation of mutually entangled loops of thermoplastic chains and resin strands across the interface during cross-linking. We propose that this network is a key factor to the mechanical stability of the interphase.

Outlook

It remains an open question how the putative formation of covalent bonds between PVDF and the epoxy would further strengthen the interfacial adhesion properties. Such bonds would certainly prevent chain pull-out from the epoxy network. Therefore, the next steps consist in using density functional theory to predict possible chemical bond formation at the interface between the two components. Further, we are aiming at improving the Molecular Dynamics interphase formation procedure by initiating cross-linking from the start of the diffusion process. This introduces competition between diffusion and cross-linking and provides a more accurate model of the real system during co-curing.

hbc00012: All-atom molecular dynamic investigations of the adhesion mechanisms at the contact interface of TiO2 nanoparticles in films and aggregates

hbc00013: Fabrication of multishaped magnetic structures via a knowledge based biomimetic approach

These two projects concluded their run on HLRN resources in the first quarter of 2017. The scientific results obtained thanks to the allocated computational resources have been already included in the 2016 BremHLR Annual Status Report. Publications resulting from the performed simulations have been included in the following list.

Publications

1. J. Laube, S. Salameh, M. Kappl, L. Mädler, L. Colombi Ciacchi, “Contact forces between TiO2 nanoparticles governed by an interplay of adsorbed water layers and roughness” *Langmuir* 31, 11288-11295 (2015).

2. J. Laube, M. Dörmann, H.-J. Schmid, L. Mädler, L. Colombi Ciacchi, “Dependencies of the adhesion forces between TiO2 nanoparticles on size and ambient humidity” *Journal of Physical Chemisty C* 121, 15294-15303 (2017).

3. J. Laube, V. Baric, S. Salameh, L. Mädler, L. Colombi Ciacchi, “A new contact model for the discrete element method simulation of TiO2 nanoparticles films under mechanical load” *Granular Matter* 20, 28 (2018).

4. S. Lid, S. Köppen, L. Colombi Ciacchi, “Creation of models and parametrization of a classical force field for amorphous Al2O3/water interfaces based on density functional theory” *Computational Materials Science* 140, 307-314 (2017).

5. J. Larrucea, S. Lid, L. Colombi Ciacchi; “Parametrization of a classical force field for iron oxyhydroxide/water interfaces”; *Computational Materials Science* 92, 343-352 (2014).

6. S. Lid, D. Carmona, M. Maas, L. Treccani, L. Colombi Ciacchi, “Anchoring of iron oxyhydroxide clusters at H and L ferritin subunits” *ACS Biomaterials Science & Engineering* 4, 483-490 (2018).

7. S. Lid, T. Kollmann, D. Zahn, L. Colombi Ciacchi, “Molecular mechanisms of crystal nucleation and growth at ferritin/oxide interfaces: a theoretical investigation”, Submitted

8. M. Laurien, B. Demir, H. Büttemeyer, A. Herrmann, T. Walsh, L. Colombi Ciacchi, “Atomistic modelling of the formation of a thermoset/thermoplastic interphase during co-curing”. Submitted

9. M. Delle Piane, S. Potthoff, J. C. Brinker, L. Colombi Ciacchi, “Molecular dynamics simulations of the silica – cell membrane interaction: insights on biomineralization and nanotoxicity”. To be submitted.

Funding:

The project **hbc00012** was worked out within the framework of the DFG priority program SPP 1486 "Partikel im Kontakt (PIKO) - Mikromechanik, Mikroprozessdynamik und Partikelkollektive". The project **hbc00013**was embedded within the framework of the DFG priority programme SPP 1569, entitled: “Generation of multifunctional inorganic materialsby molecular bionics”. The project **hbc00020** was funded by the DFG with the project ID: CO1043/11-1 and is entitled “Molekuladynamische Simulationen der Wechselwirkung zwischen Siliziumoxid und Phospholipid-Membranen im Kontext der Biomineralisation und der Nanotoxizität”. The HLRN provides computational resources for several projects in the hybrid materials interfaces group in the **magnitude of 2000 kCPU - hours/year**.

5.2 *hbc00017:* Modeling charge-carrier assisted reactions on the surface and in the bulk of transition metal oxides

HLRNProject ID:	hbc00017
Run time:	IV/2015 – IV/2017
Project Leader:	Prof. Dr. Peter Deák
Project Scientists:	Dr. BálintAradi
Affiliation:	University Bremen, Bremen Center for Computational Materials Science

Overview: Our project is a continuation of earlier work (hbc00001, hbc00011) on highly accurate theoretical simulation of defects in/on solids at the atomic level. The present project concentrates primarily on wide-band-gap (WBG) transition metal oxides. These materials have a wide range of practical applications but cannot be well described by the standard local and semi-local approximations of density functional theory (DFT), which have been the work horse of theoretical solid state physics for electronic structure calculations in the past decades. Therefore, our work encompasses – beside simulations for practical purposes – also method development and testing:

- Developing electron self-interaction corrections for the proper description of defects in wide band gap materials.
- Calculation of defect properties in ß-Ga_2O_3.
- Defect studies in CuGa(In)S(Se)$_2$ solar cell materials.
- Development and programming of a correction scheme for periodic low-dimensional charged systems.
- Simulation of photocatalytic oxidation/reduction on the anatase-TiO_2 surface.

Results

One of the methodical problems we are considering is the inclusion of self-energy correction into DFT for calculations on supercells with hundreds of atoms. We have shown that the error compensation between semi-local (GGA) and non-local (Hartree-Fock) exchange makes the screened hybrid functional HSE06 (of Heyd, Scuseria and Ernzerhof) almost self-interaction free in TiO_2 (see [1] and references therein). Unfortunately this is not the case in many other WBG materials. In the first year of the project we have shown that following proper theoretical guidelines in selecting the parameters of an HSE hybrid, the electronic structure can be very accurately reproduced in materials where the screening is weakly orbital- and direction-dependent. We have demonstrated this on ß-Ga_2O_3, providing also for the first time a consistent interpretation of the experimental spectra of defects in this important material [2], which is being considered (among others) for power electronics, as a transparent electrode, but also as photo-electrode for water splitting, as well as a white phosphor in lighting devices. Considering the latter, in the second year, we have concentrated on the light emitting properties of ß-Ga_2O_3. Our paper regarding the dependence of the colour on sample treatments has just been submitted [3].

We have also proven the efficiency of our method for other WBG materials. $CuGaS_2$ has the widest band gap among thin film solar cells, and doping with tin (on gallium sites, Sn_{Ga}) has been shown to give rise to a partially filled intermediate band in the gap, which could – in principle – improve the efficiency of solar light harvesting. Our optimized HSE hybrid functional was able to reproduce a characteristic light emission of $CuGaS_2:Sn_{Ga}$ (see, e.g., Fig.1a), proving that it can be applied to describe the interaction of defects. We have shown (Fig.1b), that increasing the Sn_{Ga} concentration automatically increases the concentration of a compensating intrinsic defect (Ga_{Cu}), which means that the intermediate band will be empty. This explains while the expected increase in the efficiency of this solar cell material has not been observed [4].

Since HSE calculations for surfaces are very costly even on a supercomputer, parallel with the work described above, we are developing “low-budget” corrections to standard semi-local (GGA) DFT calculations, which satisfy at least approximately the criteria used in parameterizing the hybrids. We have shown that, in case of surfaces, the corrections must depend on the coordination of the atoms, and succeeded in reproducing the small electron- and hole-polaron states in the bulk and on the surface of anatase and rutile TiO_2 [5]. (Note that this is a crucial requisite to simulate charge assisted reactions on the surface, like photocatalytic processes.)

Charge transport across phases plays an important role in photocatalysis, where the electron or the hole, generated by photo-excitation, promotes the chosen reaction, while the other carrier gets trapped, e.g., by scavenger molecules. In both processes, it is a crucial question whether the molecule is adsorbed or desorbed after charge transfer. Atomistic modelling via electronic structure calculations on periodic models has become a vitally important part of R&D also in these areas. Modelling of photo-catalytic reactions typically involves only one of the photo-excited carriers, since the other member of the electron-hole pair must be outside the explicitly treated (relatively small) system, to prevent recombination. Supercells with a net charge require corrections because of the interaction between artificially repeated charges. While various schemes have been proposed for correcting the total energy of charged defects in the bulk, gas/solid interfaces, where the charge can be located in either phase, remain a challenge. Solutions suggested so far are either restricted to special cases (making assumptions on the location of the charge) or do not correct the selective effect of the spurious electrostatic potentials on the individual one-electron states (i.e., are not self-consistent). In this project we develop a general and self-consistent charge correction scheme for supercell calculations in charged 1D, 2D and 3D systems. Our test system is the anatase-TiO_2 (101) surface, where we investigate reactions relevant to the photocatalytic oxidation/reduction of CO_x and NO_x species. In the first year of the project, we have discovered that, upon electron scavenging by O_2 molecules (a crucial reaction in the photo-assisted oxidation of CO), the negatively charged O_2^- desorbs from the surface. In the second year, we have investigated, how this process contributes to the full photocatalytic (i.e. cyclic) oxidation of CO. We have found that the positively charged oxygen vacancies, created during spontaneous oxidation of CO on the positively charged surface can be healed by the O_2^-molecules, and the pristine surface can be regained [6].

Outlook

We will continue working on the development of an appropriate charge correction code, and apply it to charge assisted surface reactions on TiO_2, notably oxidation of NO in the presence of H_2O molecules, which may act as hole-scavengers. However, our work on the hybrid functionals have shown that further method development will be necessary also in that direction. The optimized HSE parameters are materials-specific with limited transferability even between related compounds. Since the standard HSE notoriously fails for Ga-based semiconductors, making re-optimization of the parameters in every case, our plan is to investigate the field of optimal parameters for a series of such compounds, trying to elucidate a possible generalization. This is a big task, so we have applied for a new project (hbc00027).

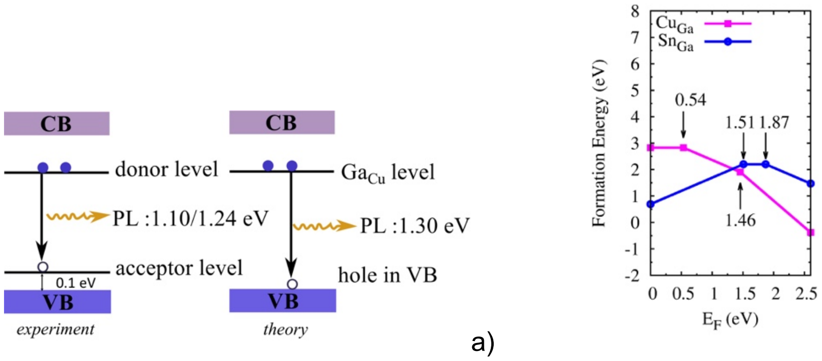

a) b)

Fig.1: Observed and calculated photoluminescence (a), and formation energy of the Sn_{Ga} and Cu_{Ga} defects in $CuGaS_2$ (b).

Publications

1. P. Deák, *Calculating the optical properties of defects and surfaces in wide band gap materials*. Physica B, https://doi.org/10.1016/j.physb.2017.06.024, (2018).
2. P. Deák, Quoc Duy Ho, F. Seemann, B. aradi, M. Lorke, and T. Frauenheim, *Choosing the correct hybrid for defect calculations: a case study on intrinsic carrier trapping in ß-Ga_2O_3*. Phys. Rev. B *95,075208 (2017).*
3. Quoc Duy Ho, T. Faruenheim, and P. Deák, *The origin of photoluminescence in ß-Ga_2O_3, submitted*
4. M. Han, Z. Zeng, T. Frauenheim, and P. Deák, *Defect physics in intermediate-band materials: Insight from an optimized hybrid functional,* Phys. Rev. B *96, 165204 (2017).*
5. M. F. Tabriz, B. Aradi, T. Frauenheim, and P. Deák, *Application of the Lany-Zungerpolaron correction for calculating surface charge trapping.*J. Phys.: Condens. Matter. *29, 394001 (2017).*
6. K. Rehling, *Analysis of the Reaction Paths of Oxygen on the Anatase* (101) Surface using Polaron and Gap corrected DFT, Master Thesis, University Bremen 2018.

5.3 ***hbi00024:*** 3D Simulation einer kompressiblen Edelgasströmung innerhalb eines thermischen Lichtbogentriebwerks

HLRN-Projektkennung:	hbi00024
Laufzeit:	II/2014 – III/2017
Projektleiter:	PD Dr.-Ing Rodion Groll
Projektbearbeiter.	J. Gomez
Institut / Einrichtung:	ZARM – Center of Applied Space Technology and Microgravity, Universität Bremen

Überblick

Im vorliegenden Forschungsprojekt wird das Verhalten eines Lichtbogentriebwerks, welches mit den Edelgasen Neon, Argon, Krypton und Xenon betrieben wird, sowohl experimentell als auch numerisch untersucht. Der experimentelle Versuchsaufbau wird in Abb. 1 schematisch dargestellt. In vorherigen Projektphasen wurde der Fokus auf das Verhalten der kompressiblen Strömung im Kaltgas-Betrieb gelegt. Das Kaltgas-Triebwerk wird unter Vakuumbedingungen betrieben. Bei den Kaltgas-Untersuchungen wurde der Druckverlust für die jeweiligen Gase bei verschiedenen Massenstromwerten zwischen 0,178 mg/s und 3,568 mg/s gemessen. Die Knudsen-Zahlen der untersuchten Betriebspunkte liegen oberhalb der Kontinuumsgrenze 0,01, was zum Auftreten von Verdünnungseffekten führt. Die experimentell ermittelten Druckwerte wurden mit numerischen Simulationsergebnissen verglichen. Als numerischer Ansatz wurde sowohl die kompressible Form der Navier-Stokes-Gleichungen mit gewöhnlichen Haftbedingungen, als auch die kinetische Direct-Simulation-Monte-Carlo (DSMC) Methode berücksichtigt.

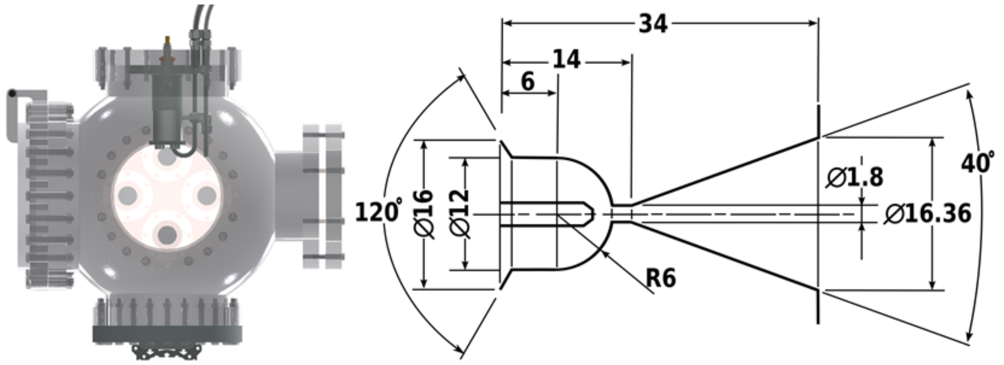

Abb. 1: Schematische Darstellung des Versuchsaufbaus (links) und der eingesetzten Lavaldüse (rechts) mit geometrischen Maßen in mm.

Aus dem Vergleich zwischen den experimentellen Ergebnissen und den Navier-Stokes-Simulationen wurde eine von der Knudsen-Zahl abhängige Korrekturfunktion entwickelt, welche auf vier gasunabhängigen Koeffizienten basiert. Die Knudsenfunktion ermöglicht es, aus Navier-Stokes-Simulationen mit gewöhnlichen Haftbedingungen den korrekten Druckverlust in Abhängigkeit von der Knudsen-Zahl zu bestimmen. Hierbei liegt der Hauptvorteil des Ansatzes an den deutlich niedrigeren Rechenanforderungen im Vergleich zu DSMC-Simulationen.

In der letzten Projektphase wurde der Fokus auf das Verhalten der kompressiblen Strömung im Heißgas-Betrieb gelegt. Hierbei wird das Plasma, welches durch die elektrische Entladung zwischen der Kathode und der Anode des Lichtbogentriebwerks entsteht, mittels eines hauseigenen, kinetischen Ansatzes modelliert. Vorläufige Ergebnisse bestätigen die Anwendbarkeit des entwickelten Modells.

Ergebnisse

In vorherigen Projektphasen konnte eine mathematische Korrekturfunktion entwickelt werden, welche es ermöglicht, die Druckergebnisse der Navier-Stokes-Simulationen mit Haftbedingungen für den Kaltgas-Betrieb des Lichtbogentriebwerks zu korrigieren. Die experimentellen und numerischen Ergebnisse werden in Abb. 2 dargestellt. Aus Abb. 2 ist die sehr gute Übereinstimmung zwischen den korrigierten, numerischen Ergebnissen und den experimentell ermittelten Druckwerten ersichtlich.

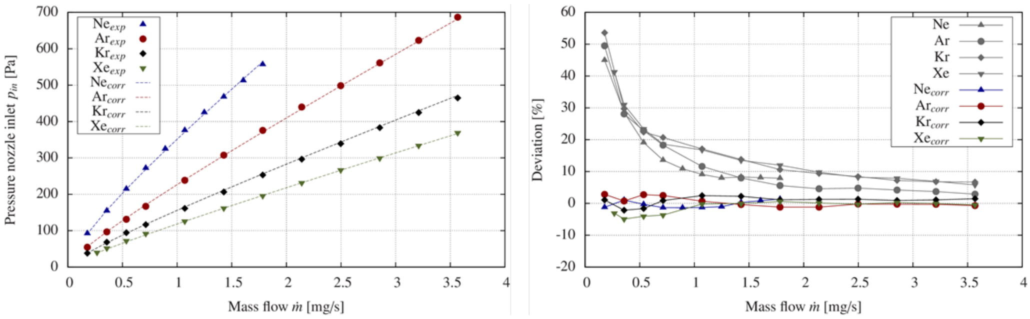

Abb.2: Experimentelle und korrigierte Navier-Stokes-Ergebnisse für den Inletdruck in Abhängigkeit vom Massenstrom. Links: Absolute Druckwerte; rechts: Relative Abweichungen.

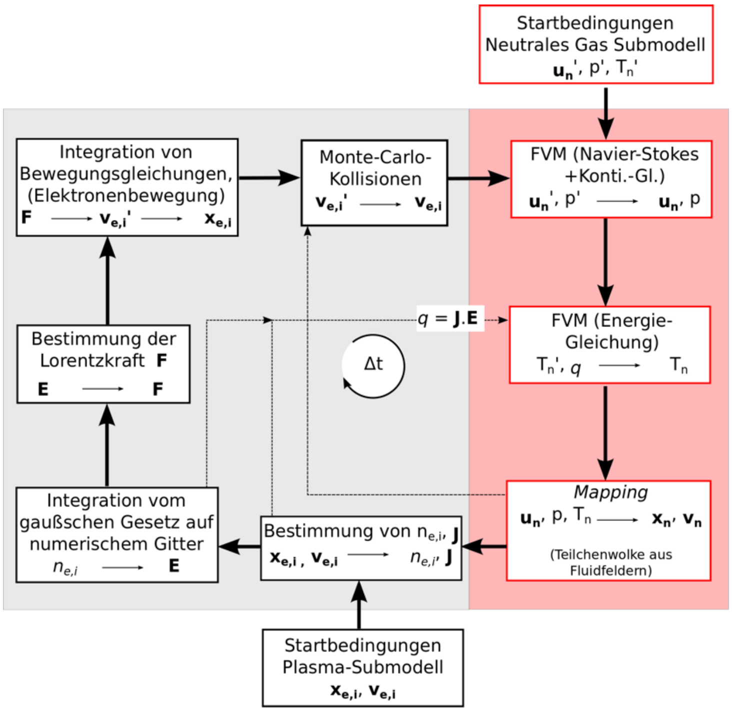

Abb. 3: Konzept eines Plasmamodells. Grau: Kinetisches Submodell für Elektronen und Ionen. Rot: Fluid-Submodell für neutrales Gas. u: Geschwindigkeitsfeld; p: Druck; T: Temperatur; q: Quellterm (Joule'sche Erwärmung); x: Position (Testpartikel/kinetisch); v: Geschwindigkeit (Testpartikel/kinetisch); Indizes: n: neutrales Gas; e: Elektronen; i: Ionen.

In der letzten Projektphase wurde ein neuartiges Konzept zur Modellierung vom Plasma innerhalb des Lichtbogentriebwerks beim Heißgas-Betrieb entwickelt und validiert. Aufgrund der sehr hohen Rechenanforderungen wurde auf einen vollständig kinetischen Ansatz verzichtet und ein hybrides Modell angestrebt. Das Modell besteht aus einer kinetischen Behandlung der Elektronen und Ionen und einer fluiddynamischen Betrachtung des neutralen Gases im Plasma. Das Modell ist in Abb. 3 schematisch dargestellt. Im Rahmen der letzten Projektphase konnten wichtige Komponenten des kinetischen Ionen-Elektronen-Submodells (Grau in Abb. 3) mittels analytischen Methoden validiert werden.

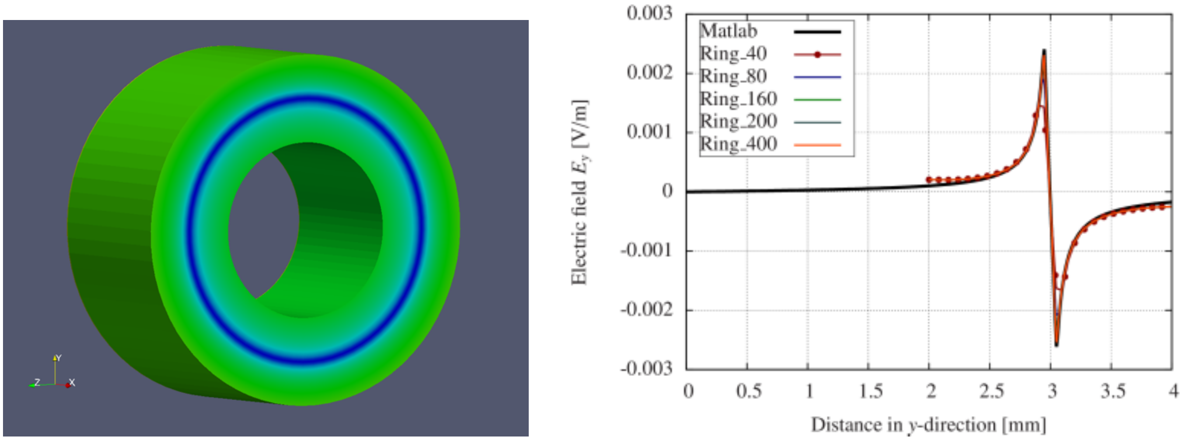

Abb. 4: Vergleich zwischen den numerischen und den analytischen (Matlab) Ergebnissen für die elektrische Feldstärke in Abhängigkeit von der Gitterauflösung. Die Ringgeometrie ist links dargestellt.

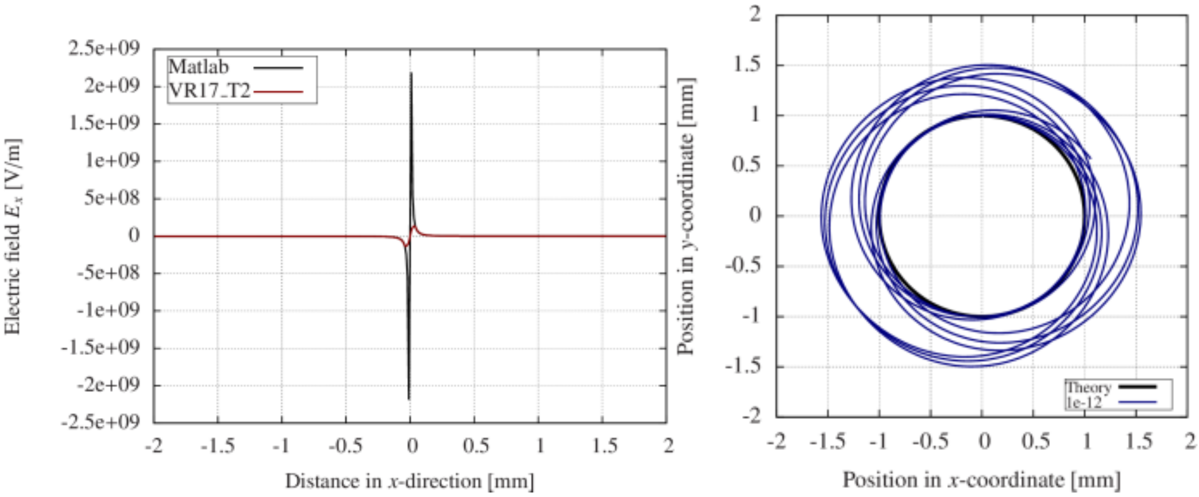

Abb. 5: Vergleich zwischen den numerischen und den analytischen Ergebnissen für den Lorentz-Solver. Dasvom Ion erzeugte elektrische Feld wird links dargestellt.

Zu den validierten Komponenten zählt der Maxwell-Solver für die Ermittlung der elektrischen Feldstärke und des elektrostatischen Potentials. Vergleiche zwischen den numerischen und den analytischen Ergebnissen sind in Abb. 4 für eine dreidimensionale Ringgeometrie dargestellt. Die sehr gute Übereinstimmung bestätigt die Gültigkeit des Maxwell-Solvers. Eine weitere wichtige Solver-Komponente ist der Lorentz-Löser, der für die Bahnberechnung der Ladungsträger in einem elektrischen Feld eingesetzt wird. Um diesen zu validieren, wurde eine Reihe von Simulationen durchgeführt, bei denen ein Elektron ein in der Mitte des Rechengitters platziertes Ion umkreist. Aus den in Abb. 5 dargestellten Ergebnissen ist die gute Übereinstimmung zwischen der numerischen und der theoretischen Elektronenbahn zu erkennen, wobei eine Verbesserung durch den Einsatz der Leapfrog-Methode zurzeit angestrebt wird.

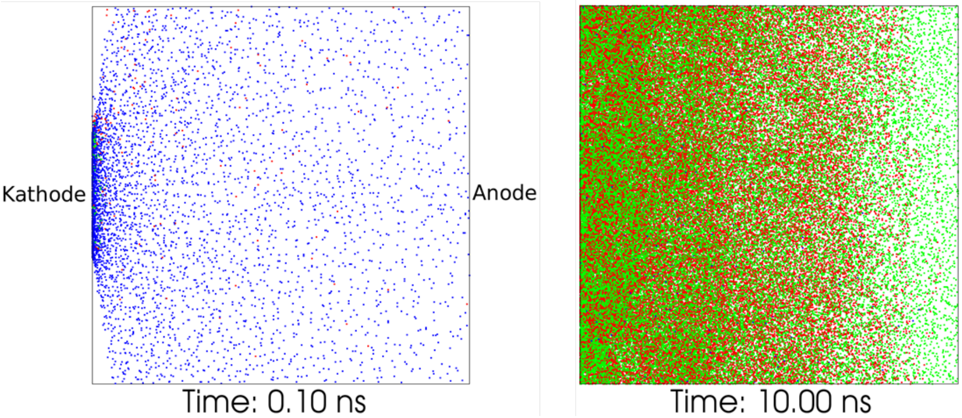

Abb. 6: Vorläufige Ergebnisse für die elektrische Entladung zwischen der Kathode und der Anode eines Lichtbogentriebwerks zu dem Zeitpunkt t = 0,10 ns (links) und t = 10 ns (rechts).

Vorläufige Ergebnisse für die elektrische Entladung innerhalb des Lichtbogentriebwerks werden in Abb. 6 dargestellt. Bei dieser Simulation wird Argon als neutrales Gas modelliert und eine elektrische Stromstärke von 30 A zwischen Kathode und Anode vorgegeben. Zu dem Zeitpunkt t = 0,1ns ist ein deutlicher Überschuss an Primärelektronen (blaue Punkte) zu erkennen. Darüber hinaus befinden sich nur wenige Ionen (grün) und Sekundärelektronen (rot) im Berechnungsraum. Die Elektronen werden auf Grund des entstehenden, elektrischen Feldes in Richtung der Anode beschleunigt. Dabei kollidieren sie mit neutralen Argon-Atomen in der Brennkammer des Lichtbogentriebwerks. In Abhängigkeit von der Kollisionsenergie können diese Kollisionen zur Ionisierung des neutralen Atoms und zur Bildung eines Elektron-Ion-Paares führen. Die entstehenden Sekundärelektronen werden ebenfalls in Richtung der Anode beschleunigt und können selbst weitere Ionisierungskollisionen einleiten. Die resultierende Elektronenlawine hat die Bildung eines elektrischen Lichtbogens zwischen der Kathode und der Anode des Lichtbogentriebwerks zur Folge.

Ausblick

Mit Hinblick auf die Simulation des Lichtbogentriebwerks ist die Untersuchung der Kopplung zwischen dem Ionen-Elektronen-Submodell und dem Fluid-Submodell von zentraler Bedeutung. Auf diese Weise könnte im Rahmen zukünftiger Projekte ein Gesamtmodell für das elektrische Lichtbogentriebwerk validiert werden.

Publikationen

1. J. Gomez, R. Groll, *Pressure drop and thrust predictions for transonic micronozzle flows*, Physics of Fluids (1994-present), 28, 022008 (2016)
2. J. Gomez, R. Groll, *Experimental and numerical study of the pressure drop in transonic micronozzle flows across multiple flow regimes,* ASME 2016 14th International Conference on Nanochannels, Microchannels, and Minichannels, Washington DC, July 10-14 2016, American Society of Mechanical Engineers

5.4 ***hbi00026:*** DSMC-Simulation einer verdünnten Edelgasströmung innerhalb eines Kaltgas-Arcjets

HLRN-Projektkennung:	Hbi00026
Laufzeit:	II/2017 – I/2018
Projektleiter:	Dr.-Ing. habil. Rodion Groll
Projektbearbeiter.	Till Frieler, M.Sc.
Institut / Einrichtung:	ZARM – Zentrum für angewandte Raumfahrttechnologie und Mikrogravitation

Überblick und Projektbeschreibung MOLETHRUSTBALANCE

Elektrische Raumfahrtantriebe sind heutzutage bereits in einer Vielzahl von Weltraummissionen erfolgreich im Einsatz und werden beispielsweise zur Bahn- und Lageregelung auf geostationären Kommunikationssatelliten oder für interplanetare Langzeitmission genutzt. Für die Entwicklung neuer Triebwerke sind unter anderem Leistungsmerkmale, wie Antriebsleistung (spezifischer Impuls), Treibstoffverbrauch (Treibstoffeffizienz) und Regelverhalten (Schubcharakteristik) von großer Bedeutung.

Um eine Aussage über die Treibstoffeffizienz und die Schubcharakteristik eines Triebwerks machen zu können, ist es sinnvoll die Schubkraft F_s bestimmen zu können. Im Rahmen des Forschungsprojektes MOLETHRUSTBALANCE wird einerseits ein Versuchsstand zur experimentellen Messung und Untersuchung der Schubkraft von elektrischen Triebwerken niedriger Leistungsklasse entwickelt und aufgebaut, sowie andererseits numerische Kaltgas-Simulationen mittels DSMC-Methoden durchgeführt. Der Vergleich der numerischen und experimentellen Ergebnisse wird im Anschluss genutzt, um Erkenntnisse für die weitere Optimierung des Triebwerks sammeln zu können.

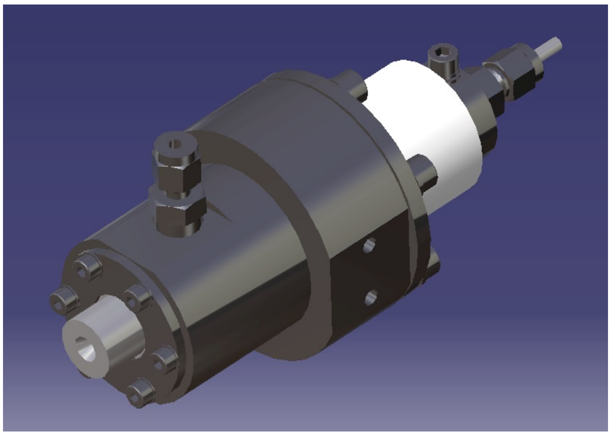

Abb. 1: Gerenderte, isometrische Ansicht des INGA IV Lichtbogentriebwerks.

Das in dem Projekt MOLETHRUSTBALANCE untersuchte Triebwerk ist das am ZARM entwickelte Lichtbogentriebwerk INGA IV. Das Triebwerk ist in Abbildung 1 dargestellt. Mit dem INGA IV Triebwerk können Differenzdrücke zwischen dem Inneren des Triebwerks und der Vakuumkammer aufgezeichnet und Untersucht werden. Aus den gemessenen Drücken und dem Massenstrom des eingeleiteten Gases können, unter Verwendung der numerischen Methoden, Rückschlüsse auf die Antriebsleistung gezogen werden.

Technische und mathematische Aspekte

Für die, in dem Projekt MOLETHRUSTBALANCE durchgeführten, numerischen Berechnungen wurden an der Standardimplementierung des DSMC-Solvers in dem Softwarepaket OpenFOAM einige Änderungen vorgenommen. Die Änderungen beinhalteten die Implementierung eines neuen Inflowmodells ZARMInOutflow, welches auf dem InOutflow-

Modell der Standardimplementierung aufbaut. Es ermöglicht dem Nutzer die, aus den Experimenten genau definierten, Massen- oder Volumenströme über die Volumenränder des Inlets vorzugeben. Für die Randflächen des Outletvolumens ist der Druck die vorgegebene makroskopische Größe aus den Experimenten. Dieser wird als Absolutdruck durch die Drucksensoren der Vakuumanlage gemessen und stellt den, sich im stationären Betriebszustand eingestellten, Umgebungsdruck in einiger Entfernung zum Diffusorende (Düsenauslass) dar.

Anders als bei Finite-Volumen-Solvern hängt bei statistischen Methoden, wie der DSMC-Methode, der Rechenaufwand stark von der Gesamtanzahl der simulierten Testpartikel im Simulationsvolumen ab. Der Rechenaufwand für die einzelnen Testpartikel lässt sich hierbei nochmals in die Anteile Molekülbewegung und Kollisionsberechnung unterteilen. Abhängig von der Art der Implementierung der Kollisionsroutine in den numerischen Solver nimmt nach Titov [1] die Berechnung der Kollisionen bis zu 60% der Rechenzeit in Anspruch.

Um den numerischen Aufwand der Kollisionsberechnung bei hohen Drücken zu reduzieren, wurden zwei Methoden zur Begrenzung der Kollisionen nach Titiov [1] und nach Zhang [2] implementiert. Hierbei wird in der ersten Methode die Anzahl Kollisionen über einen statischen Wert begrenzt, so dass es für die Anzahl der Kollisionen pro Molekül und Rechenzeitschritt eine feste, einstellbare Obergrenze existiert.

Bei der dynamischen Limitierungsmethode werden hingegen die Kollisionen pro Zeitschritt und Partikel durch eine Funktion berechnet. Die Funktion greift in den Prozess der Kollisionsberechnung ein, in dem bei Sie in Abhängigkeit der Strömungsbedingungen Werte kleiner eins liefert und maximal gegen einen Wert von eins strebt. Multipliziert mit der zuvor berechneten Anzahl der Kollisionen, ergibt sich eine von den Strömungsbedingungen abhängige Reduzierung der durchzuführenden Kollisionen.

Einfluss der Wandreibung auf die Strömung

Um vorhandene Abweichungen der numerischen zu den experimentellen Ergebnissen für den Brennkammerdruck zu quantifizieren und gegeben falls zu reduzieren wurde der Einfluss der Wandreibung in der DSMC Simulation untersucht. In dem, in der DSMC Simulation verwendeten Wandkollisionsmodell lässt sich der Einfluss der Wandreibung über den "Wall accommodation coefficient" σ_v steuern. Ein Wert von $\sigma_v = 1{,}0$ repräsentiert hierbei eine vollkommen diffuse Reflektion der simulierten Teilchen an der Wand, während ein Wert von $\sigma_v = 0{,}0$ eine spiegelnde Reflektion modelliert. Ein Wert von $\sigma_v = 0{,}0$ würde eine reibungsfreie Strömung modellieren, was für das untersuchte Triebwerk zu nicht physikalischen Ergebnissen führen würde. Jedoch könnte eine leichte Variation von σ_v die Durchströmung der Düse verbessern und als Folge zu einer Reduzierung der Abweichungen des vorhergesagten Brennkammerdrucks in der DSMC Simulation mit statischer Limitierung führen.

Untersucht wurden Werte von 1,0, 0,9, 0,8 und 0,5 für σ_v. In Tabelle 1 sind die Ergebnisse für den Brennkammerdruck p_s für DSMC Simulationen mit statischer Limitierung für die vier Massenströme 0,357 mg/s, 3,568 mg/s, 35,68 mg/s und 71,360 mg/s dargestellt und in Relation zu den experimentellen Werten gesetzt. Die Ergebnisse in der Tabelle zeigen, dass es für alle untersuchten Massenströme zu einem Abfall des vorhergesagten Brennkammerdruck kommt, wenn für σ_v ein kleinerer Wert verwendet wird. Hierbei wird die größte Reduzierung und die kleinsten Abweichungen für $\sigma_v = 0{,}5$ erreicht. Vergleicht man die numerischen mit den experimentellen Werten für p_s, so könnten zwei Effekte beobachtet werden. Für die kleineren Massenströme bis zu 3,568 mg/s würde ein Wert zwischen 0,9 und 0,8 zu einer Verbesserung der numerischen Ergebnisse führen und die Abweichung zu den experimentellen Werten negieren. Für einen Wert von 0,5 für σ_v würden hingegen zu niedrige Brennkammerdrücke vorhergesagt werden. Für die größeren dargestellten Massenströme von

35,680 mg/s und 71,360 mg/s können hingegen nur leichte Verbesserungen in den numerischen Ergebnissen für p_s erzielt werden. Selbst für einen Wert von σ_v = 0,5 werden zu hohe Brennkammerdrücke vorhergesagt.

Massenstrom [mg/s]	Exp. p_s [Pa]	Num. p_s [Pa]				(SCL DSMC)
		$\sigma_v = 1{,}0$	$\sigma_v = 0{,}9$	$\sigma_v = 0{,}8$	$\sigma_v = 0{,}5$	
0,357	595	606	599	589	556	
	+0,0%	+1,6%	+0,7%	-1,0%	-6,5%	(Abw.)
3,568	5190	5203	5199	5171	5062	
	+0,0%	+0,3%	+0,2%	-0,4%	-2,5%	(Abw.)
35,680	47811	51909	51661	51449	50563	
	+0,0%	+8,6%	+8,0%	+7,6%	+5,8%	(Abw.)
71,360	93533	104186	103814	103432	101515	
	+0,0%	+11,4%	+11,0%	+10,6%	+8,5%	(Abw.)

Tab. 1: Brennkammerdrücke $p_s$von DSMC Simulationen mit statischer Limitierung der Kollision (SCL) für verschiedene Werte σ_v und Massenströme.

Vergleich zwischen modifiziertem DSMC Solver und reiner DSMC Simulation

Um den Einfluss der statischen Limiterungsmethode weiter quantifizieren zu können, wurden die erhaltenen Ergebnisse für den Brennkammerdruck in einer weiteren Studie mit reinen DSMC Simulationen ohne Limitierung, Navier-Stokes Simulationen und den experimentellen Ergebnissen verglichen. Hierbei wurden die Massenströme 0,357 mg/s, 1,780 mg/s, 3,568 mg/s und 7,136 mg/s untersucht. In Tabelle 2 sind die erhaltenen Brennkammerdrücke p_s aus den Experimenten und den numerischen Simulationen mit den drei Solvern für die vier Massenströme dargestellt.

Massenstrom [mg/s]	Exp. p_s [Pa]	Num. p_s [Pa]			
		SCL DSMC	DSMC	NS	
0,357	595	606	606	674	
	+0,0%	+1,9%	+1,9%	+13,3%	(Abw.)
1,780	2721	2673	2660	2683	
	+0,0%	-1,8%	-2,2%	-1,4%	(Abw.)
3,568	5190	5203	5178	5093	
	+0,0%	+0,3%	-0,2%	-1,9%	(Abw.)
7,136	9747	10366	9840	9816	
	+0,0%	+6,4%	+1,0%	+0,7%	(Abw.)

Tab. 2: Vergleich zwischen experimentellen und numerischen Ergebnissen der drei Solver (SCL DSMC, reines DSMC, Navier-Stokes) für p_s für Massenströme zwischen 0,357 mg/s und 7,136 mg/s.

Aus der Tabelle lässt sich gut erkennen, dass für den kleinsten untersuchten Massenstrom von 0,356 mg/s kein messbarer Einfluss auf den Brennkammerdruck vorhanden ist, wenn die statische Limitierungsmethode angewendet wird. In Kontrast dazu sagt die Navier-Stokes Simulation deutlich zu hohe Brennkammerdrücke vorher. Für die beiden mittleren Massenströme von 1,780 mg/s und 3,568 mg/s könnten ebenfalls nur kleine Änderungen im vorhergesagten Brennkammerdruck festgestellt werden, wenn man die DSMC Simulationen mit und ohne statische Limitierung miteinander vergleicht. Für die Navier-Stokes Simulationen lässt sich ebenfalls nur eine kleine Abweichung zu den experimentellen Werten feststellen. Für den größten untersuchen Massenstrom von 7,136 mg/s lässt sich erkennen, dass der DSMC Solver mit statischer Limitierung den Brennkammerdruck im Vergleich zu den experimentellen Werten um 6,4% zu hoch vorhersagt. Im Kontrast hierzu sagt der reine DSMC Solver den Brennkammerdruck gut vorher, mit nur einer kleinen Abweichung von etwa 1% zu den experimentellen Ergebnissen. Die Druckabweichungen in den numerischen Ergebnissen von der reinen DSMC Simulation und der Navier-Stokes Simulation sind hierbei innerhalb des numerischen Fehlers der beiden Simulationen.

Zusammenfassung und Ausblick

In dem Forschungsprojekt MOLETHRUSTBALANCE sollen aus numerischen Bestimmung des Schubs, sowie experimentellen Schubmessungen Erkenntnisse für die Optimierung des INGA IV Triebwerks gesammelt werden. Hierfür sollen sowohl im experimentellen Aufbau, sowie bei den numerischen Berechnungen eine Reihe von Parametern innerhalb einer Parameterstudie variiert und deren Einfluss ausgewertet werden.

Im letzten Antragszeitraum wurde der Einfluss des Parameters Wandreibung auf die Strömung untersucht, mit dem Zeil diesen genauer quantifizieren zu können und die Genauigkeit der numerischen Ergebnisse zu erhöhen. Weiterhin wurden Ergebnisse aus DSMC Simulationen mit statischer Limitierung mit numerischen Ergebnissen aus reinen DSMC Simulationen ohne Limitierung, Navier-Stokes Simulationen und den experimentellen Ergebnissen verglichen. Neben der bereits implementierten statischen Limitierungsmethode wurde im letzten Antragszeitraum eine Methode zur dynamische Limitierung der Kollisionen in den Solver implementiert. Diese soll nun in einigen zukünftigen Parameterstudien mit der Methode zur statischen Limitierung vergleichen werden und Unterschiede in den numerischen Ergebnissen zwischen den beiden Methoden quantifiziert werden.

Publikationen

1. T.Frieler, R. Groll: *Using DSMC selection limiter for micronozzle thrust predictions with high density ratios*. (in Begutachtung)
2. T.Frieler, R. Groll: *A torsional sub milli-Newton thrust balance based on a spring leaf strain gauge sensor.* (in Begutachtung)
3. T.Frieler, R. Groll: *Validation of a mass flow driven inflow model for the DSMC method*. (in Vorbereitung)

Weitere Informationen / Literatur

[1] Titov, Evgeny V., and Deborah A. Levin. *Extension of the DSMC method to high pressure flows*, International Journal of Computational Fluid Dynamics 21.9-10 (2007): 351-368.

[2] Zhang, Ronghai ; Yao, Wei ; Li, Jindong: *A selection limiter of DSMC for near continuum flows*. Communications in Nonlinear Science and Numerical Simulation 13 (2008), Nr. 10, S. 2203-2212.

5.5 *hbi00027:* 3D Simulation of a magnetoplasmadynamic thruster with coaxial induced magnetic field

HLRN Project ID:	hbi00027
Run time:	IV/2015 – II/2018
Project Leader:	PD Dr.-Ing. habil. Rodion Groll
Project Scientists:	Charles Chelem Mayigué, M. Sc.
Affiliation:	ZARM – Center of Applied Space Technology and Microgravity

Overview

The magnetoplasmadynamic (MPD) arcjet is a promising thruster which is developed for exploration missions to the moon and Mars [1,2], and for raising orbits of large space structures. The MPD arcjet utilizes mainly electromagnetic force, i.e, Lorentz force, which is generated in this work by interaction between the current density and a coaxial magnetic field azimuthally induced by the total discharge current. In the present work, we developed and used a density-based method associated with a divergence cleaning technique for the simulation of the MPD thrusters under a finite volume formulation. This new algorithm was developed for the single resistive MHD equations and make use of the central-upwind scheme of Kurganov and Tadmor for flux calculation [3]. Electrical conductivity for fully ionized plasma and viscosity are predicted according to the Spitzer-Härm formulation and the Sutherland thermophysical model respectively. The perfect gas equation of state is also considered.

Results

A limited set of computer runs were performed to access the effect of geometric scale changes on self-field MPD thruster performance. The first geometry set (MPDT01) consisted of a 0.0095 m radius cathode with 0.264 m length, surrounded by a 0.025 m radius anode. The second set (MPDT02) doubled the anode radius to 0.051 m, but kept the cathode radius at 0.0095 m. The third set (MPDT03) kept the anode radius at 0.051 m, but increased the cathode radius to 0.0181 m. The last set (MPDT04) has the same parameter than MPDT02, but reduce the cathode length to 13.2 cm. For each combination of radii, the anode lengths are scaled from 1 to 5 times the anodes radius (aspect ratio). The argon propellant mass flow rate was kept constant at 6 g/s, and was assumed to be fully ionized for all cases. A nondimensionalize current parameter ξ [5] is used to analyse the thruster performance instead of the power parameter I^2/m. Results of the numerical simulations for MPDT02 with long cathode are presented below. MPDT02 thruster was not able to converge for aspect ratio $l_a/r_a=1$. Convergence was obtained for all the ξ values with $l_a/r_a > 1$. Thrust and plasma voltage increase with increasing ξ(Fig.1). The transition from electrothermal acceleration mode to electromagnetic acceleration mode occur at ξ around 0.6 which correspond to a discharge current value of 10 kA (critical current). These results are almost similar for the two other geometry configurations MPDT01 and MPDT02 with different stability range and different critical current value. But most generally, the simulation points out the fact that, at lower ξ, thruster operation require larger aspect ratio with shorter cathode length for more stability. For equivalent ξ value, small aspect ratio thrusters are required to improve the thruster flow efficiency.

Outlook

The results obtained in this project indicate that the semi-discrete density-based central-upwind solver is able to deal with plasma flow simulation in MPD thrusters and therefore will be helpful for their development and designing.

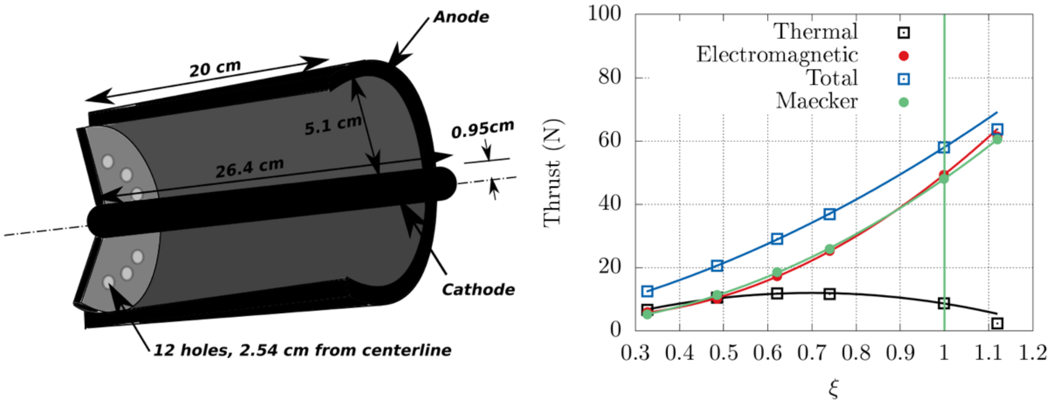

Fig. 1: Villani-H MPD thruster geometry (left) and MPDT02 thrust performance with l_a/r_a=5 and l_c=0.264 m (right).

Publications

1. C. Chelem Mayigue, R. Groll, *A density-based method with semi-discrete central-upwind schemes for ideal magnetohydrodynamics,* Arch. Appl. Mech. (2016) doi :10.1007/s00419-016-1216-7.
2. C. Chelem Mayigue, R. Groll, *Magneto-Plasmadynamic Thruster modelling with coaxial induced magnetic field,* Int. J. Comp. Meth. and Exp. Meas., Vol. 4, No.4 (2016) 380–392.
3. C. Chelem Mayigue, R. Groll, *Numerical simulation of Argon fuelled self-field magnetoplasmadynamic thrusters using the central-upwind scheme flux interpolations,* Submitted to European Journal of Mechanics B/Fluids.

Presentations

4. C. Chelem Mayigue, R. Groll, 11th International Conference on Advances in Fluid Mechanics in Ancona (Italy), 5-7/09/2016.
5. C. Chelem Mayigue, R. Groll, 4th Northern germany OpenFoam User meetiNg (NOFUN) 2016, Braunschweig, Germany, 29/09/2016.

References

1. R. G. Jahn, E. Y. Choueiri, *Electric propulsion*, Academic Press Encyclopedia of Physical Science & Technology (2000) 1–17.
2. K. Sankaran, *Simulation of mpd flows using a flux-limited numerical method for the mhd equations*, Ph.D. thesis, Princeton University, Technology and Medicine, Princeton (2005).
3. A. Kurganov, S. Noelle, G. Petrova, Semi-discrete central-upwind schemes for hyperbolic conservation laws and hamilton-jacobi equations, SIAM Journal on Scientific Computations 23 (2001) 707–740.

4. C. J. Greenshields, H. G. Weller, L. Gasparini, J. M. Reese, Implementation of semi-discrete, non-staggered central schemes in a collocated, polyhedral, finite volume framework, for high-speed viscous flows, International journal for numerical methods in fluids 63 (2010) 1–21.

5. Choueiri, E. Y, Scaling of Thrust in Self-Field Magnetoplasmadynamic Thrusters, Journal of Propulsion and Power (1998) 744–753.

5.6 *hbi00030:* Investigation of performance of an argon fueled magnetoplasmadynamic thruster with applied magnetic fields

HLRN Project ID:	hbi00030
Run time:	II/2016 – I/2018
Project Leader:	PD Dr.-Ing. habil. Rodion Groll
Project Scientists:	Charles Chelem Mayigué, M. Sc.
Affiliation:	ZARM – Center of Applied Space Technology and Microgravity

Overview

The applied-field magnetoplasmadynamic thrusters (AF-MPDT) are the promising technology for space missions requiring high specific impulse, high thrust density with low on board electric power. In this device, the plasma is accelerated by combining the gas dynamic and the electromagnetic processes. In the present project, the numerical modeling of AF-MPDT is performed using a electromagnetic code to produce external magnetic field and the density-based code, developed in the on going MagJet project, to deal with magnetohydrodynamic (MHD) equations. The magnetic field is axially applied by an external coil surrounding the anode which interacts with the discharge current and the induced azimuthal current to produced thrust. We make used of the Spitzer-Härm formulation for the calculation of electrical conductivity as the plasma in this work is considered fully ionized. The main goals of the Applied-MhdJet project are: Optimize the thruster and electrode geometry and particularly the configuration of the applied magnetic field of an AFMPDT.Investigate the influence of externally-applied magnetic fields strength and discharge current on the thruster efficiency. Better understanding of all propellant acceleration mechanisms. The achievement of acceptable thruster performance, especially in terms of thrust efficiency.

Results

A limited set of computer runs were performed to access the effect of external magnetic strength and mass flow rate of Argon on the NASALeRC MPD thruster performance (see Tab.1). For the purpose of comparison of our results with previous study, we decided to change the former geometry with the applied field NASA Lewis Research Center's (NASALeRC) MPD thruster geometry, which in contrary to the Villani-H thruster was typically investigated for applied-field code with a wide range of experimental data. For the same reason, we also decide to replace the geometric scaling analysis based on the ratio of anode over cathode radius by the variation of the mass flow rate of argon which ranging from 0.06 g/s to 0.2 g/s. Thus, the configuration considered (AFMPDT01) consisted of a cathode with 1.27 cm radius, surrounded by an anode with 5.1 cm radius both are 7.6 cm long. For the AFMPDT01 configuration, the magnet coil that provide the applied magnetic field is 15.3 cm long with a 10.15 cm radius. To avoid the creation in the discharge chamber of two magnetic force pointing in opposite direction, the magnet is placed with one end coinciding with the exit plane of the thruster. The second configuration we considered in this work named AFMPDT02, maintains the same geometric dimensions of AFMPDT01 but here, two magnet coils with a 10.15 cm radius have been used instead of one. the first magnet is 11.72 cm long and it is placed one end at 1.6 cm downstream of the inlet. The second one is 3.4 cm long with one end at the thruster exit. For each value of mass flow rate, the discharge current strength are scaled form 750 A to 2000 A. The five values of the applied magnetic field strength was varied from 0.012 T to 0.08 T, as measured at the cathode tip. The most challenging results of the numerical simulations with AFMPDT01 realised at this stage of the project are presented in Fig.1. The main effect of the application of an axial magnetic field is to put the plasma in rotation inside the discharge chamber of the MPD thruster. Here, for a constant value of applied magnetic field strength, the swirl to self thrust ratio decreases by increasing the current (see Fig. 2). In the other hand for each current value, this ratio increases by increasing the applied magnetic field. Thus, for the case of consideration, it appeared that the swirl component of thrust is dominant and is mostly responsible of the acceleration of the plasma out of the thruster.

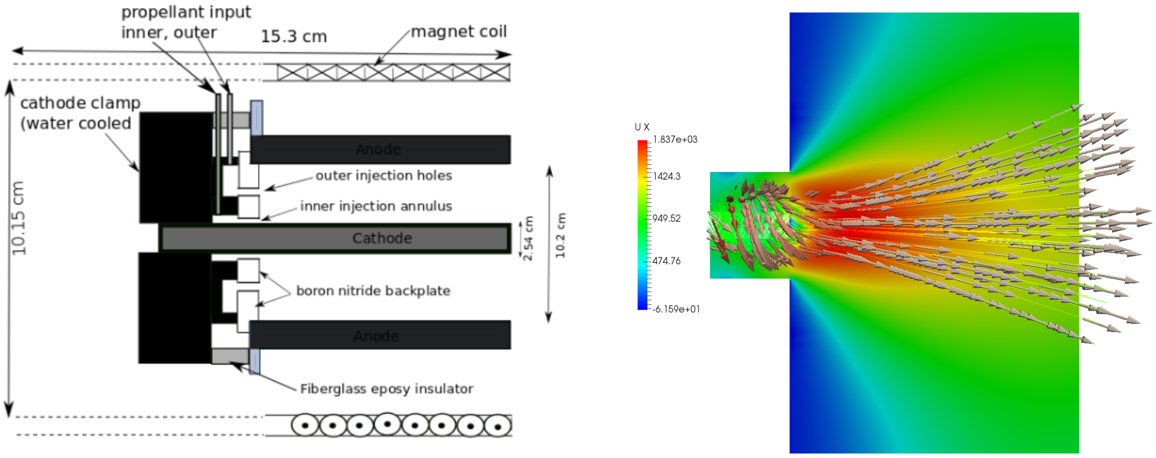

Fig. 1: Geometry of the applied field NASA Lewis Research Center's MPD thruster [1] (left) and axial component of velocity (Ux) [m/s] including velocity field vectors (right).

Outside the MPD thruster, the acceleration is based on the conversion of the above mentioned rotational energy via expansion in a magnetic nozzle which is formed by the diverge magnetic field lines. The induced azimuthal currents interact with the applied magnetic field to produce a radially confining electromagnetic force. The code reproduced the increase of thrust for both case as predicted by some previous modelling and analytic works.

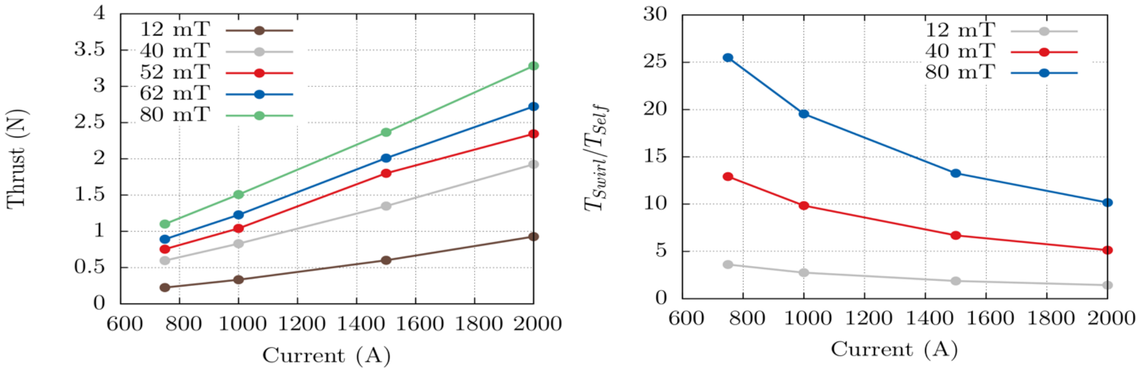

Fig. 2: Thrust [N] (left) and the ratio of swirl over self component of thrust (right) function of discharge current.

Outlook

In this project, we successfully used the developed density-based code for the simulations of the applied-field NASALeRC MPD thruster and the method presents ability to reproduce the theory of thrust production and plasma acceleration. For that we used a configuration with one external magnet and investigated the effect of applied magnetic strength and discharge current on the thruster performance. For the near future work it is planned to investigated the configuration (AFMPDT02) with two external magnets surrounding the discharge chamber in order to obtain a quasi uniform and horizontal applied field distribution near the anode to improve the thrust production as the swirl acceleration appeared as the most important component of thrust.

Publications

1. C. Chelem Mayigue, R. Groll, *Performance investigation of an argon fueled magnetoplasmadynamic thruster with applied magnetic fields,* In preparation for submission

Acknowledgement

This work is funded by the *Deutscher Akademischer Austauschdienst* (DAAD) through the "Research grants for doctoral candidates and young academics and scientists" programme (grant number 57076385).

References

1. G. Krulle, M. Auweter-Kurtz, A. Sasoh, *Technology and application 335 aspects of applied field magnetoplasmadynamic propulsion*, Journal of Propulsion and Power 14 (5) (1998) 754–763. doi:10.2514/2.5338.
2. G. P. Mikellides, J. P. Turchi, F. N. Roderick, *Applied-field magnetoplasmadynamic thrusters, part 1: Numerical simulations using the mach2 code*, Journal of Propulsion and Power 16 (2000) 887–893. doi:10.2514/2.5656.

5.7 ***hbi00032:*** **Plasma-Electrode Coupled Simulation Using Finite Volume Method**

HLRNProject ID:	hbi00032
Run time:	III/2016 –II/2017
Project Leader:	Dr.-Ing. Rodion Groll
ProjectScientists:	Peng Liang
Affiliation:	ZARM, University of Bremen

Overview

This project utilizes a newly developed and universally applicable method to simulate the plasma-electrode interaction in a D.C. plasma torch using the finite volume method. The open source CFD software OpenFOAM is developed based on its default solver chtMultiRegionFoam. Due to the atmospheric working condition, the arc jet developed during the arc discharge can be generally regarded as a continuous flow using the one-fluid two-temperature equation along with the Navier–Stokes equations. For an extra inclusion of the chemical nonequilibrium, which is prevailing in non-thermal plasmas, the ionization and excitation non-equilibrium rates are calculated according to Lotz's model (Fig.1):

$$\nabla \cdot (n_i \vec{u}) = -\nabla \cdot \vec{j}_{D,i} + \omega_i, \qquad (1)$$

where i=0~3, referring to heavy species from neutral atoms up to triply charged argon ions, $\vec{j}_{D,i}$ is the mass diffusion flux for heavy species.

$$\vec{j}_{D,i} = -n_s D_{fi} \nabla\left(\frac{n_i}{n_s+n_e}\right) - \xi_i \sum_{m=0}^{3}\left(-n_s D_{fm} \nabla\left(\frac{n_m}{n_s+n_e}\right)\right), \qquad (2)$$

where n_s is the total heavy species number density, ξ_i is the mass fraction of species i. D_{fi} is the effective diffusion coefficient,ω_i is the net production rate for species i:

$$\omega_i = -n_i n_e k_{f,i+1} + n_{i+1} n_e^2 k_{b,i+1} - n_i n_e^2 k_{b,i} + n_{i-1} n_e k_{f,i}, \qquad (3)$$

where $k_{f,i}$ and $k_{b,i}$ are the reaction rates of impact ionization and three-body re-combination.

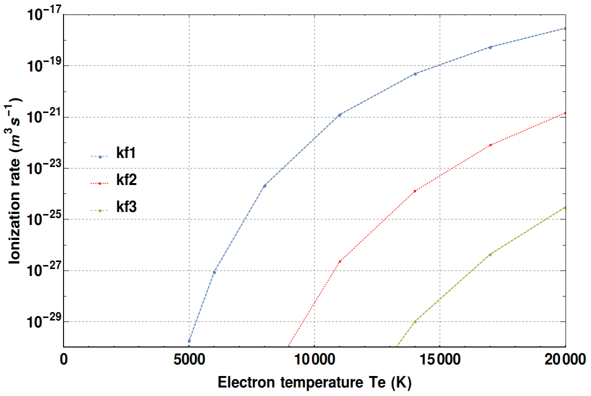

Fig. 1: Impact ionization rate from Lotz model

The sheath layer, key to the coupled simulation of plasma and electrodes, especially the cathode, is treated in this scope as a single layer represented by the boundary cells at plasma-cathode interface. This is achieved by replacing the local electrical conductivity obtained for bulk plasma in this place by the effective sheath electrical conductivity:

$$\sigma_{eff}=\frac{1}{\frac{1}{\sigma_{child}}(1-I_g)+\frac{1}{\sigma}I_g}, \quad (4)$$

where σ is the value of electrical conductivity used for quasi-neutral bulk plasma, I_g is ionization degree attained by the non-equilibrium composition calculation. σ_{child} is a value attained according to the Child Law for the collisionless high voltage sheath. By using the following relation, the continuity of electric potential at the interface could be guaranteed (Fig.2):

$$\sigma_{eff}A\frac{\varphi_{cp}-\varphi_p}{\Delta x_p} = \sigma_s A\frac{\varphi_p-\varphi_{cs}}{\Delta x_s}, \text{ (cathode sheath)} \quad (5)$$

$$\sigma_p A\frac{\varphi_{cp}-\varphi_p}{\Delta x_p} = \sigma_s A\frac{\varphi_p-\varphi_{cs}}{\Delta x_s}. \text{(other interfaces)} \quad (6)$$

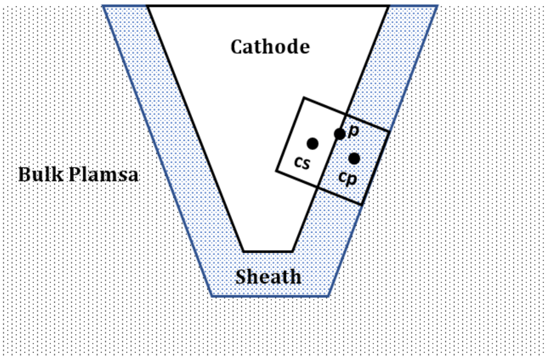

Fig. 2: Schematic description of boundary cell parameter configurations

Results

The simulation is performed based on the geometry of the Praxair SG-100 plasma-spray torch with a thoriated tungsten cathode, a coaxial tubular copper anode and a steel substrate under 700 A direct-current with pure argon under atmospheric condition as working gas (60 slpm, 45°swirl).The numerical results of both situations (2T and sheath) are presented (Fig.3 and 4), the predicted time-resolved voltage magnitude and fluctuation attained by sheath model is much more realistic when compared with experimental results (Fig.5). Besides, we have found out that the arc instability in plasma region could lead to the fluctuation of cathode surface temperature and emission current simultaneously, as well as a rotating feature of anode attachment (Fig.8).

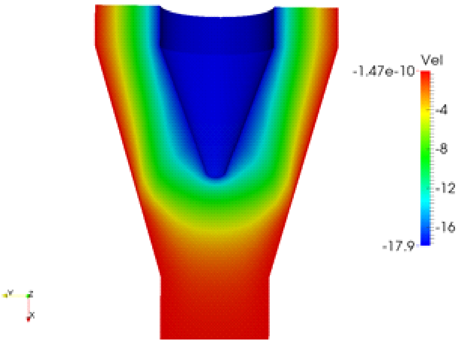

Fig. 3: Distribution of electric potential from 2T

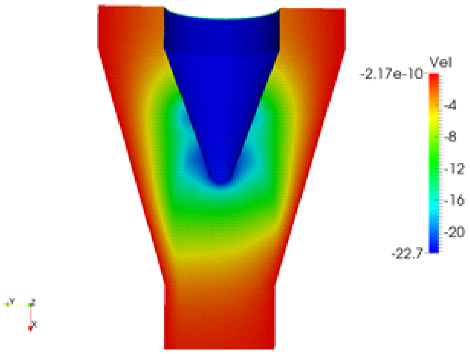

Fig. 4: Distribution of electric potential from sheath model

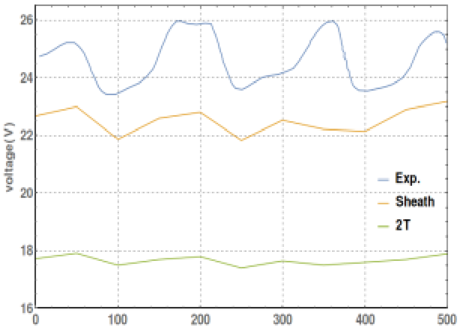

Fig.5. Predicted results of both situations in comparison with experimental results

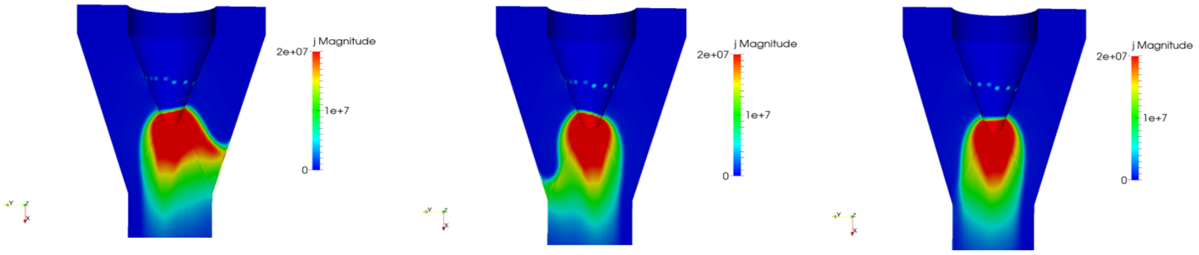

Fig. 6: Transient current density profile scaled under $2\times 10^7 \mathrm{A}/m^2$ at different observation points: point1(left), point2(middle), point3 (right)

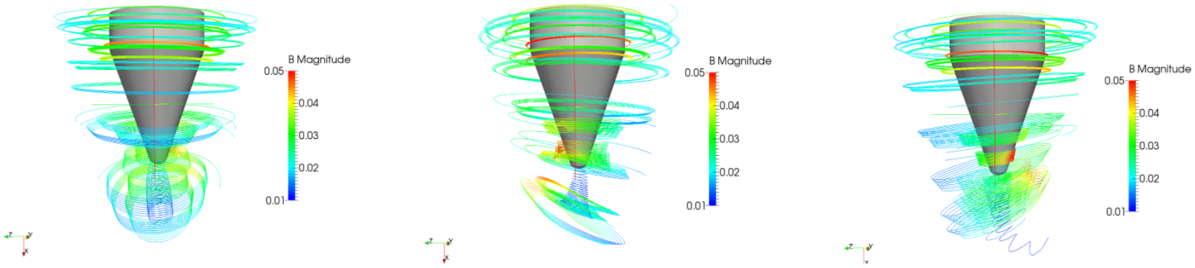

Fig. 7: Transient streamline profile of magnetic flux density scaled under 0.05T at different observation points: point1(left), point2(middle), point3 (right)

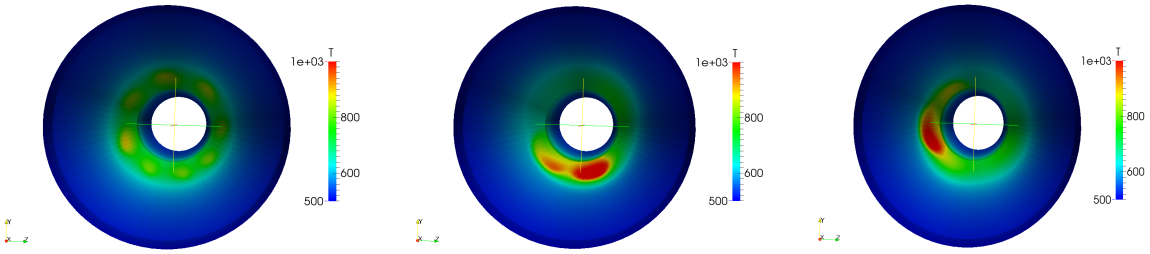

Fig. 8: Transient temperature profiles at plasma-anode interface of: 2T situation(left), and sheath situation in point 1(middle), point2(right)

Outlook

At present our numerical research considers only the basic aspect of plasma-electrode interaction, more sophisticated process such as melting and evaporation of electrodes and its effects on plasma properties will be taken into consideration as the next step to make the interaction model more universally applicable.

Publications

1. Peng Liang and RodionGroll. Numerical Study of Plasma–Electrode Interaction During Arc Discharge in a DC Plasma Torch. IEEE Transactions on Plasma Science. 2018;46: 363 – 372.

5.8 ***hbi00033:*** **Flow transitions and regimes in core-annular pipe flow**

HLRN Project ID:	hbi00033
Run time:	01/2017 – 12/2017
Project Leader:	Prof. Marc Avila
Project Scientists:	Dr. Baofang Song, Carlos Plana
Affiliation:	ZARM - Center of Applied Space Technology and Microgravity

Overview

In this project we planned to investigate the flow regimes in core-annular flow and the transition between them, using the phase-field method to capture the interface between the two fluids. Ultimately we aim at a phase-diagram of the flow regimes in terms of nondimensional system parameters such as the nominal Reynolds number of the two fluids, and aim to understand the bifurcations occuring at the regime boundaries. Considering the potentially very large drag reduction in transport of heavy oil in pipelines using the core-annular flow configuration, which was the concept of core-annular flow originally conceived for, in this project we mainly focused on the heavy oil-water system. The core-annular flow of this system was experimentally investigated in the literature but there is rare theoretical analysis of the flow regimes and the transition between them. These experimental studies provide good validation for our numerical method and good starting point for refining the phase-diagram and for the eventual bifurcation study on the regime boundaries. To our knowledge, there have been no quantitative studies of this system using phase-field method, given the very large viscosity ratio between oil and water (about 600). Therefore, we carried out simulations to reproduce the established typical flow configurations.

Results

In the run time of the project, we have completed the following studies:

1. We systematically investigated the Cahn-Hilliard-Navier-Stokes (CHNS) system of phase field method in case of core-annular flow and particularly studied the convergence to the sharp interface when the model interface width (measured by the Cahn number) decreases. CHNS is a complex system. The parameters Cahn number (Cn), Peclet number (Pe), and the time scale within the interfacial region which determines the numerical time-step size Δt, are correlated. In principle, given Cn the optimal Pe has been determined to be $Pe_o = 1/3Cn$ in the literature, however, in practice Pe largely determines the time-step size that is needed to fully resolve the Cahn-Hilliard equation. The optimal Pe may result in very restrictive time-step sizes. For practial use, we spent a lot of time on investigating a proper Pe range, instead of a single optimal $Pe_o = 1/3Cn$. We found that the range $0.1Pe_o \lesssim Pe \lesssim 10Pe_o$ can give systematic and super-linear convergence to the sharp interface solution, at least in core-annular flow situation. Besides, a lot of effort has been invested in investigating the influence of the Pe on the Δt for a given Cn. We found that when Pe is varied, Δt has to be changed accordingly in order to fully resolve the Cahn-Hilliard equation (in the literature Δt is only set to meet the numerical stability criteria). Lower Pe allows larger Δt and we found a nearly inverse proportionality between the two parameters for convergence. For example, $0.1Pe_o$ allows a Δt that is one order of magnitude larger than that allowed by Pe_o for comparable accuracy. Therefore, we pointed

out that the lower end of the range $0.1\mathrm{Pe}_o \lesssim \mathrm{Pe} \lesssim 10\mathrm{Pe}_o$ should be used in practical simulations. These aspects of the method have not been carefully studied in the literature.

2. We simulated a bamboo wave flow in water-heavy oil core-annular flow with large viscosity contrast. The very high viscosity ratio of 601 between heavy oil and water requires very thin interfacial region in our simulation, i.e. very small Cn are needed to closely approximate the sharp interface solution. In our simulation Cn = 0.002 and 0.001 are needed, which are much smaller than the typical values used in the literature (≃0.01), where usually only fluids with matching viscosity or comparable viscosities were considered. In practically relevant problems, such as heavy oil transport and gas-liquid core-annular flow systems high viscosity ratios are usually present. Very small Cn, meaning very high spatial resolution, together with very small Δt are required for convergence towards the sharp interface solution, making the simulations very costly. Besides, the forming of bamboo waves is a long process, which takes millions of integration steps with the time-step sizes on the order of 10^{-5}. It took a long time to obtain correct linear growth rate and nonlinear bamboo waves. Nevertheless, the bamboo wave flow regiem was successfully obtained in our simulations, and we obtained good quantitative agreement with the hold-up ratio in the nonlinear regime of the flow as reported in the literature, see figure 1. We showed that the result converges to the reference result as Cn decreases, if the parameters Cn, Pe and Δt are selected consistently.

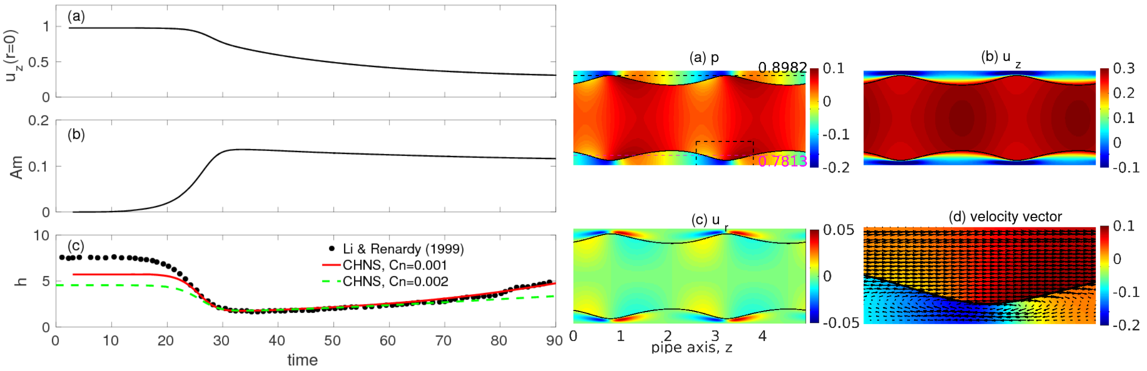

Figure 1: (left) The centreline velocity $u_z(r=0)$, nonlinear wave amplitude (Am) and the hold-up ratio obtained with our CHNS code with the comparison with the hold-up ratio calculated by Li & Renardy, *J. Fluid Mech. (1999), vol. 391, pp.* 123-149 using volume of fluid method. (right) The flow field of the bamboo wave flow: pressure field (a), streamwise velocity (b), radial velocity (c) and the velocity vectors near the wave crest (d) marked by a dashed window in pabel (a). The bold black line shows the position of the interface between water and heavy oil.

3. We performed a 3-D high resolution simulation of a fully turbulent core-annular flow simulation, with a grid size of 85 million grid points. The density of the two fluids are set the same and the viscosity of the core fluid is set to be three times as that of the annular fluid. The flow starts from perfect core-annular configuration with fully turbulent velocity perturbations. The interface is gradually distorted by the underlying turbulence and eventually is torn by turbulent fluctuations, and 3-D turbulent bamboo waves were observed during the development of the flow, see figure 2. Our code allows us to explore the 3-D regimes of core-annular flow, e.g. the disturbed core-annular flow, slug flow, bubble flow, and even dispersion flow.
4. Based on the aforementioned studies, we finished one manuscript “Approaching the sharp interface limit of the phase-field method in core-annular flows” which is ready for submission.

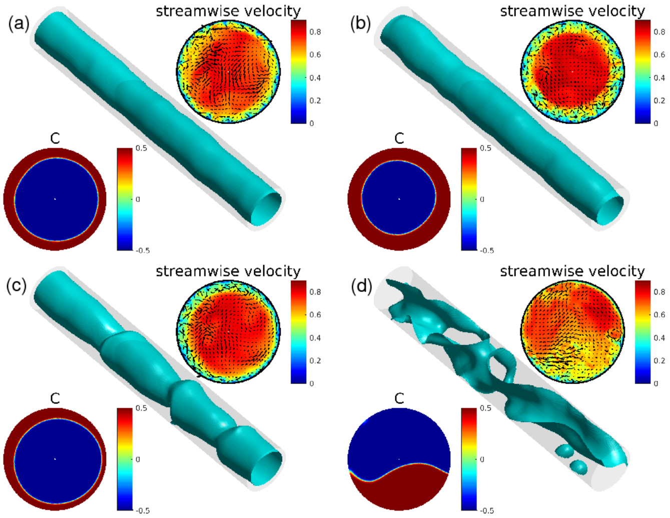

Figure 2: Snapshots of the interface in a core-annular flow perturbed by a fully turbulent velocity field, and the parameters are set such that the flow is inertia dominant (inertia effect outweigs that of surface tension and of viscosity). The initial cylindrical interface is positioned at 0.8R where R is the pipe radius. The streamwise velocity field and the concentration (C) field on the pipe cross section at the left end of the pipe are plotted. Blue region in C field plot (left-bottom corner of each panel) represents the more viscous core flow and represents low speed region in the streamwise velocity plot (right-top corner of each panel). The core-annular configuration (panel a) is perturbed and becomes twisted (panel b), then the bamboo wave-like flow configuration appears (panel c), and eventually the interface is torn by the underlying turbulence and the core flow touches the pipe wall (panel d).

Outlook

Currently, we are trying to locate the slug flow regime by obtaining a slug flow in our simulations. However, we showed that in numerical simulations that it is difficult to match the flow parameters of experiments, in which water and oil volume flow rates are set at the pipe inlet. To simulate the experiment situation, it takes long distances in the pipe for the flow to evolve toward a stabilized configuration, which requires a very large computation domain and makes it very expensive for a numerical code to simulate this spatial development, especially when the thin interface has to be resolved. In our simulations, we have to use relatively short periodic pipe to reproduce the flow regimes, but cannot use the same input parameters as in experiments. To reproduce the flow regime diagram as shown in the literature is the main task but is also a challenge for our on-going work.

Once the slug flow regime is obtained, we can approach the boundary between the bamboo wave and slug flow regimes. The slugging process, i.e. the transition from bamboo wave regime to the slug flow regime, is the most important as annular flow (perfect core-annular flow, bamboo waves, disturbed core-annular flow) allows efficient transport of heavy oil in pipelines, while slugging can significantly decrease the transport efficiency. Besides, the slug flow regime separates the bamboo wave regime and the bubble flow and dispersion regimes. It is of great importance to study this slugging process and develop techniques to suppress this process, which is our focus of our project.

Publications

B. Song, J. Lopez, A. Marc, Approaching the sharp interface limit of phase-field method in core-annular flows, *to be submitted*

5.9 *hbi00035: Numerical modelling of dynamo process in Taylor-Couette setup*

HLRN Project ID	hbi00035
Run time:	I/2017 - I/2018
Project leader:	Prof. Dr. Marc Avila
Project scientists:	Anna Guseva
Affiliation:	ZARM, University of Bremen

Overview

Dynamo theory was first developed to explain the sustainability of magnetic field of the Earth by conversion of mechanical energy to magnetic energy through the stretching, lifting and twisting of magnetic field lines by the flow field. The flow in planets and stars is governed by the balance between differential rotation and convection, whereas the influence of magnetic field on the flow is weak. The onset of this kinematic dynamo is a linear instability problem: the initial seed field will be exponentially amplified if dissipation effects are relatively weak. Cowling's theorem states that the flow also must possess non-zero helicity, i.e. must be non-axisymmentric at least on average.

Yet outside of a planetary or solar context, another question becomes important: can a magnetic field be maintained by the small-scale turbulence? Turbulent flows often have no mean helicity since the flow is disorganized. In those flows, dynamo can arise through a competition between the stretching of small-scale magnetic flux tubes by the velocity field and Ohmic dissipation of these flux tubes. This type of dynamo is extremely relevant for accretion disk flows (often called Keplerian).

Keplerian flows can be destabilized by imposed magnetic fields of specific shape and finite amplitude. This process, called magnetorotational instability (MRI), yields turbulence which is effective in angular momentum transport. However, existence of such imposed fields is unlikely the case in accretion disks. Explicit evidence for magnetic field in disks is sparse, and it is often believed that magnetic field arise from some original seed field due to the dynamo action. Axisymmetric flows like Keplerian with angular velocity profile of $\Omega \backsim r^{-3/2}$ can not yield dynamo action, according to Cowling's theorem. Nevertheless, small turbulence created via MRI-action is a flow of sufficient complexity to make dynamo possible. Therefore, the problem becomes highly nonlinear: infinitesimally small magnetic fields would be damped, but an initial magnetic field of sufficient amplitude could yield a configuration which maintains both the turbulence and the magnetic field.

In this project, we aimed to study the dynamics and transport properties of self-sustained dynamo process in Taylor-Couette flow. This setup, consisting of two co-rotating cylinders, under certain conditions is a good approximation of Keplerian flows and is often used for building laboratory experiments of rotating flows. By performing direct nonlinear simulations (DNS) we investigated the dynamo for various relevant parameters (magnetic Prandtl and magnetic Reynolds numbers).

Results

The existence of a finite-amplitude dynamo was demonstrated. A small-scale dynamo operating in Rayleigh-stable flows is observed for *Pm = 10* and *Rm* = 10^5. The resulting magnetic field is small-scale and shows no decay over more that one thousand inner cylinder rotations. The respective mean magnetic field is essentially zero, so as magnetic flux through the cylinder boundaries. With Lorentz force being slightly larger than Coriolis force, this dynamo belongs to the so-called strong field dynamos (Dormy, 2016). Interestingly, although turbulence modifies significantly the mean profile of azimuthal velocity, the mean angular velocity profile remains very close to the initial quasi-Keplerian profile.

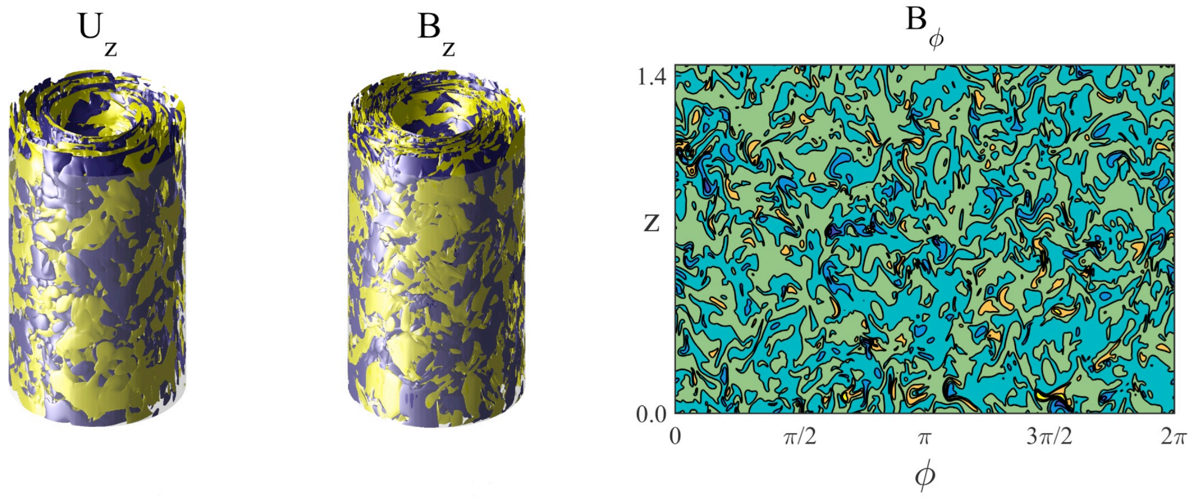

Figure 1: Instantaneous velocity and magnetic fields of the self-sustaining dynamo. From left to right: isosurfaces of velocity with u_z = ± 0.01 $[\Omega_i r_i]$ and magnetic field, B_z = ± 100 in $(\mu_0\rho)^{0.5}\ \nu\ /\ \delta$ scale, contours of B_ϕ on the unrolled cylinder at mid-gap *(r = 1.5). Pm=10 (Rm=*10^5*).*

To visualize this turbulence, instantaneous isosurfaces and contours of velocity and magnetic fields were plotted (Fig. 1). Both velocity and magnetic field have small-scale structure in all three directions, with magnetic field structures (Fig. 1, middle) being smaller than velocity field pattern (Fig. 1, left). Meridional slices (Fig. 1, right) show some clustering of vortices at the inner cylinder but otherwise no clear boundary layer structure. Neither velocity nor magnetic field exhibit periodicity or large-scale vortices comparable with the system's dimensions.

It is important to know at which parameter values the dynamo disappear, in order to probe the possibility of its operation in accretion disks. Since *Pm=10 (Rm=*10^5*)* results in dynamo and *Pm=1 (Rm=*10^4*)* relaminarises, there is likely a critical *Rm* (or *Pm*), where the dynamo ceases to exist. We approached this problem fixing *Re*=10^4 and varying *Pm* (and therefore *Rm*). Several simulations show that the dynamo dies out between Rm = 4.5 $\cdot 10^4$ and 5 $\cdot$ 10^4 (Figure 2a). A more precise definition of Rm_c is a subject for future work.

Taylor--Couette flow between two cylinders and Keplerian flows of accretion discs are similar in many aspects. Nevertheless, the presence of walls in the Taylor-Couette setup is a crucial difference between the two geometries and may influence some aspects of nonlinear equilibrium. Particularly, the average angular velocity of accretion disks can not deviate much from Keplerian. If gravity from the central object is the dominant force, it will always enforce $\Omega \sim r^{-3/2}$ no matter how intense the turbulence is.

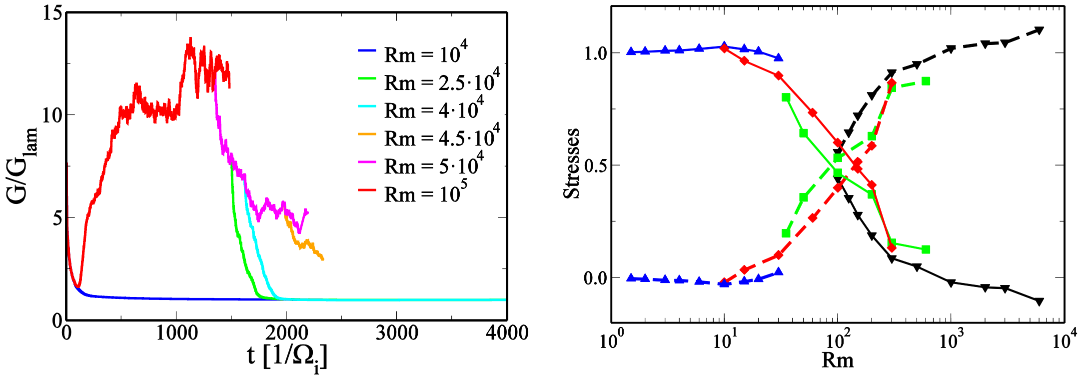

Figure 2: (a) Critical *Rm* for the dynamo. Reynolds number is fixed to *Re*= 10^4, *Pm* varied. (b) Reynolds (solid), Maxwell (dashed) and viscous (dots) stresses along the gap between cylinders at *Pm=10* (Rm= 10^5).

We performed an additional simulation, where the flow is forced to be quasi-Keplerian. The result was that the turbulence does not die out even if Keplerian rotation is imposed, showing similar stress distribution. The primary role in angular momentum transport plays Maxwell stress, being 10 times more efficient than Reynolds in both forced and non-forced setups (Figure 2b). This forced-flow results suggest that the dynamo presented here is generic to any Rayleigh--stable differential rotation flows, including flows in accretion disks, and is not specific only to Taylor--Couette flows. This argument is also confirmed by the absence of attached eddies at the wall, implying the near-wall turbulence does not define the flow structure.

Outlook

We explored the possibility of MRI-turbulence to be self-sustained in the absence of imposed magnetic fields. A small-scale dynamo operating in Rayleigh-stable flows is observed for *Pm* > *1* and *Rm* > *4.5* · 10^4. These values are huge for magnetohydrodynamic experiments on Earth but not unrealistic in the astrophysical context. The existence of such dynamo suggests that accretion disks can generate self-sustained magnetic fields without relying on large-scale fields from the central object. It is a matter for future research to map out the full range of parameters where the dynamo operates. The important question here is whether the dynamo is possible for lower *Pm* as well. Although it is not entirely clear whether vortices of inertial range or large-scale motions are responsible for the dynamo at low *Pm*, it is known that higher critical *Rm* are required (Schekochihin et al., 2007). Due to the computational complexity of the problem, requiring simultaneous solution of nonlinear equations for velocity and magnetic field, we plan to address the mechanisms of the dynamo in the subsequent work.

The results of this project confirm the applicability of Taylor--Couette system for modelling of magnetized rotating flows and provide a useful framework for further astrophysical studies of Keplerian flows. Further work should shed more light on the sensitivity of the dynamo to the initial condition and magnetic Prandlt number *Pm*.

Publications

Guseva, A.P. Willis, R. Hollerbach, M. Avila. *Dynamo action in a quasi-Keplerian Taylor-Couette flow.* Physical Review Letters, 119, 164501 (2017).

Presentations

Guseva, A.P. Willis, R. Hollerbach, M. Avila. *Dynamo Action in a Quasi-Keplerian Taylor-Couette Flow.* GDRI Dynamo Meeting, November 27-29, 2017, Paris, France.

5.10 *hbi00036:* Fluiddynamische Untersuchung der Stressbeanspruchungen proteinstabilisierter o/w-Phasengrenzflächen beim Premix-Membranemulgieren

HLRN-Projektkennung:	hbi00036
Laufzeit:	II/2017 – I/2018
Projektleiter:	Prof. Dr.-Ing. Udo Fritsching
Projektbearbeiter.	Laura Luhede
Institut / Einrichtung:	Fachbereich 4, Universität Bremen

Überblick

Emulgierverfahren werden im Rahmen des Downstream-Prozessierens und der Weiterverarbeitung/Formulierung zur Homogenisierung oder auch Verkapselung in biogenen Produkten eingesetzt. Beim Premix-Emulgieren wird eine grobdisperse Voremulsion mittels der Dispergierung in porösen Membranen in eine Feinemulsion bzw. -Dispersion überführt. Insbesondere das Stress-Verweilzeitverhalten und die darauf erfolgende Reaktion eines proteinstabilisierten dispersen Systems bedarf einer vertieften wissenschaftlichen Klärung. Hieraus können mechanistische Schädigungsmodelle abgeleitet werden. Die im Emulgier-Prozess auftretenden mikromechanischen Belastungen auf biologische Systeme sind nicht vollständig geklärt, die Prozessumgebung ist somit noch weiter zu entwickeln im Hinblick auf die Anpassung an spezielle biologische Systeme.

Der Fokus dieses Forschungsvorhabens liegt auf der Beschreibung des mehrphasigen fluiddynamischen Prozesses beim Premix-Emulgieren in porösen Strukturen. Der Einfluss von Scher- und Dehnkräften auf die Grenzfläche ist von besonderem Interesse für die Untersuchung von Tropfenaufbruchskriterien beim Premix-Emulgieren, sowie zur Bestimmung der dabei entstehenden Belastung der an Phasengrenzen adsorbierten Proteine. Ziel des Projekts ist es die Kriterien für Tropfendeformation und –Aufbruch zu ermitteln und anhand der Belastungen auf die Grenzfläche zu quantifizieren. Ergebnisse dieses Forschungsvorhabens werden von einem weiteren Projekt (Molekulardynamische Untersuchung der Stressbeanspruchung auf Proteine an der Phasengrenzfläche beim Premix-Membranemulgieren, hbi00037) zur Ermittlung von Stressbelastungen auf Proteine beim Premix-Membranemulgieren genutzt.

Ergebnisse

Es wurde ein Modell zur Beschreibung von Scher- und Dehnkräften an der Phasengrenze entwickelt und in die Open Source Software OpenFOAM implementiert. Die Validierung erfolgte an einer mehrphasigen Couette Strömung.Komplexere System wurden behandelt, indem das Scher-Stress-Verweilzeitverhalten von Tropfen in verschiedenen idealisierten Porenstrukturen untersucht wurde. Im Folgenden wird das Verweilzeitverhalten anhand einer Verengung von einer großen Kapillare in eine kleinere dargestellt (Vgl. Abbildung 1).

Exemplarisch sind in Abbildung 1 die Tropfendeformation verschiedener Tropfen-durchmesser (300 – 500 µm) bei konstanter Geschwindigkeit (u = 0, 012 m/s) zu sehen. Es fällt auf, dass sich kleinere Tropfen schneller durch das System bewegen als die Größeren, da sie eine geringere Deformation erfahren und somit schneller von der Kapillarwand gelöst werden. Dadurch sinkt die Wandreibung und die Geschwindigkeit steigt gegenüber den größeren

Tropfen. Man sieht deutlich, dass sich der Tropfenaufbruch mit der Tropfengröße zu späteren Zeitpunkten verschiebt. Nach Tropfenaufbruch nehmen die Tropfen, wie bei der kleinsten untersuchten Tropfengröße ein Taylorblasen ähnliches Verhalten ein.

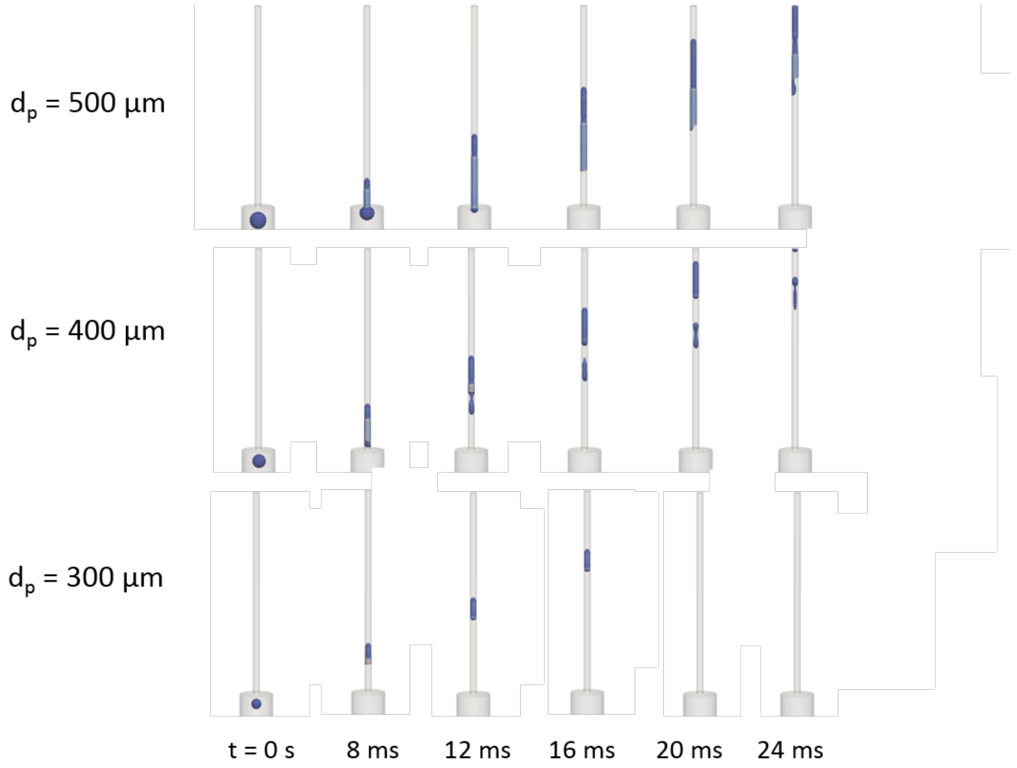

Abbildung 1: Tropfendeformation in einer Verengung von verschiedenen Tropfendurchmessern bei einer konstanten Geschwindigkeit von 0,012 m/s

Interessant zu beobachten ist außerdem, dass sich hintere Teile der größeren Tropfen an einer Wandseite anlagern anstatt sich über den gesamten Kapillarquerschnitt zu verteilen. Der gleiche Effekt wurde im Experiment unter ähnlichen Strömungsbedingungen entdeckt (Abbildung 2).

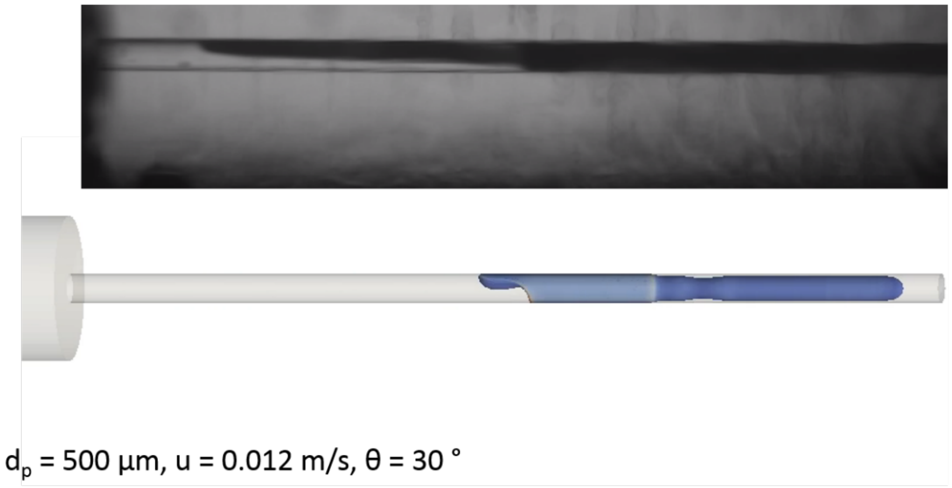

Abbildung 2: Vergleich der Simulation mit einem Experiment unter ähnlichen Randbedingungen

Das Scher-Verweilzeitverhalten des 400 µm großen Tropfens wird in Abbildung 3 gezeigt. Man sieht die die Scherkräfte über die Position des Tropfens während des Aufstiegs aufgetragen (Abbildung 3a). Deutlich zu erkennen sind die Dehnung des Tropfens sowie der Tropfenaufbruch (bei Aufspaltung des Graphen). Die Scherraten zeigen einen Anstieg am unteren Ende des Tropfens, das heißt an dem Teil, der durch Reibungskräfte festgehalten wird und dadurch eine Kraft auf die Grenzfläche erfährt. Der obere Teil weist moderate Scherraten auf, nachdem die Deformation nach der Verengung erfolgt ist. Deutlicher zu erkennen ist dieser Trend bei Betrachtung der auf den Tropfen wirkenden Dehnkräfte (Abbildung 3b).

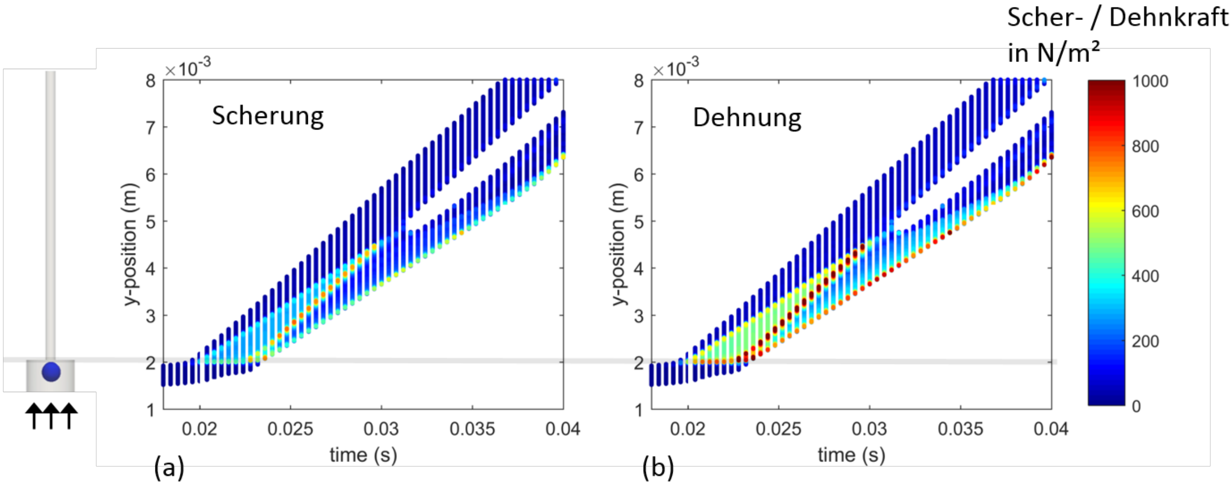

Abbildung 3: Verlauf der (a) Scher- und (b) Dehnkräfte eines 400 µm großen Tropfens über die Simulationsdomain

Dehn- und Scherkräfte sind sich im Verlauf ähnlich, wobei die Dehn- die Scherungskräfte überwiegen. Vergleicht man nun alle Tropfendurchmesser (Abbildung 4) zeigt sich, dass die maximalen Dehnkräfte mit dem Durchmesser ansteigen. Der Anstiegt der Dehnungsrate zum Eintritt des Tropfens in die Kapillare ist deutlich sichtbar und die Steigung in der Dehnkraft für alle Tropfen sehr ähnlich. Alle Tropfen weisen einen kurzen Abfall in der maximalen Dehnkraft auf, sobald der obere Teil der Tropfen anfängt sich von der Kapillarwand zu lösen. Darauf steigt die gesamte Dehnkraft jedoch wieder an, da sich der Anteil an Tropfen bereits in der Kapillare und damit in Wandnähe weiter erhöht.

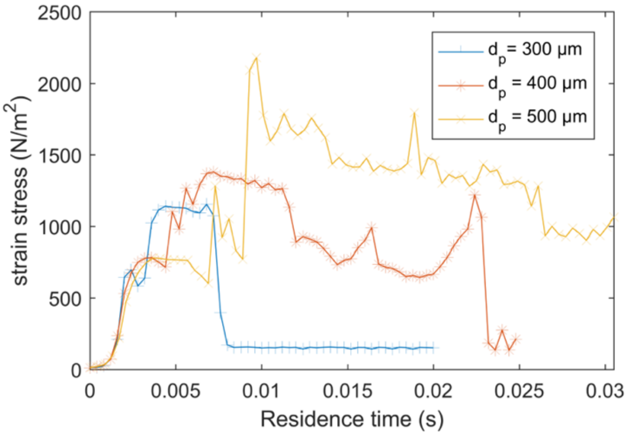

Abbildung 4: Vergleich der maximalen Dehnkräfte für verschiedene Tropfendurchmesser

Für den 300 µm Tropfen ist deutlich zu erkennen, dass er sich am schnellsten von der Wandreibung löst, da die Dehnkraft stark abnimmt. Auch ist zu erkennen, dass er sich am schnellsten durch die vorgegebene Geometrie bewegt. Für den 400 µm Tropfen löst sich neben dem Kopf auch der hintere Teil (zur Hälfte) von der Wand, was zu einer leichten Reduktion in der maximalen Dehnkraft führt. Erkennbar ist der Tropfenaufbruch, an diesem Punkt findet eine sprunghafte Reduktion der Dehnkraft statt. Im weiteren Verlauf kommt es zu einem erneuten Anstieg, in dem sich der neu entstandene Tropfen ein weiteres Mal dehnt, aber anstatt wieder zu reißen zurückfedert. Beide Tropfen erreichen kurz vor Ende der Domain ihren Endzustand, welcher an der abgefallenen Dehnkraft sichtbar ist.

Für den größten Tropfen ist der Verlauf Ähnlich, die Dehnkraft nimmt mit zunehmender Ablösung der Grenzfläche von der Kapillarwand ab, wie beim 400 µm Tropfen bildet sich ein an einer Seite anliegender Schwanz aus. Es ist zu sehen, dass mit Ende der Domain noch keine finale Tropfenform erreicht ist, der Vergleich der Tropfenform mit dem 400 µm Tropfen lässt aber sehr auf einen späteren Zerfall schließen.

Ausblick

Im laufenden Projekt wurden Einwirkungen von Scher- und Dehnkräften auf Einzeltropfen in Modellstrukturen untersucht. Es konnte gezeigt werden, dass Tropfendeformation und – Aufbruch auf Änderungen in den Dehn- und Scherkräften an den Phasengrenzen erfolgen. Das neue Modell erlaubt es, die an den Phasengrenzen wirkenden Kräfte mit der porösen Struktur in Verbindung zu setzen. Im nächsten Arbeitsschritt werden nun komplexe Strukturen wie Computer Tomographie Scans eingesetzt um reale System abbilden zu können. Aus den gewonnen Daten kann dann im nächsten Schritt eine Korrelation für das Scher-Stress-Verweilzeitverhalten gefunden werden.

Vorträge / Poster

1. T. Wollborn, L. Luhede, U. Fritsching, *Modeling of interfacial shear and strain stresses in multiphase systems*, OpenFOAM User Group Meeting, Chalmers University, Göteborg, 17.11.2017
2. T. Wollborn, L. Luhede, U. Fritsching, *Modellierung und Simulation des Grenzflächenspannungszustands bei der Tropfendeformation in flüssig-slüssig Systemen*, Jahrestreffen der PorcessNetFachgruppen MFA, TRO und GFSP, Halle/Merseburg, 26.02.-28.02.2018
3. L. Luhede, T. Wollborn, U. Fritsching, *Analyse des Grenzflächen-Spannungszustands bei der Deformation von Tropfen in flüssig-flüssig Systemen*, Jahrestreffen der PorcessNetFachgruppen MPH, WSUE und CFD, Bremen, 05.-07.03.2018

5.11 *hbi00037:* Molekulardynamische Untersuchung der Stressbeanspruchungen auf Proteine an der Phasengrenzfläche beim Premix-Membranemulgieren

HLRN-Projektkennung:	hbi00037
Laufzeit:	II/2017 – II/2018
Projektleiter:	Prof. Dr.-Ing. Udo Fritsching
Projektbearbeiter.	Tobias Wollborn
Institut / Einrichtung:	Fachgebiet Mechanische Verfahrenstechnik, Universität Bremen, Deutschland

Überblick

Emulgierverfahren werden im Rahmen des Downstream-Prozessierens und der Weiterverarbeitung/Formulierung zur Homogenisierung oder auch Verkapselung in biogenen Produkten eingesetzt. Beim Premix-Emulgieren wird eine grobdisperse Voremulsion mittels der Dispergierung in porösen Membranen in eine Feinemulsion bzw. -dispersion überführt. Insbesondere das Stress-Verweilzeitverhalten und die darauf erfolgende Reaktion eines protein-stabilisierten dispersen Systems bedarf einer vertieften wissenschaftlichen Klärung. Hieraus können mechanistische Schädigungsmodelle abgeleitet werden. Die im Emulgier-Prozess auftretenden mikromechanischen Belastungen auf biologische Systeme sind nicht vollständig geklärt, die Prozessumgebung ist somit noch weiter zu entwickeln im Hinblick auf die Anpassung an spezielle biologische Systeme.

Um den Einfluss des Premix-Emulgierverfahrens und der dabei auftretenden Stress-Verweilzeit-Belastungen auf die agglomerierten Proteine im Fluid und an den Phasengrenzflächen zu untersuchen, werden numerische Untersuchungen auf molekulardynamischer Ebene an Proteinstrukturen durchgeführt. Diese Untersuchungen zeigen, inwieweit die Proteinstrukturen durch den Emulgiervorgang belastet und geschädigt werden können, beziehungsweise ob eine proteinschonendere Emulgierung mit den Membranen möglich ist.

Ergebnisse

Innerhalb der letzten Förderperiode wurden insgesamt zwei Schwerpunkte untersucht. Der erste Schwerpunkt befasste sich mit der Adsorption von Proteinstrukturen an einer Öl-Wasser-Phasengrenzfläche. Der zweite Schwerpunkt mit der Untersuchung der Auswirkungen von in Strömungen auftretenden Dehn- und Scherbelastungen auf die adsorbierten Strukturen.

Adsorption der Proteine an der Phasengrenzfläche:

Im ersten Arbeitspaket wurde zunächst die Adsorption von Einzelproteinen an der Öl-Wasser-Phasengrenzfläche untersucht, um bevorzugte Adsorptionskonfigurationen ausfindig zu machen. Es konnte gezeigt werden, dass abhängig vom eingestellten pH-Wert unterschiedliche Adsorptionskonfigurationen auftreten und das Protein in allen Fällen eine Affinität hin zur Phasengrenzfläche zeigt. Da sich das Protein innerhalb seiner Startkonfiguration in der wässrigen Phase befindet, wird vermutet, dass vor allem die hydrophoben Aminosäuren des Proteins für diese Affinität hin zum Öl verantwortlich sind. Eine Analyse der nach Adsorption mit der Phasengrenzfläche interagierenden Aminosäuren zeigt allerdings, dass es sich bei einem großen Teil dieser Aminosäuren um hydrophile Anteile des

Proteins handelt, was der Annahme widersprechen würde. Die Ursache dafür zeigt eine Analyse der Proteinstruktur während des Adsorptionsvorgangs. Abbildung 5a) zeigt dazu die hydrophilen (rot) und hydrophoben (blau) Aminosäuren des Proteins. Wie zu erkennen ist, liegen die hydrophilen Aminosäuren in wässriger Lösung erwartungsgemäß weiter außen, als die Hydrophoben.

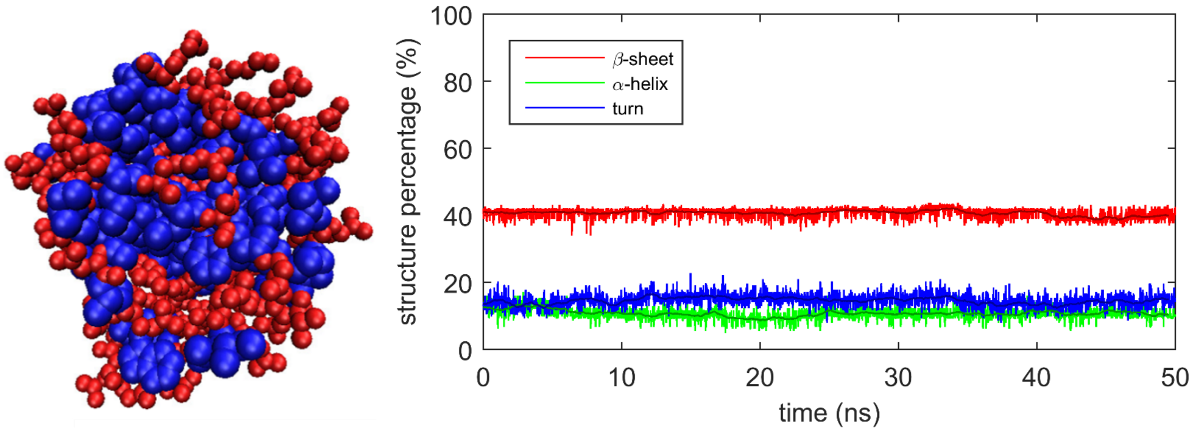

Abbildung 5: Hydrophile (rot) und hydrophobe (blau) Aminosäuren von b-Lactoglobulin (a) und Sekundärstruktur des Proteins während des Adsorptionsvorgangs (b)

Damit es zu einer Interaktion der hydrophoben Anteile mit der Phasengrenzfläche kommen kann, ist daher eine Änderung der Proteinstruktur (Entfaltung) erforderlich. Experimentell wurde die Proteinentfaltung an Öl-Wasser-Phasengrenzen in (Zhai et al., 2010) beschrieben. Ein Vergleich mit der Proteinstruktur während des simulierten Adsorptionsvorgangs in Abbildung 5b) zeigt allerdings, dass während des gesamten Simulationszeitraums die Proteinentfaltung ausbleibt und es so nicht zu einer stärkeren Adsorption der hydrophoben Aminosäuren an der Phasengrenzfläche kommt. Eine Ursache dafür könnte sein, dass die nötige Zeit für diese Entfaltung deutlich über der möglichen Simulationszeit liegt oder das Protein in einem Energieminimum liegt, dessen Überwindung im Rahmen der Simulation nicht möglich ist. Daher wurde für eine Überprüfung dieser These die kinetische Energie des Systems für einzelne Beispielkonfigurationen aus den vorherigen Untersuchungen erhöht (Erhöhung der Temperatur). Das Resultat in Abbildung 6 zeigt bei erhöhter kinetischer Energie eine deutliche Entfaltung des Proteins an der Phasengrenzfläche.

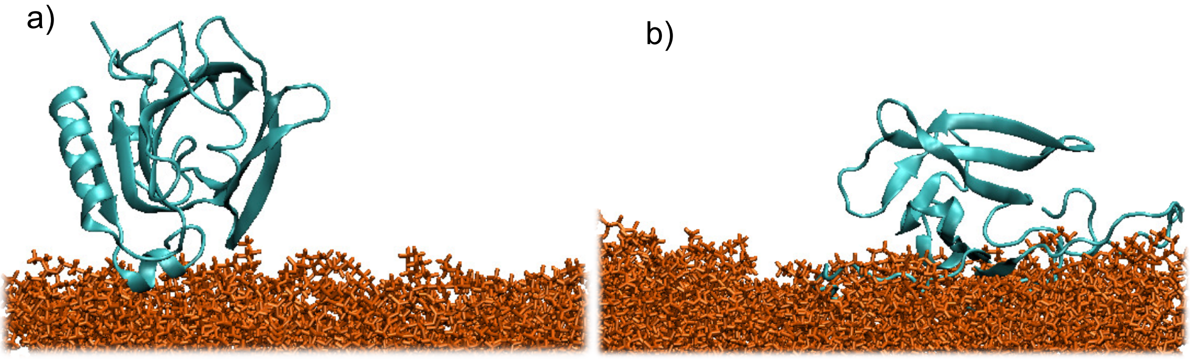

Abbildung 6: Protein an der Phasengrenzfläche vor (a) und nach Entfaltung (b)

Die Analyse der Kontaktstellen zwischen Protein und Grenzfläche weist zudem einen größeren Anteil an hydrophoben Aminosäuren auf, was die Anfangshypothese bestätigt. Das zeigt, dass bei erhöhter kinetischer Energie eine Überwindung der Barrieren zur

Strukturänderung möglich ist und sich die Aminosäuren des Proteins gemäß ihrer hydrophilen oder hydrophoben Neigung ausrichten können. Zudem lässt sich ein Rückgang der β-Faltblattstrukturen erkennen, wie in (Zhai et al., 2010) beschrieben wurde. Neben der Beschreibung der Orientierung des Proteins bei der ersten Anlagerung kann also zudem das weitere Verhalten an der Phasengrenzfläche in Form von den in der Literatur beschriebenen Strukturänderungen erläutert werden. Dadurch sind genauere Aussagen über den Zustand des Proteins an der Phasengrenzfläche möglich, die für die Betrachtung der Stressbeanspruchung entscheidend sein können. Da die dazu nötigen Simulation mit 200ns recht zeit- und kostenintensiv sind, konnte das Vorgehen innerhalb dieser Antragsperiode nicht auf die übrigen Konfigurationen angewandt werden. Daher sollen im folgenden Antragszeitraum weitere Untersuchungen bezüglich der Proteinentfaltung an der Phasengrenzfläche unternommen werden, um die Veränderung der Struktur qualitativ und quantitativ beschreiben zu können

Stressuntersuchungen an Proteinstrukturen an der Phasengrenzfläche:

Bei der Untersuchung des Stresseinflusses wurden die adsorbierten Proteinstrukturen durch Anlegung eines Schergradienten belastet. Bei niedrigen Scherraten verbleibt das Protein bei allen untersuchten pH-Werten in seiner Adsorptionskonfiguration und es treten keine Strukturänderungen in Form einer Proteinschädigung auf. Bei Erhöhung der Scherrate kommt es zu einer Ablösung des Proteins von der Phasengrenzfläche, wobei auch hier keine Veränderungen in der Proteinstruktur feststellbar sind. Bei einem Vergleich der Adsorptionskräfte mit den Kräften, die nötig sind die Proteinstruktur zu deformieren, konnte festgestellt werden, dass die Adsorptionskräfte um eine Größenordnung niedriger liegen und somit bei den aktuell untersuchten Konfigurationen eine Proteinschädigung an der Phasengrenzfläche unwahrscheinlich ist. Dieses Ergebnis ist zu erwarten, da bei den Adsorptionsvorgängen unter Standardbedingung (Raumtemperatur), wie bereits erwähnt, eine Entfaltung des Proteins ausbleibt und es somit in seiner stabilsten Form verbleibt. Zudem kann sich der Kontakt zwischen Protein und Phasengrenzfläche nicht richtig ausbilden und bereits niedrige Beanspruchungen sind ausreichend um für eine Desorption zu sorgen. Daher wurden auch die entfalteten Konfigurationen aus den Tests Scherbeanspruchungen ausgesetzt (siehe Abbildung 7).

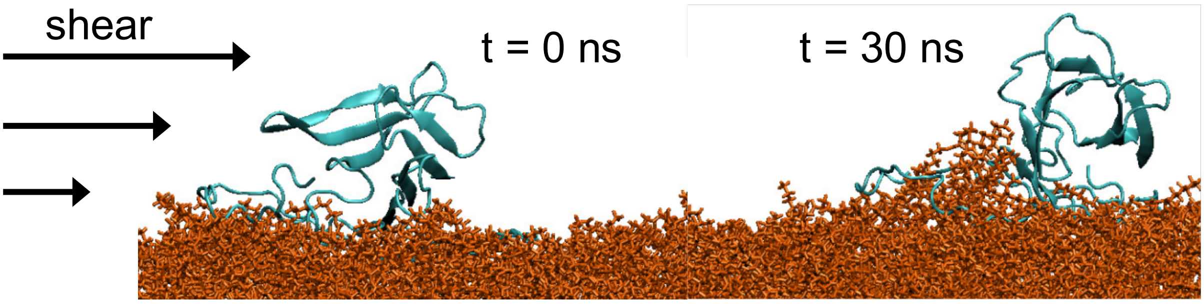

Abbildung 7: Protein an der Phasengrenzfläche vor Aufbringung des Scherstress (t = 0ns) und nach einer Simulationszeit von t = 30 ns

Die dabei verwendeten Scherraten liegen in derselben Größenordnung in der sie bei den nicht entfalteten Adsorptionskonfigurationen zu einer Desorption von der Phasengrenzfläche geführt haben. Bei der entfalteten Form in Abbildung 7 ist deutlich zu erkennen, dass es zu keiner Desorption kommt. Durch die Entfaltung an der Phasengrenzfläche kommt es zu einer deutlich höheren Anzahl an adsorbierten Aminosäuren und somit zu wesentlich höheren Haftkräften. Dadurch wird das Protein an der Phasengrenzfläche gehalten. Zudem bewirkt die Entfaltung eine Schwächung der Proteinstruktur, da ein Teil der dazu nötigen Energie bereits investiert wurde. Dadurch ist das Protein deutlich anfälliger gegenüber weiteren Beanspruchungen, was zu einer Deformation führt, wie sie beim Vergleich in Abbildung 7 (links und rechts) zu erkennen ist. Dies bestätigt die Wichtigkeit der Untersuchung der Strukturänderung an der Phasengrenze in Bezug auf die Stressbeanspruchung, wie sie für den nächsten Antragszeitraum vorgesehen ist.

Ausblick

Die hier dargestellten Untersuchungsergebnisse haben gezeigt, dass für verschiedene Versuchsparameter die bevorzugten Adsorptionskonfigurationen gefunden werden konnten. Es konnten allerdings keine, wie in der Literatur dargestellten, Konfigurationsänderungen beobachtet werden. Die beschriebenen Stresstests haben gezeigt, dass das Protein dabei in seiner nativen Form sehr widerstandsfähig ist und es anstelle einer Degradierung zur einer Desorption von der Phasengrenzfläche kommt. In weiteren Untersuchungen konnte jedoch durch Erhöhung der kinetischen Energie des Systems eine Entfaltung des Proteins an der Grenzfläche hervorgerufen und gezeigt werden, dass diese einen signifikanten Einfluss auf die Stressuntersuchungen hat. Dementsprechend ist eine Berücksichtigung der Proteinentfaltung an der Grenzfläche zwingend notwendig. Im weiteren Projektverlauf sollen daher die Untersuchungen zur Proteinentfaltung auf die verschiedenen betrachteten Prozessparameter ausgeweitet und der Effekt der Stressbelastung beschrieben, sowie mit den bisherigen Resultaten gegenübergestellt werden. Ein Vergleich zu den molekulardynamischen Untersuchungen soll experimentell mittels CD (Circular Dichroism) durchgeführt werden.

Literatur

Zhai, J., Miles, A. J., Pattenden, L. K., Lee, T., Augustin, M. A., Wallace, B. A., Aguilar, M.-I., Wooster, T. J. (2010). Changes in -Lactoglobulin Conformation at the Oil / Water Interface of Emulsions Studied by Synchrotron Radiation Circular Dichroism Spectroscopy, 2136–2142.

Vorträge / Poster

T. Wollborn, U. Fritsching, *Adsorption behavior of β-Lactoglobulin at liquid-liquid interfaces and degradation due to mechanical stresses*, CECAM 2017, Bremen, 12.-16.06.2017

5.12 *hbk00018:* Berechnung der Wasserdampfkonzentrationen aus Limb-Messungen des Satelliteninstruments SCIAMACHY

HLRN-Projektkennung:	hbk00018
Laufzeit:	I/2012 – III/2017
Projektleiter:	Dr. K. Weigel
Projektbearbeiter.	Dr. K. Bramstedt, Dr. A. Rozanov, Dr. M. Vountas
Institut / Einrichtung:	Institut für Umweltphysik (IUP), Universität Bremen

Überblick

Im Rahmen der DFG-Forschergruppe SHARP (engl.: Stratospheric Change and its Role for Climate Prediction) und der ESA-Projekte SPIN (engl: ESA SPARC Initiative) und SQWG (engl: SCIAMACHY Quality Working Group) haben wir eine neue Version für einen Wasserdampfdatensatz der oberen Troposphäre und unteren Stratosphäre berechnet. Grundlage der Berechnung sind SCIAMACHY (engl.: Scanning Imaging Absorption spectroMeter for Atmospheric CHartographY) Messungen. SCIAMACHY, ein Instrument auf dem europäischen Satelliten Envisat, lieferte von August 2002 bis April 2012 Messungen. Die veröffentliche Datenversion V3.01 wurde teilweise auf dem HLRN berechnet, beinhaltet aber nur einen Teil der auswertbaren Daten. Diese Zeitserie wird auch durch die Initiativen SPARC-DI (engl.: Stratospheric Processes and their Role in Climate - Data Initiative) und SPARC - WAVAS (engl.: Water Vapour Assessment) genutzt. Die neue Datenversion V4.2 ist die erste, bei der alle verwendbaren SCIAMACHY Messungen zur Berechnung von Wasserdampfprofilen ausgewertet wurden. Mögliche wurde dies mit einer Erweiterung von SCIATRAN, durch die zusätzlich zu OpenMP auch MPI genutzt werden kann. Gegenüber V3.01 wurde V4.2 zusätzlich insbesondere hinsichtlich der vertikalen Auflösung und der Aerosolkorrektur verbessert.

Ergebnisse

Wasserdampf in der Atmosphäre ist im Gegensatz zu Wassertröpfchen, die man als Wolken oder Nebel sehen kann, für das menschliche Auge unsichtbar. Trotzdem spielt er eine wichtige Rolle für den Strahlungstransport in der Atmosphäre, denn er absorbiert besonders gut Strahlung im infraroten Bereich und somit z.B. die von der Erde emittierte Wärmestrahlung. Für das kurzwelligere, sichtbare Licht ist er dagegen fast vollständig transparent. Dadurch ist er das wichtigste natürliche Treibhausgas. Der Wasserdampfgehalt der Atmosphäre schwankt stark, sowohl örtlich als auch zeitlich. Den höchsten Wasserdampfgehalt findet man üblicherweise nahe dem Erdboden. An der Tropopause, d.h. am Übergang zwischen Troposphäre und Stratosphäre gibt es meist besonders wenig Wasserdampf. Die Troposphäre reicht bis in eine Höhe von etwa 10 bis 18 km und ist die Schicht, in der sich die meisten Wetterphänomene abspielen. Wolken findet man beispielsweise meist in der Troposphäre und nur unter bestimmten Bedingungen in der Stratosphäre. Das Wasserdampfminimum in der Nähe der Tropopause (siehe auch Abb. 1) hat einen großen Einfluss auf den Strahlungstransport. Modellstudien haben gezeigt, dass Änderungen des Wasserdampfgehaltes dort auch das Klima am Boden beeinflussen können. Ziel des DFG Projektes SHARP (siehe auch: www.fu-berlin.de/sharp/) ist es, zu einem besseren Verständnis über die Verteilung und die zeitliche Änderung des Wasserdampfgehaltes in der Atmosphäre und dessen Wirkung auf das Klima beizutragen.

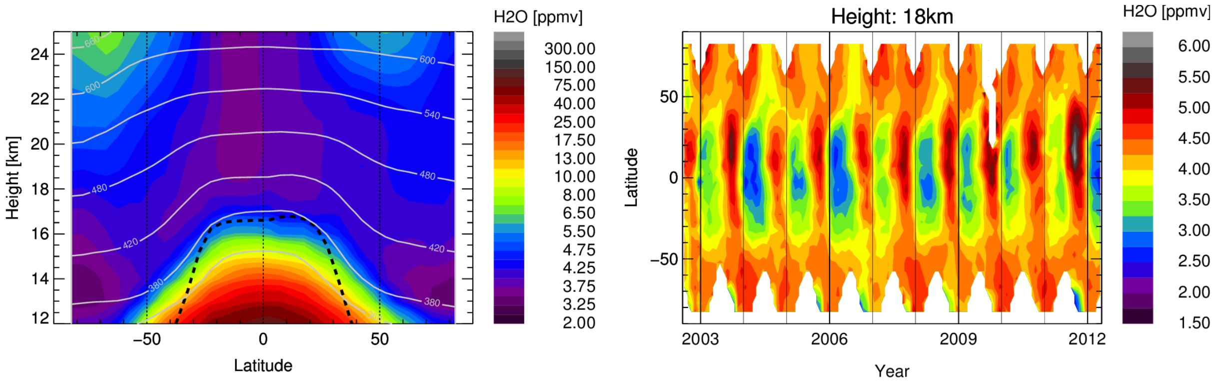

Abb. 8: Wasserdampf-Volumenmischungsverhältnisses Datenversion V4.2 berechnet aus SCIAMACHY Limb-Messungen. Links: Zonales Mittel des gesamten Datensatzes. Zusätzlich zeigen weiße Linien die Level potentieller Temperatur und die schwarze, gestrichelte Linie die Lage der Tropopause, beides berechnet aus ECMWF Reannalyse Daten. Rechts: Zeitserie in 18km Höhe gemittelt über alle Längengrade und 5° Breitengradbereiche.

Um dieses Wasserdampfminimum beobachten zu können braucht man sehr empfindliche Instrumente. Bodengebundene Messverfahren erreichen diesen Höhenbereich oft nur schlecht, Messungen von Ballonen und Flugzeugen sind nicht global und regelmäßig in ausreichender Qualität verfügbar. Limb-Messverfahren von Satelliteninstrumenten sind besonders gut geeignet um den Bereich der Tropopause zu beobachten. Bei diesem Messverfahren schaut das Instrument durch die Atmosphäre über den Erdboden hinweg in Richtung des Weltraumes und kann so verschiedene Höhen abtasten. Solche Messungen wurden von SCIAMACHY durchgeführt, einem Spektrometer an Bord des europäischen Satelliten Envisat. Beim Limb-Messverfahren tastet SCIAMACHY die Atmosphäre mit Höhenschritten von jeweils 3.3 km ab. Bei jedem Höhenschritt wird das Spektrum des in der Atmosphäre gestreuten Sonnenlichts über einen breiten Wellenlängenbereich aufgezeichnet. Absorptionslinien des Wasserdampfes im infraroten Bereich des Spektrums ermöglichen es, den Wasserdampfgehalt der Atmosphäre zu bestimmen. Das gemessene Spektrum wird außer vom Wasserdampfgehalt auch durch Druck, Temperatur und die Streuung in der Atmosphäre z.B. an Aerosolen und Wolken beeinflusst.

Um Wasserdampfprofile aus den gemessen Spektren zu bestimmen verwenden wir SCIATRAN (Rozanov et al., 2011). Dabei wird mit einem Strahlungstransportmodell aus einer gegebenen Atmosphäre ein solches Spektrum berechnet, wobei auch die Mehrfachstreuung modelliert wird. Um aus den Messungen und den modellierten Spektren auf Wasserdampfprofile in der Atmosphäre zu schließen sind aufwändige, inverse mathematische Verfahren nötig. Das Ergebnis sind Wasserdampfprofile zwischen ca. 10 und 25 km Höhe. Die Berechnungen erfolgen iterativ und der Zeitaufwand ist groß, unter anderem weil ein breiter Spektralbereich und ein dichtes Höhengitter verwendet werden müssen. Dazu kommt die große Zahl von Profilen, die berechnet werden kann. SCIAMACHY Messungen gibt es von August 2002 bis zum plötzlichen Kontaktverlust mit Envisat im April 2012. In diesem Zeitraum gibt es etwa 4.5 Millionen Limb-Messungen bei Tageslicht, die sich prinzipiell für die Berechnung des Wasserdampfgehaltes eignen. Das sind über 1000 Profile pro Messtag. Mit einem Wolkenfilter werden zunächst die Profile identifiziert, bei denen hohe Wolken eine Auswertung erschweren. Nach der Filterung bleiben etwa 700 Profile pro Messtag übrig, die Zahl der Profile reduziert sich besonders in der Nähe des Äquators. Deshalb wurde für die letzte Datenversion V3.01 nur jeder 8. Tag global und jeder 2.Tag zwischen 45°N und 45°S ausgewertet.

Die Datenversion V3.01 haben wir mit verschiedenen Datensätzen von anderen Satelliteninstrumenten und Ballonmessungen verglichen und die Berechnung anhand von simulierten Messungen überprüft, siehe Weigel et al. (2016). Die Wasserdampfdaten werden im Rahmen internationaler Initiativen wie SPARC-DI (engl.: Stratospheric Processes and their Role in Climate - Data Initiative) und SPARC - WAVAS (engl.: Water Vapour Assessment) zur Erforschung der Stratosphäre genutzt und mit anderen Daten verglichen, siehe Hegglin et al. (2013; 2014), Lossow et al. (2017) und Khosrawi et al., (2018). Der Datensatz wird auch bei einer Studie zu Polaren Stratosphärenwolken verwendet (Khosrawi et al., 2016).

Für die neue Datenversion V4.2 wurde die Rechenmethode verbessert, insbesondere hinsichtlich der Aerosolkorrektur und der Höhenauflösung. Mit der neuen SCIATRAN Version 3.5 ist es nun möglich, zusätzlich zur bisher verwendeten openMP Parallelisierung auch eine Parallelisierung mit Hilfe von MPI (engl.: message passing interface) zu verwenden. Dadurch konnten die Berechnung auf dem HLRN deutlich besser organisiert werden. Damit konnte für die Datenversion 4.2 erstmals der kompletten Datensatz ausgewertet werden. Abb. 1 zeigt das zonale Mittel des Wasserdampf-Volumenmischungsverhältnisses über den gesamten Datensatz und eine Zeitserie in 18 km Höhe.

Ausblick

Die Zeitserie für die Datenversion V4.2 wurde 2017 vervollständigt und das Projekt hbk00018 ist abgeschlossen.

Publikationen

1. Rozanov, A., Weigel, K., Bovensmann, H., Dhomse, S., Eichmann, K.-U., Kivi, R., Rozanov, V., Vömel, H., Weber, M., and Burrows, J. P., *Retrieval of water vapor vertical distributions in the upper troposphere and the lower stratosphere from SCIAMACHY limb measurements*, Atmos. Meas. Techn., 4, 933-954, doi:10.5194/amt-4-933-2011, 2011.
2. Hegglin, M. I., Tegtmeier, S., Anderson, J., Froidevaux, L., Fuller, R., Funke, B., Jones, A., Lingenfelser, G., Lumpe, J., Pendlebury, D. , Remsberg, E., Rozanov, A., Toohey, M., Urban, J., von Clarmann, T., Walker, K. A., Wang, R., Weigel, K.: *SPARC Data Initiative: Comparison of water vapour climatologies from international satellite limb sounders*, J.Geophys. Res., 118, 20, 11824–11846, doi: 10.1002/jgrd.50752, 2013.
3. Hegglin, M. I., Plummer, D. A., Shepherd, T. G., Scinocca, J. F., Anderson, J., Froidevaux, L. Funke, B., Hurst, D., Rozanov, A., Urban, J., von Clarmann, T., Walker, K. A., Wang, H. J., Tegtmeier, S., and Weigel, K.: *Vertical structure of stratospheric water vapour trends derived from merged satellite data*, Nature Geosc., 7, 768–776, doi:10.1038/ngeo2236, 2014.
4. Khosrawi, F., Urban, J., Lossow, S., Stiller, G., Weigel, K., Braesicke, P., Pitts, M. C., Rozanov, A., Burrows, J. P., and Murtagh, D.*: Sensitivity of polar stratospheric cloud formation to changes in water vapour and temperature*, Atmos. Chem. Phys., 16, 101-121, doi:10.5194/acp-16-101-2016, 2016.
5. Weigel, K., Rozanov, A., Azam, F., Bramstedt, K., Damadeo, R., Eichmann, K.-U., Gebhardt, C., Hurst, D., Kraemer, M., Lossow, S., Read, W., Spelten, N., Stiller, G. P., Walker, K. A., Weber, M., Bovensmann, H., and Burrows, J. P.: *UTLS water vapour from SCIAMACHY limb measurementsV3.01 (2002–2012)*, Atmos. Meas. Tech., 9, 133-158, doi:10.5194/amt-9-133-2016, 2016.
6. Lossow, S., Khosrawi, F., Nedoluha, G. E., Azam, F., Bramstedt, K., Burrows, John. P., Dinelli, B. M., Eriksson, P., Espy, P. J., García-Comas, M., Gille, J. C., Kiefer, M., Noël, S., Raspollini, P., Read, W. G., Rosenlof, K. H., Rozanov, A., Sioris, C. E., Stiller, G. P., Walker, K. A., and Weigel, K.: *The SPARC water vapour assessment II: comparison of annual, semi-annual and quasi-biennial variations in stratospheric and lower mesospheric*

water vapour observed from satellites, Atmos. Meas. Tech., 10, 1111-1137, doi:10.5194/amt-10-1111-2017, 2017.

7. Khosrawi, F., Lossow, S., Stiller, G. P., Rosenlof, K. H., Urban, J., Burrows, J. P., Damadeo, R. P., Eriksson, P., García-Comas, M., Gille, J. C., Kasai, Y., Kiefer, M., Nedoluha, G. E., Noël, S., Raspollini, P., Read, W. G., Rozanov, A., Sioris, C. E., Walker, K. A., and Weigel, K.: *The SPARC water vapour assessment II: Comparison of stratospheric and lower mesospheric water vapour time series observed from satellites*, Atmos. Meas. Tech. Discuss., https://doi.org/10.5194/amt-2018-33, in review, 2018.

Vorträge / Poster

1. Weigel, K., Rozanov, A., Azam, F., Bramstedt, K., Kowalewski, S., Eichmann, K.-U., Noël, S., Weber, M., Bovensmann, H., and Burrows, J. P.: *A new version of water vapour profile data from SCIAMACHY limb measurements*, ESA Living Planet Symposium 2016 - LPS16, Praha, 12.05.2016.
2. Weigel, K., Rozanov, A., Azam, F., Bramstedt, K., Eichmann, K.-U., Stiller, G. P., Weber, M., Bovensmann, H., and Burrows, J. P.: *Validation of SCIAMACHY Limb Water Vapour V4.2*, Atmospheric Composition Validation and Evolution Workshop - ACVE 2016, ESA/ESRIN, Italy, 18-20 October 2016.
3. Weigel, K., Rozanov, A., Azam, F., Bramstedt, K., Eichmann, K.-U., Malinina, E., Weber, M., Bovensmann, H., and Burrows, J. P.: SCIAMACHY limb measurements - one decade of observations in the upper troposphere and stratosphere, WCRP/SPARC workshop: "Challenges for Climate Science - Synergies between SPARC and the WCRP Grand Challenges", Berlin, 31 October - 1 November 2016.

5.13 ***hbk00032:*** Improving physics and efficiency of AWI-CM multi-resolution climate model

HLRN-Projektkennung:	hbk00032
Laufzeit:	III/2017 – II/2018
Projektleiter:	Prof. Dr. Thomas Jung[1,2]
Projektbearbeiter.	Dmitry Sidorenko[2], Dirk Barbi[2], Sergey Danilov[2], Helge Gößling[2], Ozgur Gurses[2], Sven Harig[2], Jan Hegewald[2], Nikolay Koldunov[2], Thomas Rackow[2], Natalja Rakowsky[2], Patrick Scholz[2], Dmitry Sein[2], Tido Semmler[2], Qiang Wang[2], Claudia Wekerle[2]
Institut / Einrichtung:	[1] also at University of Bremen [2] Alfred-Wegener-Institute for Polar and Marine Research, Bremerhaven

Summary

FESOM is the global sea-ice ocean circulation model based on unstructured meshes. It allows to simulate the global ice-ocean system with extremely high resolutions in the regions of interest at affordable computational cost. The new version of FESOM (Finite-volumE Sea ice–Ocean Model FESOM 2.0, Danilov et al. 2017) has emerged recently and promises a significant improvement in the performance of the ocean component as compared to its previous version 1.4. Therefore, it has been decided to replace the old version with FESOM 2.0 in both types of applications in coming years: the standalone ocean simulations and coupled model (AWI-CM2.0) simulations. In this project we validate and improve FESOM2.0 and AWI-CM2.0. The validation is accompanied with the extensive comparison between 2.0 and 1.4 versions.

FESOM v.2.0

FESOM 2.0 builds upon FESOM1.4 (Wang et al., 2014) but differs by its dynamical core. FESOM 2.0 exploits the finite volume approach with the cell centered placement of horizontal velocities (quasi-B-grid). This speeds up the dynamical core of FESOM by a factor of 3 compared to the finite element implementation in version 1.4. For vertical discretization the new version exploits the Arbitrary Lagrangian Eulerian Method. This allows users to switch between different discretizations which already include linear/non-linear free-surface, Z star, partial cell etc. The model inherits the framework and sea ice model from the previous version, which minimizes the efforts needed from a user to switch from one version to the other.

AWI-CM v.2.0

AWI-CM climate model is built upon FESOM and coupled with the latest version of ECHAM6.3 (Stevens et al. 2013) atmosphere from the Max Planck Institute for Meteorology, Hamburg (AWI-CM climate model; Sidorenko et al., 2015, Rackow et al., 2016). Using FESOM as the ocean component allows to simulate the global climate system with reduced biases at affordable computational cost. Both components are coupled via the parallel OASIS3-MCT coupler developed at Centre Européen de Recherche et Formation Avancée en Calcul Scientifique (CERFACS). AWI-CM2.0 and AWI-CM1.0 differ only in the ocean and sea components (FESOM 2.0 vs. 1.4).

Benefits from multi-resolution

The qualitative comparison of both versions of FESOM has been made using a mesh with moderate resolution and under the standard set of model configurations. It has been shown that the new version provides results with quality comparable to that of FESOM 1.4 (see et al. Danilov et al. 2017). Although the impact of vertical transport schemes, bottom representation and boundary conditions remains to be explored in more detail, the speedup in the code performance of the new FESOM version allows for configurations which are not affordable with the older versions.

Taking advantage of the improved code performance we addressed the role of multi-resolution using two meshes with ~5,000,000 wet surface nodes. The resolution of the first mesh is similar the regular grid STORM configuration of the Max Planck Institute Ocean Model (MPIOM, Marsland et al., 2002) and is shown in Fig.1 (left panel). In the second configuration (FESOM-XR, right panel in Fig.1) we used a similar amount of surface nodes but redistributed them with some density function designed according to the ocean eddy active. The principles underlying the mesh design are explained in detail in Sein et al. (2016, 2017).

The results show, that FESOM 2.0 simulates richer dynamics with FESOM-XR than with the STORM mesh. Furthermore, FESOM-XR simulates more realistically the Gulf Stream separation, shows richer dynamics in the Nordic Seas and simulates the Azore current. Provided that the computational cost between both setups is nearly the same, we conclude that the multi-resolution approach provides substantial advantages against traditional regular-grid-based models. This is still to be demonstrated in more detail in upcoming studies.

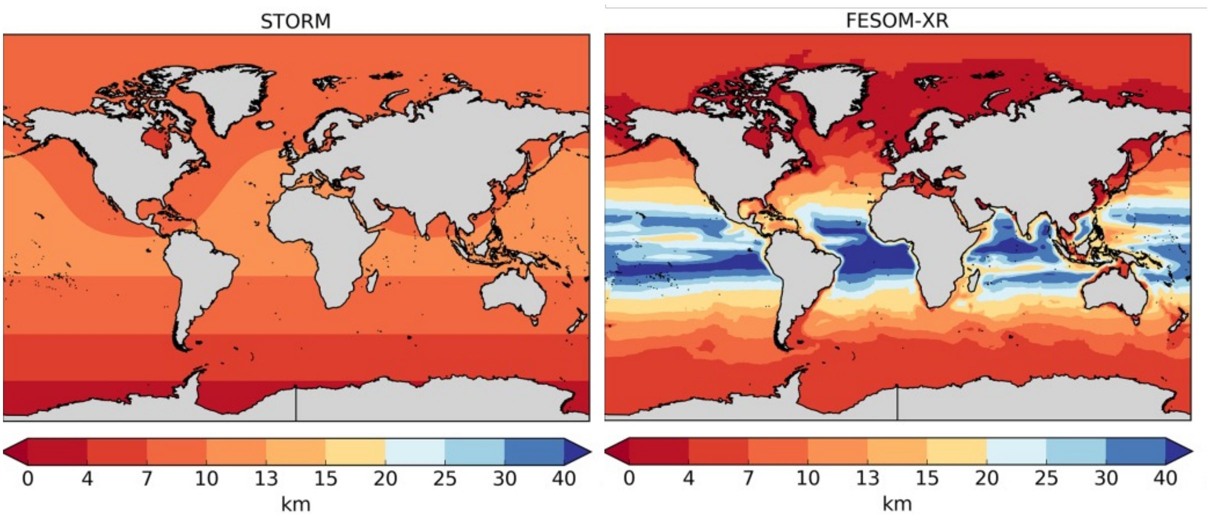

Fig. 1: Horizontal resolutions (km) of the FESOM model grids: the STORM (left) and FESOM-XR (right) meshes.

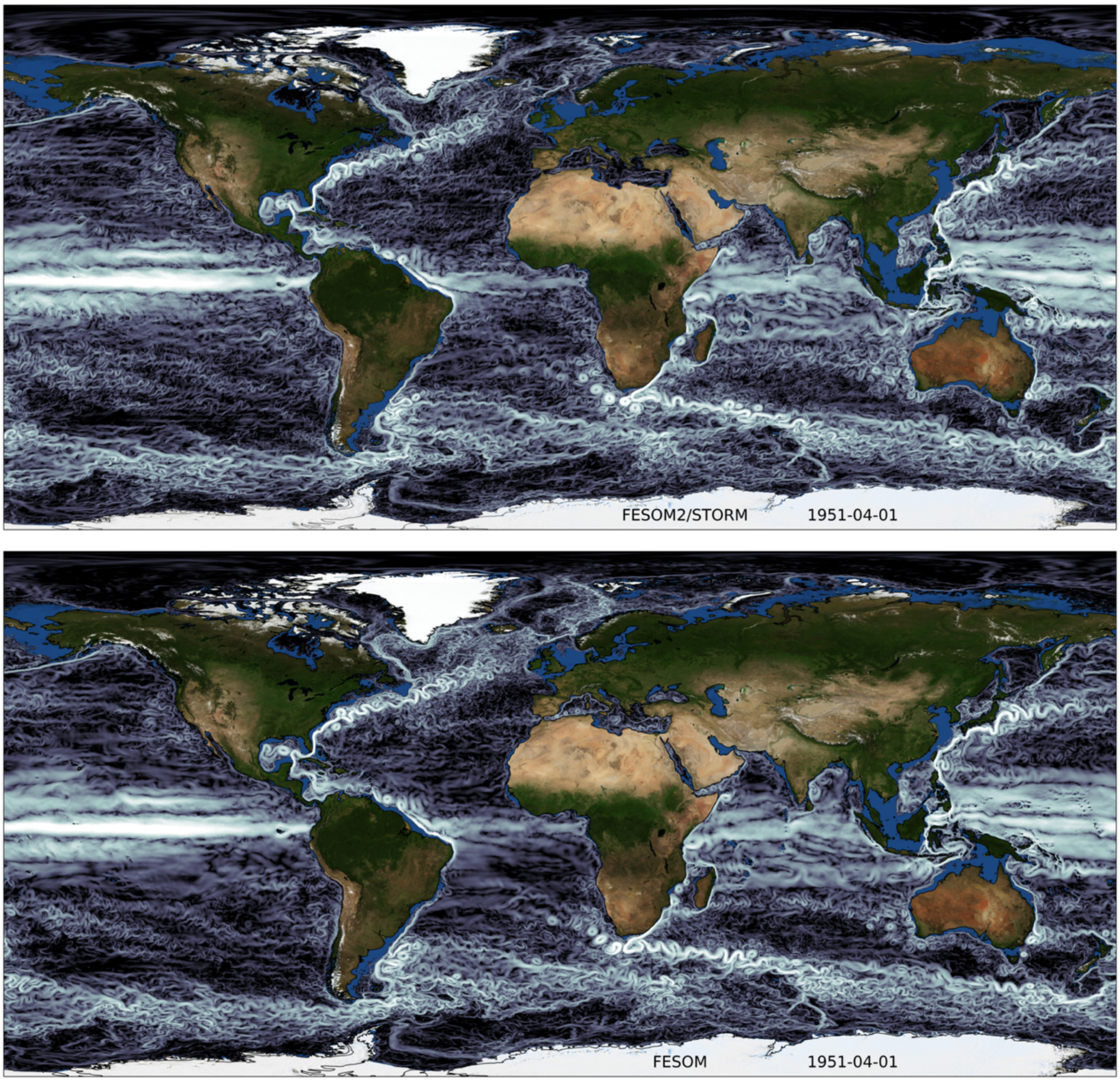

Fig. 2: Snapshots of absolute velocities at 100m depth simulated with FESOM 2.0 using the STORM (upper panel) and FESOM-XR (lower panel) meshes.

References

Danilov, S., Sidorenko, D., Wang, Q., and Jung, T.: The Finite-volumE Sea ice–Ocean Model (FESOM2), Geosci. Model Dev., 10, 765-789, 2017, doi: 10.5194/gmd-10-765-2017

Rackow, T. and co-authors (2016), Towards multi-resolution global climate modeling with ECHAM6-FESOM. Part II: climate variability, Clim. Dyn. doi:10.1007/s00382-016-3192-6

Sein, D. V., Danilov, S., Biastoch, A., Durgadoo, J. V., Sidorenko, D., Harig, S., Wang, Q. (2016). Designing variable ocean model resolution based on the observed ocean variability. Journal of Advances in Modeling Earth Systems, 8(2), 904-916.

Sein, D. V., Koldunov, N. V., Danilov, S., Wang, Q., Sidorenko, D., Fast, I., ... & Jung, T. (2017). Ocean modeling on a mesh with resolution following the local Rossby radius. Journal of Advances in Modeling Earth Systems, 9(7), 2601-2614.

Sidorenko D. and co-authors (2015). Towards multi-resolution global climate modeling with ECHAM6–FESOM. Part I: model formulation and mean climate, Climate Dynamics, doi:10.1007/s00382-014-2290-6

Stevens, B. and co-authors, 2013: Atmospheric component of the MPI-M Earth System Model: ECHAM6. Journal of Advances in Modeling Earth Systems, 5(2), 146-172, doi:10.1002/jame.20015

Wang, Q. and co-authors (2014), The Finite Element Sea Ice-Ocean Model (FESOM) v.1.4: formulation of an ocean general circulation model, Geosci. Model Dev., 7 (2), 663-693, doi:10.5194/gmd-7-663-2014.

5.14 hbk00034: Ice sheet - ice shelf - ocean interaction in the marginal seas of the Southern Ocean

HLRN Project ID::	hbk00034
Run time:	III/2013-III/2018
Project Leader:	Prof. Torsten Kanzow[1,2]
Project Scientists:	Dr. Mathias van Caspel[2], Svenja Ryan[2], Janin Schaffer[2], Frank Schnaase[1], Lukrecia Stulic[2], Dr. Ralph Timmermann[2]
Affiliation:	[1] University of Bremen [2] Alfred Wegener Institute, Helmholtz Centre for Polar and Marine Research

Overview

In this project we use a global sea ice – ice shelf – ocean model to study the interaction between the deep Southern Ocean, the ice shelves fringing the Antarctic continent, and the Antarctic Ice Sheet. With its unstructured grid, the Finite Element Sea ice – Ocean Model (FESOM) allows for an adequate resolution of the key regions, namely the grounding lines, the ice shelf fronts, and the continental shelf break. We are particularly interested in water mass exchange between the deep ocean and the continental shelf, and the pathways of water in the sub-ice cavities. We have developed a coupled ocean – ice shelf - ice sheet model, which enables us to investigate the relevant processes in decadal to centennial-scale simulations in a consistent way. With the high computational burden imposed by the use of a finite-element ocean model (to which there is no alternative if local processes are to be represented in a global system), the project depends on resources provided through the HLRN.

Results

We have completed and published a suite of centennial-scale simulations with the coupled Regional Antarctic and Global Ocean (RAnGO) model; results have been published in *Ocean Science* (see https://www.ocean-sci.net/13/765/2017/). As already highlighted in the 2016 report, RAnGO is based on a global FESOM configuration with an eddy-permitting mesh in the Weddell Sea sector of the Southern Ocean and an even further refinement in the sub-ice cavities. It is coupled to an implementation of the three-dimensional ice dynamics model RIMBAY that comprises the Filchner Ronne Ice Shelf (FRIS) and the ice streams in its catchment area up to the ice divides.

RAnGO simulations with a 20th-century climate forcing yield realistic basal melt rates and a quasi-stable grounding line position close to the presently observed state. In a centennial-scale warm-water-inflow scenario forced with A1B scenario data from the HadCM3 climate model, RAnGO suggests a substantial thinning of the ice shelf and a local retreat of the grounding line, with the strongest anomalies occuring near the grounding line of Suport Force Glacier. This is caused by an increase of ice shelf basal melt rates by a factor of six between the simulated 1990s and the projected 2190s; maximum melt rates near the grounding line increase from 4 to 15 m/yr. Simulated ice-shelf thickness is reduced by almost 25 % near the grounding line of Support Force Glacier (Fig. 1). A comparison to a control simulation with the same atmospheric forcing but a constant ice shelf geometry reveals that the potentially negative feedback from ice-shelf thinning through a rising in-situ freezing temperature in the coupled model is more than outweighed by the increasing water column thickness and the steeper slope of the ice shelf base in the deepest parts of the cavity (Fig. 2). Compared to the control simulation with fixed ice-shelf geometry, the coupled model thus yields a slightly stronger increase of ice-shelf basal melt rates. At the end of the 22nd century, increasing ice flow from the continent has contributed an additional 12 mm to global sea level rise. This regime shift does not occur in two control simulations (coupled/uncoupled) with a perpetual 20th-century forcing from the same climate model and can thus clearly be attributed to the climate scenario/forcing data used.

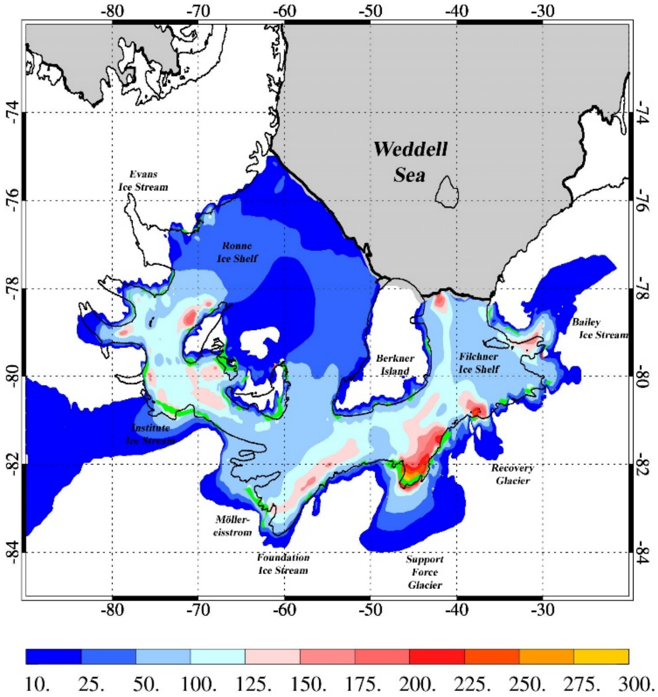

Fig. 1 Simulated thinning of ice shelf and grounded ice (m) between 1995 and 2195. Green patches denote areas that become ungrounded.

Further activities in this project have focussed on

- an improved representation of Weddell Sea circulation and hydrography in eddy-resolving simulations, on
- a multi-parameter optimization of sea ice model parameters using the Green's functions approach, and on
- the quantification of sea ice net growth in the Weddell Sea and the relevant feedback between sea ice formation and regional-scale hydrography.

These projects have proceeded well and will very like lead to pear-reviewed publications this year. Results will be highlighted in the report for 2018.

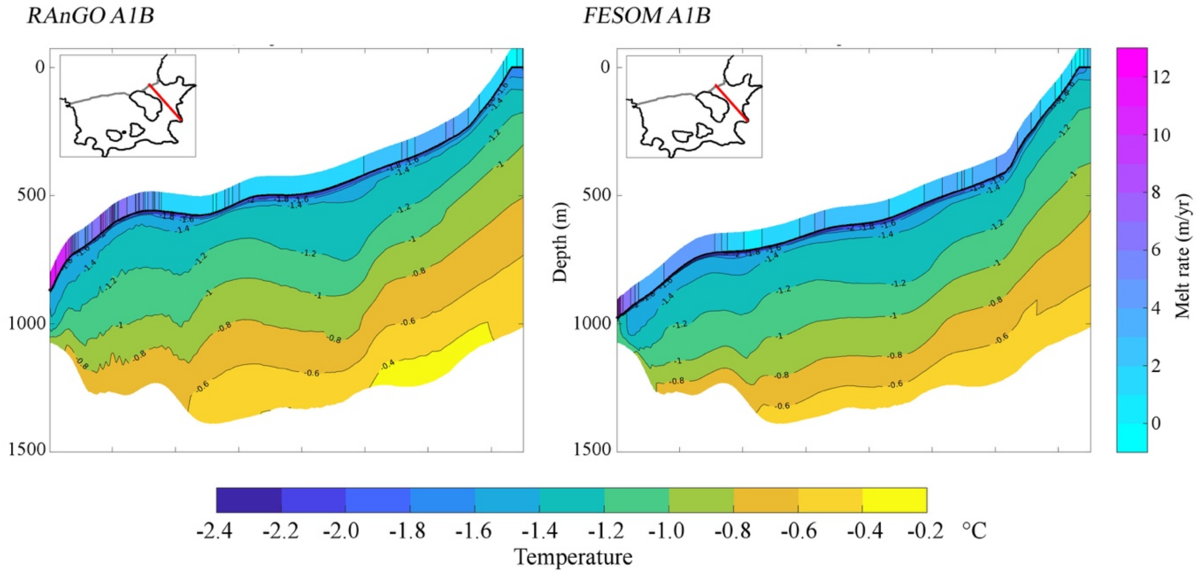

Fig. 2: Annual mean potential temperature sections for 2195 below Filchner–Ronne Ice Shelf in the coupled model RAnGO (left) and in FESOM with fixed ice shelf geometry (right). Colours on top of the ice-shelf base indicate annual mean basal melt rates. The red lines in the maps indicate the location of the section.

Outlook

Experience gained with and infrastructure developed for RAnGO will be utilized for the coupling between FESOM and the Ice Sheet System Model (ISSM) for the area of Northeast Greenland Ice Sheet and the 79°N-Glacier in HLRN. This effort is supported by funding from the *Helmholtz-Verbund Regionale Klimaänderungen* (REKLIM) and pursued in HLRN project hbk00038. For Antarctica we plan to implement a pan-Antarctic coupled model based on a combination of FESOM with the Parallel Ice Sheet Model (PISM).

Publications

1. van Caspel, Mathias, Hartmut H. Hellmer, and Mauricio M. Mata: *On the ventilation of Bransfield Strait deep basins.* Deep Sea Research Part II: Topical Studies in Oceanography, DOI: 10.1016/j.dsr2.2017.09.006, 2017.
2. Timmermann, R., and S. Goeller: *Response to Filchner–Ronne Ice Shelf cavity warming in a coupled ocean–ice sheet model – Part 1: The ocean perspective*. Ocean Science, 13, 765–776, 2017

Presentations

1. Ryan, S., Timmermann, R. and Schröder, M.: *Towards new eddy-resolving simulations with FESOM in the southwestern Weddell Sea,* FRISP - Forum for Reasearch into Ice Shelf Processes, Bergen, Norway, 19 June 2017 - 22 June 2017 (Poster)
2. Stulic, L., Timmermann, R., Zentek, R., Heinemann, G., Paul, S.: *Quantification of sea ice production at coastal polynyas in the southern Weddell Sea*, EGU General Assembly 2017 (Poster)

3. Stulic, L., Timmermann, R., Zentek, R., Heinemann, G., Paul, S.: *Quantification of sea ice production at coastal polynyas in the southern Weddell Sea*, NASA Jet Propulsion Laboratory (JPL), USA, June 2017 (Invited Talk)
4. Stulic, L., Timmermann, R., Zentek, R., Heinemann, G., Paul, S.: *Sensitivity of sea ice production in the southern Weddell Sea coastal polynyas to atmospheric forcing*, FISS/FISP Meeting, 18-19 October 2017, Bremen, Germany
5. Timmermann, R. and S. Goeller: *Response to a warming inflow in a coupled model of Filchner-Ronne Ice Shelf cavity*. Geophysical Research Abstracts Vol. 19, EGU2017-14061, 2017 (Poster)
6. Timmermann, R. and F. Schnaase: *Representation of shallow grounding zones in a sigma-coordinate ice shelf-ocean model*, FRISP - Forum for Reasearch into Ice Shelf Processes, Bergen, Norway, 19 June 2017 - 22 June 2017 (Poster)

5.15 ***hbk0038:*** Interaction between marine terminating glaciers and the ocean circulation in Northeast Greenland

HLRNProject ID:	hbk00038
Run time:	III/2014 – III/2018
Project Leader:	Prof. Dr. Torsten Kanzow
Project Scientists:	Dr. Ralph Timmermann and Dr. Claudia Wekerle
Affiliation:	Alfred Wegener Institute

Overview

The Greenland ice sheet has been subject to strong ice loss in the last decades. The flow of grounded ice towards the ocean accounts presently for a third to a quarter of global sea-level rise (Milne et al. 2009). The mass loss is particularly strong along the marine margins, where outlet glaciers drain the ice sheet (Rignot et al., 2012). The 79°N Glacier (79NG), located in Northeast Greenland, is one of Greenland's largest marine-terminating glaciers. Wilson et al. (2017) recently showed that the surface and basal melt flux exceeds the inflow of ice at the 79NG, indicating that the ice tongue is thinning. An important role is played by the ocean. A large fraction of Atlantic Water (AW), carried northward through the Fram Strait by the West Spitsbergen Current (WSC), recirculates and part of it spills over the Northeast Greenland continental shelf break, possibly mediated by eddies. It is then transported through a trough system on the continental shelf toward the glacier (Schaffer et al., 2017). Based on mooring measurements in the Fram Strait, Beszczynska-Möller et al. (2012) found that the amount of Atlantic Water carried by the WSC significantly increased during the last decades, which has implications for the stability of the 79NG.

In this project, we investigate the interaction of the marine terminating glaciers in Northeast Greenland with the ocean by applying the Finite Element Sea ice-ice shelf-Ocean Model FESOM. The high-resolution, eddy-resolving model configuration used in this project allows us to realistically resolve bathymetric features and eddy activity. Furthermore, we investigate the pathways of Greenland freshwater runoff. This is done by introducing tracers that track the freshwater pathways.

Results

(1) High resolution FESOM configuration

We use a high-resolution global FESOM configuration that was optimized for the Fram Strait (around 1 km mesh resolution in the wider Fram Strait; Wekerle et al., 2017) and further increased mesh resolution to around 800 m in the vicinity of the 79N Glacier. Bathymetry was taken from an updated version of RTopo-2 (Schaffer et al. 2016) which includes bathymetric measurements in front of the 79NG conducted during Polarstern expeditions in 2016 and 2017.The enhanced data set is referred to RTopo-2^{++}. As atmospheric forcing we use the JRA55 dataset (Kobayashi et al., 2015), which has a higher spatial resolution than the commonly used CORE2 dataset and is continuously updated. Around Greenland, we replace the JRA55 runoff with a dataset by Bamber et al. (2012), which provides more accurate freshwater fluxes.

A prerequisite for studying the interaction between the marine terminating glaciers and the regional ocean circulation is the correct representation of the AW layer. Figure 1 shows the simulated summer mean AW layer (defined by T>2°C), compared to measurements across the Northeast Greenland continental shelf break conducted on-board Polarstern during summer 2016. Note that measurements are very complicated in this region due to the presence of sea ice year-round. AW is present mainly in the southern trough that leads to the 79NG (Norske Trough), and not present in the northern trough (Westwind Trough). This is consistent with observations by Schaffer et al. (2017). Overall, the model corresponds well to the observations. Differences, e.g. at around 0°EW/80.5°N, can be due to a model bias, or due to different timescales of the simulated and observational data (long-term summer mean for the model vs. a synoptic snapshot for in-situ data).

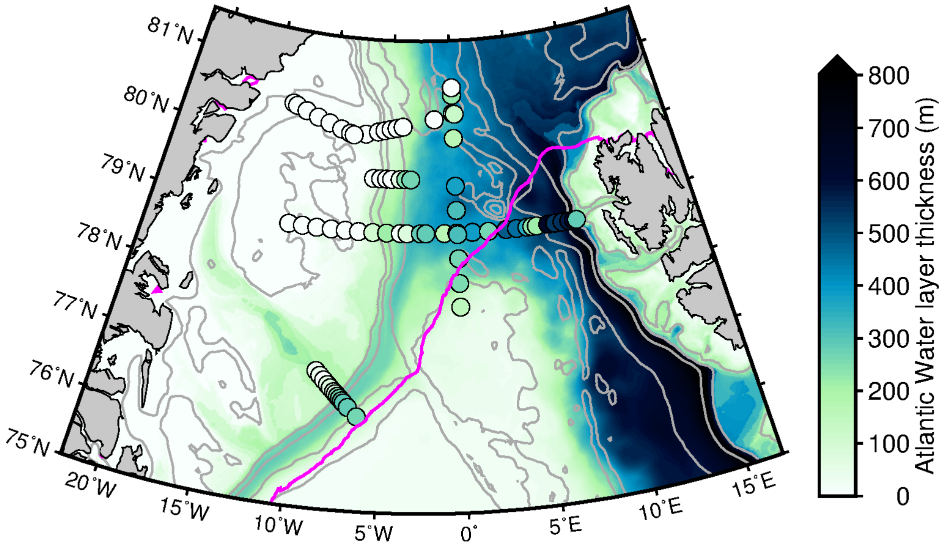

Fig. 1: Atlantic Water layer thickness simulated with FESOM (shading, long-term summer mean) and in-situ measurements conducted during a Polarstern expedition in summer 2016 (dots). Thin grey lines indicate the bathymetry from RTopo-2^{++}, and the magenta line shows the modelled summer ice edge (the western part of Fram Strait is ice-covered, while the eastern part is ice-free).

(2) Greenland runoff experiments

To study the pathways of Greenland freshwater runoff, we use a global FESOM configuration with relatively high mesh resolution around Greenland. The resolution in the Arctic and Atlantic Ocean is set to half the Rossby radius of deformation (see Sein et al., 2017, for a description of the mesh design). To obtain a mesh that still has a feasible number of nodes, the highest resolution is set to 6 km (which is still eddy-resolving in large parts of the North Atlantic). Greenland runoff by Bamber at al. (2012) is used, and its pathways are tracked with a passive tracer that is proportional to the runoff. Figure 2 shows the distribution of the tracer after one year of release. The East and West Greenland Current carries the runoff along the Greenland coast. It then spreads into the Subpolar Gyre region and further south into the western North

Atlantic.This experiment is part of a model inter-comparison study of the Greenland meltwater propagation in the framework of FAMOS (Forum for Arctic Modeling & Observational Synthesis).

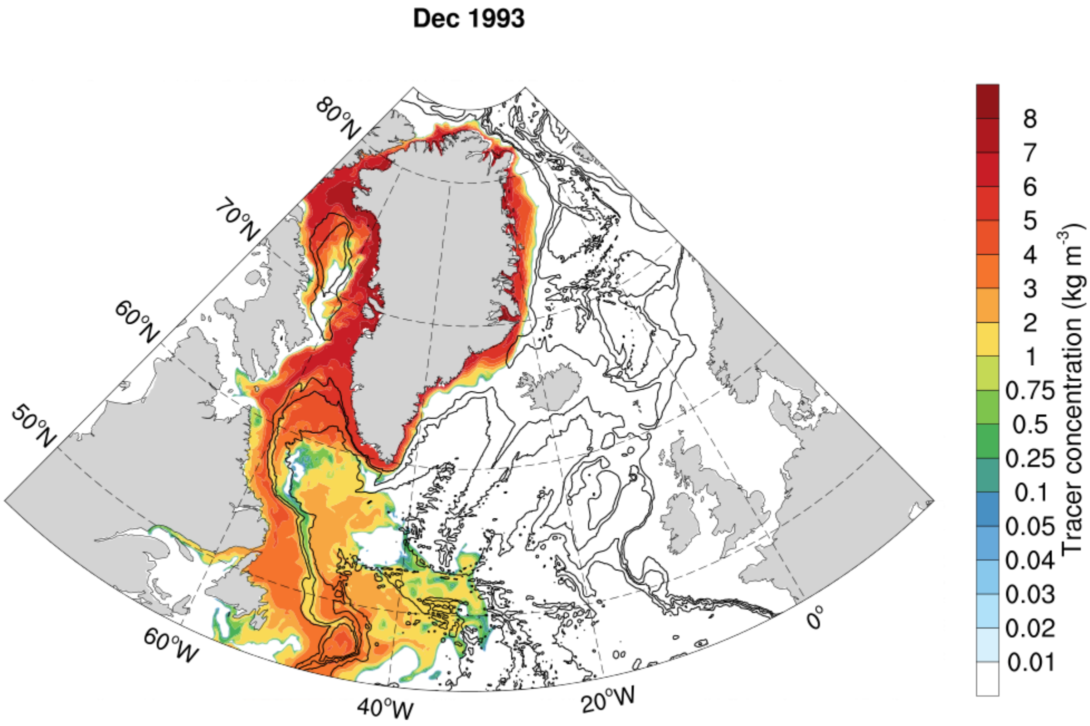
Dec 1993

Fig. 2: Tracer concentration in December 1993, after 1 year of release, in natural log-scale. The tracer tracks the Greenland runoff released around the Greenland coast. Black lines indicate the bathymetry from RTopo-2^{++}**.**

(3) Towards a coupled ice sheet-ocean model

Based on re-occurring uncertainties about the representation of isopycal mixing at the continental shelf break in the sigma-coordinate implementation of ice shelf – ocean interaction, we have started to explore possibilities to use z-coordinates not only for the deep ocean but also for ice shelf cavities. First results indicate an improved representation of cavity hydrography and circulation but leave open questions with regard to the distribution of basal melt rates. We will explore this field further in order to derive an optimal configuration for a coupled ice sheet – ice shelf – ocean model for the 79NG, the Northeast Greenland Ice Stream, and the regional and global ocean.

Outlook

As described above, first tests with a z-coordinate implementation of ice shelf cavities yield promising results with regard to cavity circulation and hydrography. In 2018, we plan to incorporate cavities into the high-resolution FESOM setup that has been the workhorse in this project. This configuration with be used to couple the ocean-sea ice model FESOM with the ice sheet model ISSM. This coupled model setup will allow us to study the interaction of the Greenland ice sheet with the regional ocean circulation and the relevant feedback processes in a consistent way.

Publications

Richter, M., von Appen, W.-J., and C. Wekerle: *On the Formation of the East Greenland Current in Fram Strait*, in prep.

References

Bamber, J., M. van den Broeke, J. Ettema, J. Lenaerts, and E. Rignot (2012), *Recent large increases in freshwater fuxes from greenland into the north atlantic*, Geophysical Research Letters, 39 (19).

Beszczynska-Möller, A., E. Fahrbach, U. Schauer, and E. Hansen (2012), *Variability in Atlantic water temperature and transport at the entrance to the Arctic Ocean, 1997-2010, ICES* J. Mar. Sci., 69, 852-863.

Dukhovskoy, D. S., P. G. Myers, G. Platov, M.-L. Timmermans, B. Curry, A. Proshutinsky, J. L. Bamber, E. Chassignet, X. Hu, C. M. Lee, and R. Somavilla (2016), *Greenland freshwater pathways in the sub-Arctic Seas from model experiments with passive tracers*, J. Geophys. Res. Oceans, 121 (1), 877-907.

Kobayashi, S., Y. Ota, Y. Harada, A. Ebita, M. Moriya, H. Onoda, L. Onogi, H. Kamahori, C. Kobayashi, H. Endo, K. Miyaoka, and K. Takahashi (2015), *The JRA-55 reanalysis: General specifications and basic characteristics*, J. Meteor. Soc. Japan, 95, 5-48.

Milne, G.A., Gehrels, W. R., Hughes, C.W. and Tamisiea, M. E. (2009), Identifying the causes of sea-level change. *Nature Geoscience*, 2, 471-478.

Schaffer, J., R. Timmermann, J. E. Arndt, S. S. Kristensen, C. Mayer, M. Morlighem, and D. Steinhage (2016), *A global high-resolution data set of ice sheet topography, cavity geometry and ocean bathymetry*, Earth System Science Data Discussions, 2016, 1-21.

Schaffer, J., W.-J. von Appen, P. A. Dodd, C. Hofstede, C. Mayer, L. de Steur, and T. Kanzow (2017), *Warm water pathways toward Nioghalvfjerdsfjorden Glacier, Northeast Greenland*, J. Geophys. Res. Oceans, 122 (5), 4004-4020.

Sein, D. V., Koldunov, N. V., Danilov, S., Wang, Q., Sidorenko, D., Fast, I., Jung, T. (2017), *Ocean modeling on amesh with resolution following thelocal Rossby radius.* Journal of Advances in Modeling Earth Systems, 9, 2601–2614.

Wekerle, C., Q. Wang, W.-J. von Appen, S. Danilov, V. Schourup-Kristensen, and T. Jung (2017), *Eddy-resolving simulation of the Atlantic Water circulation in the Fram Strait with focus on the seasonal cycle*, J. Geophys. Res. Oceans, 122, 8385–8405

Wilson, N., F. Straneo, and P. Heimbach (2017), *Satellite-derived submarine melt rates and mass balance (2011–2015) for Greenland's largest remaining ice tongues*, The Cryosphere, 11, 2773–2782.

5.16 ***hbk00042:*** **Climatic evolution in the marginal seas of the Northwest Pacific Ocean since the last glacial period until present day: changes in the formation of North Pacific Intermediate Water formation and their implications on the Pacific realm**

HLRN Project ID: hbk00042
Run time: I/2015 – IV/2017
Project Leader: Prof. G. Lohmann
Project Scientists: Dr. P. Scholz, Dr. X. Gong

Affiliation: Alfred Wegener Institute Helmholtz Center for Polar and Marine Research

Overview

The aim of this project is to simulate the variability of the sea ice cover, general ocean circulation and hydrology of the marginal seas in the Northwest Pacific Ocean as well as the Arctic Ocean on different time-slices since the last glacial period up to present day (e.g. last glacial maximum (LGM, 21000 years ago), mid (6000 years ago) Holocene, pre-industrial as well as present day). A particular focus will be on the Sea of Okhotsk, which has nowadays a significant role in the climate system of the Northwest Pacific by influencing the atmospheric and oceanic circulation as well as the hydrology of the Pacific water masses. In the Sea of Okhotsk, the so called Sea of Okhotsk Intermediate Water (SOIW) is formed, which in turn contributes to the vertical ventilation in the North Pacific and to the mid-depth water masses of the North Pacific Intermediate Water (NPIW). NPIW is one of the key elements for the nutrient and oxygen supply of the low latitude Pacific Ocean realm. As such the main question of this project is: How the role of the Sea of Okhotsk and the other marginal Seas (e.g. Bering Sea) as a source for NPIW has changed during the different climatological time-slices since the last glacial period? Beyond the regional focus on the marginal seas of the Northwest Pacific, this project should also clarify what are the large scale implications and teleconnections of the changes in NPIW. To find a compromise between a global coverage and a regional highly increased resolution, which is necessary to adequately reproduce the deep and intermediate water formation, at relatively moderate computational costs, we will use in this project the Finite-Element Sea-Ice Ocean Model (FESOM).

Previous simulation of the present-day time-slice revealed significant deficiencies in the vertical stratification of the marginal seas of the Northwest Pacific Ocean when compared with observational data. The comparison showed a tremendous deviation between the modeled and observed temperature and salinity over depth and time in the southern Sea of Okhotsk, especially in depths below 200 m. There, the modeled temperature and salinity features a constant warming and excess in salinity over the entire considered period of around 1.5◦ C to 2.0◦C and ∼ 0.5 psu, respectively compared to the observed values. The magnitude of the modeled heat and salinity excess in the Sea of Okhotsk linked to a systematic problem in the model. This could be connected to the North Pacific gyre system, consisting of northern subpolar gyre and northern subtropical gyre, which is responsible for transporting and distributing massive amounts of heat and salt into high latitudes. We could trace back this warming anomaly in the model throughout the entire northern branch of the subpolar pacific gyre and found its possible origin in problems with the Kuroshio Extension Current (KEC) in the model (not shown). It revealed that the detachment and position of the KEC is shifted by around 2° to 3° degree to the north when compared to reality. Also the modeled pathway of the KEC is tilted slightly to the north, although observational data let suggest thats its slightly tilted to the south, as well as the modeled strength of the KEC is overestimated. Due to this, to much warm waters from the subtropical pacific gyre could reach to the north and enter the branch of the subpolar pacific gyre and causes the warming anomaly in the Sea of Okhotsk. The deficiencies in the KEC and the associated warming anomaly was consistent through all spinup cycles that was carried out and was thus not an issue that could have been solved by a further improvement due to more spinup cycles. The factor of the external atmospheric forcing was already excluded by earlier tests with additional atmospheric forcing data e.g. ERA eo/interim and NCEP. This caused us to search for other possibilities to improve our model results (e.g. mesh improvements, local corrections of the forcing, improvements in the parameterization of the model). In the previous year we focused on improving the mesh resolution in critical areas, like the area of the KEC and the region of the Northern Equatorial Current. These changes in our model configuration led to improvements in the stratification and ventilation of the sea of Okhotsk but not to the extent we expected. A further in depth analysis of the boundary currents of North Pacific subpolar gyre revealed, that the Alaskan Stream in out model is still around 2°C too warm and too saline. The fingerprint of this bias is than transferred in our model onto the Sea of Okhotsk and Bering Sea. In early 2017 we tested further hypothesis to improve the vertical ventilation and hydrography in the marginal seas of the Northwest Pacific.

1. Correcting the surface wind forcing fields with CCMP observational based data.

The comparison of our modeled surface ocean velocity (Fig. 1a) with observational derived OSCAR surface ocean velocities (Fig. 1b) has revealed that the separation point of the KEC in the model and in the observations are very similar. Also the meandering of the KEC could be well reproduced in the model. However, there is a big difference in the modeled path of the KEC compared to the observational derived surface current velocities. The modeled path of the KEC is slightly inclined to the north by about 0.08 °, whereas the path of the KEC derived from observations is tilted by -0.11 ° to the south. This leads to the fact that in our model more heat and salt are transported to the north than would be expected from the observational surface current data.

The pathway of the KEC on the surface is largely determined by the prevailing wind systems, which in our model configuration is prescribed by the COREv2 10 m surface winds. A further comparison of COREv2 Reanalysis surface winds with purely observational derived Cross-Calibrated Multi-Platform Ocean Surface Wind Vectors version 2 (CCMPv2) has revealed that there are substantial deviations between both data sets in the area of the KEC, which could explain a northward directed KEC pathway when using COREv2 surface winds as forcing. To test this hypothesis we corrected the COREv2 10 m surface winds with the anomaly between their monthly climatology and the monthly climatology calculated from the CCMPv2 10 m surface winds and try to force the model with the corrected COREv2-CCMP 10 m surface winds. Fig. 2 shows the modeled ocean current with original COREv2 a) and corrected COREv2-CCMP b) surface winds. The model simulation with corrected COREv2-CCMP surface wind indicated a clear improvement in the path of the Kuroshio current. The improvement that has now been achieved in the Kuroshio Stream path is very similar to the pure observed ocean surface currents (OSCAR) (see Fig. 1b). But even this correction led to only a marginal improvement in the temperature and salinity of the Alaska stream as well as in the intermediate layers of the Bering Sea and the Sea of Okhotsk.

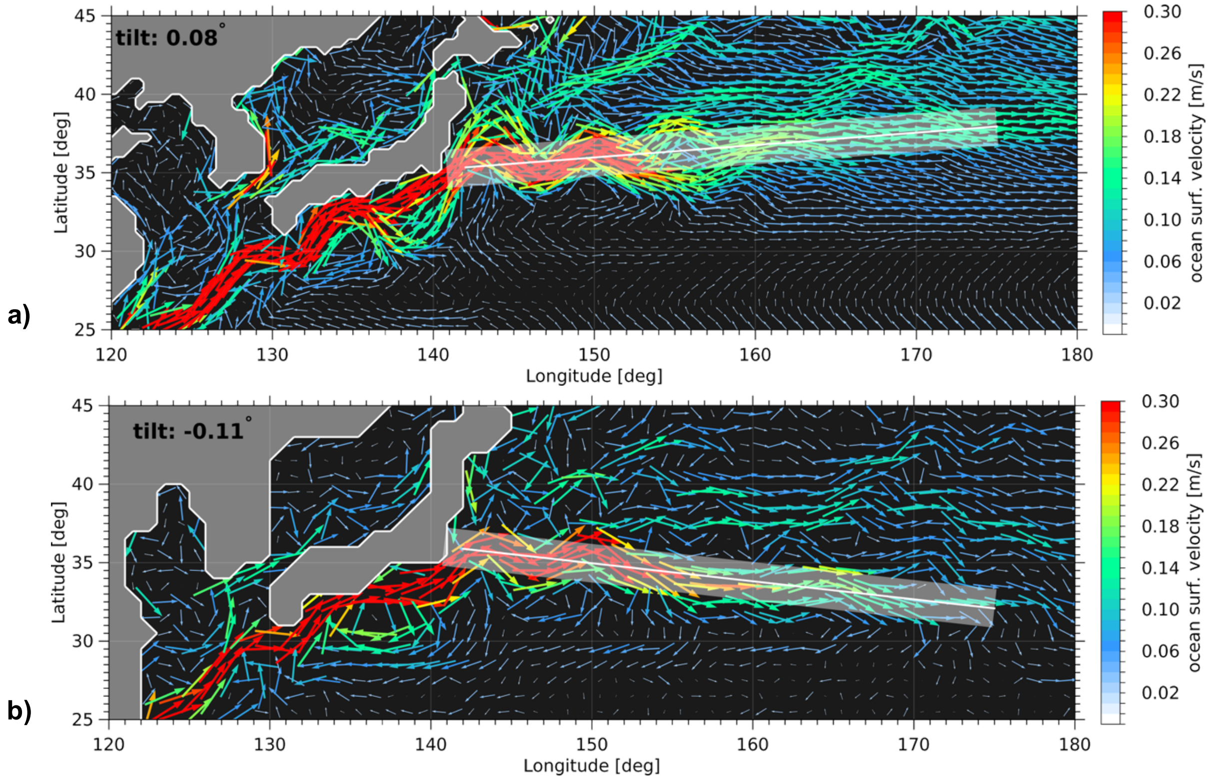

Figure 1: Modelled (a) and from observational OSCAR data derived (b, Ocean Surface Current Analysis Real-time) mean ocean surface velocity in the area of the KEC.

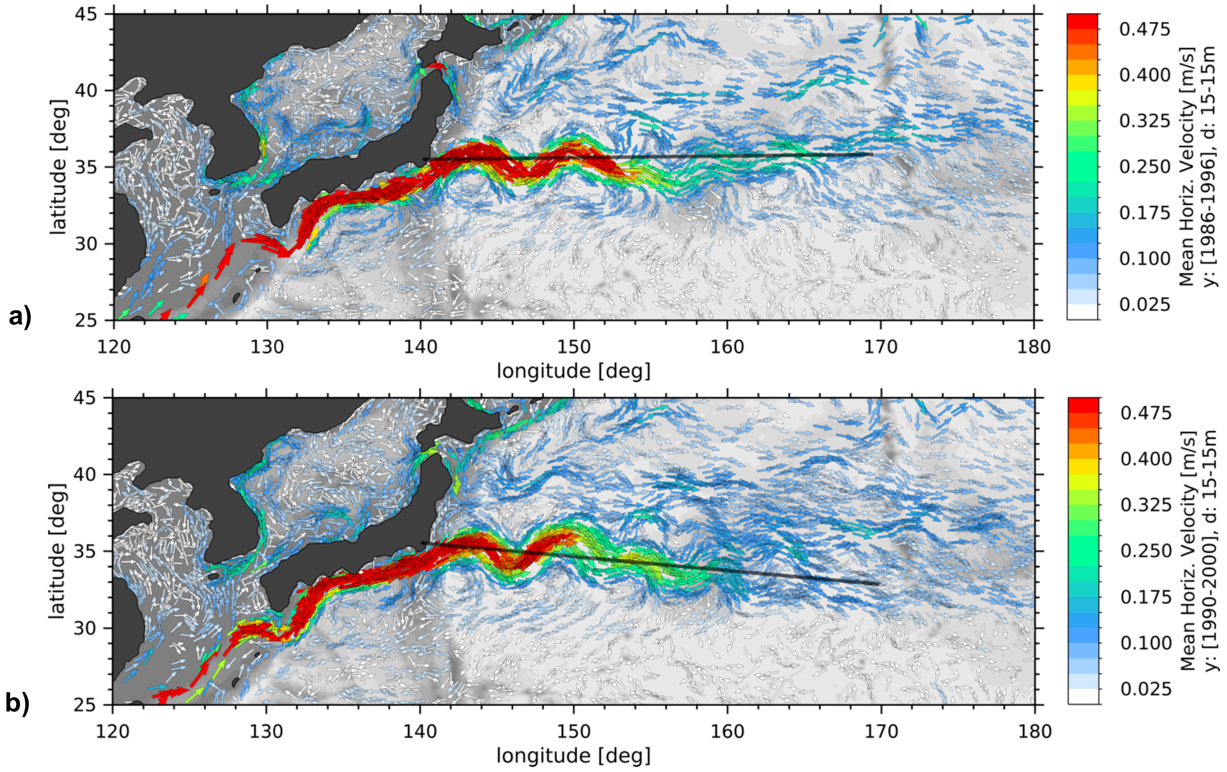

Figure 2: Modelled ocean current velocity at 15m depth averaged over 10 years, in the area of the Kuroshio Currents, forced with the original (a) and with the corrected COREv2-CCMP

2. Reducing the general advection of temperature and salt

In middle of 2017 we applied further comparisons between modeled and observed sea surface currents data, which continued to show strong deviations in the strength of the boundary currents. The magnitude of the modeled flow velocities in the boundary currents responsible for most of the heat and salt transport is by a factor of 1.4 to 1.8 enhanced when compared to the observed magnitude of the flow velocities (not shown). This suggests that the model in the Pacific may overestimate the general advection of heat and salt to the north by a similar factor, thereby causing increased heat and salinity in the Alaska Stream and in the intermediate depths of the Bering Sea and the Okhotsk Sea. To test this hypothesis, various test scenarios were carried out to reduce the flow velocities in the boundary flows. In test scenario 1, we attempted to reduce the input of momentum into the ocean by reducing the wind drag coefficient, thereby reducing flow velocities. However, this approach had in the model undesirable feedback effect which led to further warming of the subpolar Pacific marginal seas and was therefore discarded. In test scenario 2, attempts were made to reduce the flow rate by increasing the overall background viscosity in the model. But again, feedback effects led to a deterioration of the model state.

3. Improving Vertical Mixing

In addition to the two aforementioned test scenarios, two further test simulations were carried out in the second half of 2017 in order to test the effect of an improved penetration of short-wave radiation into the ocean, and to test the effect of an additional module for non-breaking surface waves. Both test scenarios serve to further improve the vertical mixing in the ocean and thus to further reduce the deviation between modeled and observed hydrography. The non-breaking surface wave module was developed by scientists of the First Institute of Oceanography (FIO) in China and has already been implemented in FESOM in a simplified form in another project. Both the improved penetration of the short-wave radiation and the module for non-breaking surface waves led to slight improvements in the modeled hydrograpy in the Sea of Okhotsk.

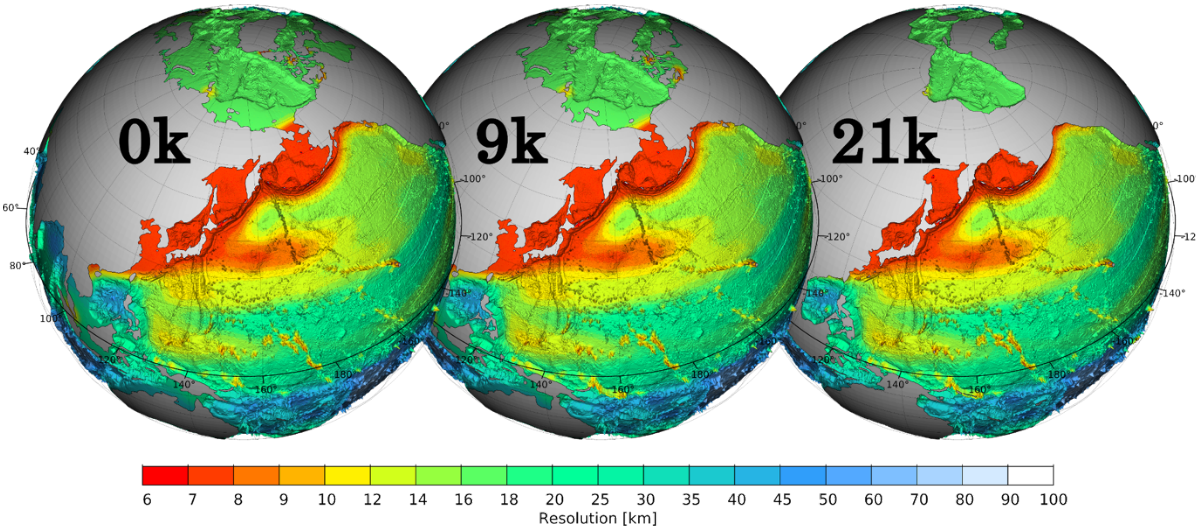

Figure 3: Mesh resolution of the northwestern Pacific FESOM configuration for time-slice experiments of today's climate (0k), the early Holocene (9k), and the Last Glacial Maximum (21k). The minimum mesh resolution in the Sea of Okhotsk, in the Sea of Japan and in the Bering Sea is about 6 to 8 km.

4. Final model configuration:

Towards the end of 2017, after completing all hypothesis test simulations, a model configuration was composed, based on the experience gained so far, with improved resolution, corrected surface forcing and an improved parameterization of vertical mixing. This configuration provides us in moment with the for us best achievable hydrography in the marginal seas of the Northwest Pacific Oceans. Although it should be mentioned that the found model biases could not be fully reduced. The mesh configuration for the time slice experiments of today's climate, the early Holocene, as well as for the last glacial maximum were generated together using all knowledge gained (see Fig. 3). Special emphasis was placed on the fact that the different mesh configurations have in the same regions the same mesh resolution. The stability of all three lattice configurations was first tested by using present day COREv2 surface forcing.

5.17 ***hbk00044:*** Exploring pathways of Atlantic Water into the Arctic Ocean: high resolution ocean-sea ice and biogeochemical simulations

HLRNProject ID:	hbk00044
Run time:	III/2017 – II/2018
Project Leader:	Prof. Dr.Thomas Jung[1,2]
Project Scientists:	Dr. Claudia Wekerle[2], Dr. Vibe Schourup-Kristensen[2], Dr. Qiang Wang[2], Dr. Sergey Danilov[2,3]
Affiliation:	[1]University of Bremen, [2]Alfred Wegener Institute for Polar and Marine Research, [3]Jacobs University Bremen

Overview

The Arctic Ocean and Nordic Seas are currently subject to strong changes. The sea ice cover is decreasing (Comiso et al., 2008) and the ice is becoming younger and thinner, with implications for ocean circulation and mixing as well as biological production in the water as well as in the sea ice (e.g. Arrigo and van Dijken, 2015; Assmy and et al., 2017). Furthermore, the changes in ice cover, water temperatures and phytoplankton productivity are thought to change the air-ocean carbon fluxes; though we currently do not know how much or in which direction. One open question is the role of eddies, which are likely to play an important role in these processes as they modulate the vertical transport of matter. Here, we have used the unique multi-resolution capabilities of the ocean general circulation model FESOM alone and coupled to the biogeochemical model REcoM2 to look into eddy dynamcis as well as the changing carbon cycle in the Arctic Ocean and the role of sea ice algae.

Results

1. High-resolution ocean-sea ice simulations with focus on the Fram Strait

The advantage of the multi-resolution model FESOM is its ability to increase mesh resolution in areas of interest. In this project, we increased resolution in the wider Fram Strait to 1 km. Compared to the Rossby radius of deformation, an indication of the size of eddies, this simulation can be considered as ‘eddy resolving’. A comparison with observational data from along-term mooring array located in the central Fram Strait revealed that the model preforms well in simulating hydrography, circulation and eddy kinetic energy (Wekerle et al., 2017). Furthermore, a comparison of the model with another eddy-resolving model, ROMS, showed that both models mostly agree on eddy properties and eddy pathways (Wekerle et al., in prep.).

2. Application of the model: Catchment area of sediment traps deployed in the Fram Strait

How can model simulations complement and help to interprete measurements carried out in the Fram Strait? Since years, biologists at the AWI measureparticle fluxes with moored sediment traps in the long-term observatory Hausgarten, located in the Fram Strait (e.g.

Bauerfeind et al. 2009). These measurements help to reveal changes in ecosystem structure such as carbon fluxes over a longer time period.

So far it was unclear from where the trapped particles originate. To determine their origin, we used the daily model output from our high-resolution FESOM simulation (Wekerle et al., 2017) and calculated backward particle trajectories. Pathways of 10 particles released at mooring HG-N in 2300 m depth in the first days of January 2009, sinking with a speed of 20 m/d, are shown in Figure 1. Most particles originate from south of the mooring position, indicating that they are carried by the northward flowing West Spitsbergen Current (Wekerle et al. in prep.).

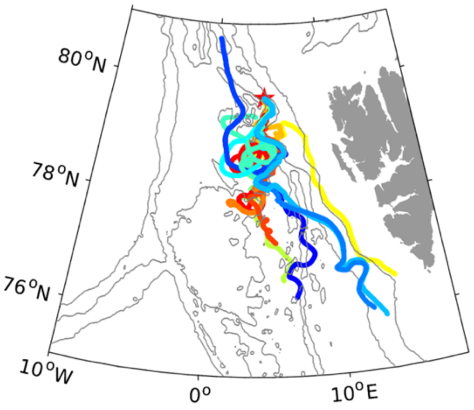

Figure 1: Backward trajectories released at mooring HG-Nin 2300 m depth between 1-10 Jan 2009, indicated by different colors. Particles sink with a speed of 20 m/day. The red star indicates the location of the mooring. Gray contours show the bathymetry at 1,000 m intervals.

3. Coupled ocean-sea ice-biogeochemical simulations; the carbon cycle and ice algae

Despite of the relatively small size of the Arctic Ocean, between 5 and 14% of the global oceanic carbon uptake is thought to occur in the area. Using our Arctic mesh, FESOM-REcoM2 has therefore been prepared to do carbon cycle runs, which require a relatively long spin-up to get the surface carbon into equilibrium. We have assessed the carbon cycle on the global scale with a special focus on the Arctic Ocean.

Results show that our model run is in good agreement with both estimates of the global carbon flux based on measurements as well as large scale modelling (Figure 2), the same is the case of the Southern Ocean and Arctic Ocean carbon uptake. The Arctic takes up 10% of the global carbon in our run, with most of the uptake occurring in the Nordic Seas and the Barents Sea. Globally, the modelled carbon uptake has increased significantly, while it has stagnated in recent years in the Arctic Ocean. This stagnation can be attributed to a warming of the Nordic Seas and the Barents Sea, leading to less uptake. This is, however, partly counteracted by an increasing uptake on the increasingly more ice free Russian shelves.

To investigate the ecosystem changes in an Arctic in which the sea ice is becoming thinner and more fragmented, it is necessary to look into sea ice algae in addition to the oceanic algae. Building on work from AWI (Castellani et al., 2017), we have therefore coupled FESOM with a sea ice algae model. To test the impact of the mesh resolution on sea ice algae productivity, we compared runs carried out with our 4.5km and 20km Arctic mesh resolution. Results showed that ice algae productivity was higher in the high resolution mesh, especially in areas where this model run created heterogeneity in the sea ice that is not possible in coarser model runs. Additionally, the onset of the bloom occurred earlier in the high resolution run.

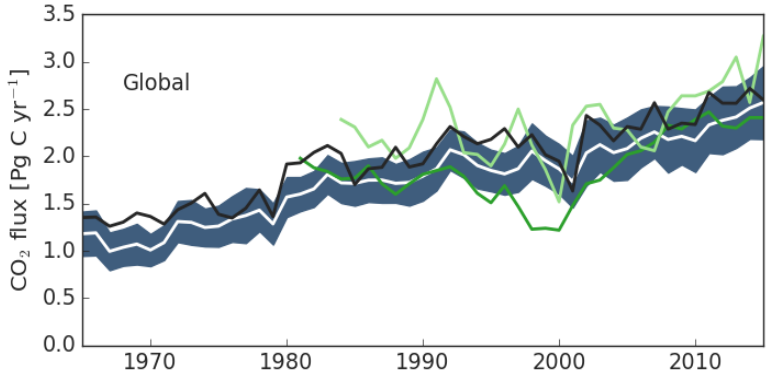

Figure 2: Global oceanic uptake of carbon for the last cycle of the run. Green lines are uptake based on measurements, white line with blue standard deviation is the average of the models from the Global Carbon Project and the black line is the carbon uptake in FESOM-REcoM2.

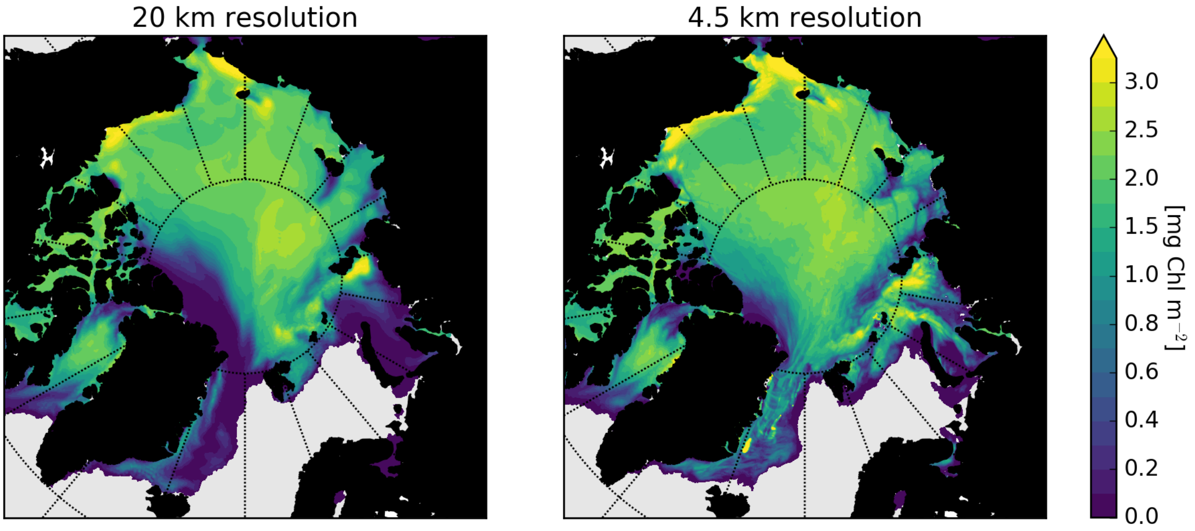

Figure 3: May sea ice algae concentration in FESOM. Left: Mesh with an Arctic resolution of 20 km. Right: Mesh with an Arctic resolution of 4.5km.

Outlook

We are now at a stage where FESOM runs in setups with the biogeochemical model REcoM2 and with a sea-ice algae model. Using FESOM-REcoM2 it is possible to make large scale runs looking at the global carbon cycle, and further coupling this model to an atmospheric model would be an important step towards a full climate model setup.The setup with the sea ice algae model works well, but still needs testing and further comparison with *in-situ* measurements.

The comparison with observational data showed that eddy-resolving simulations are needed to realistically simulate the Fram Strait ocean dynamics. In the future, we plan to carry out coupled FESOM-REcoM2 simulations with this high-resolution mesh.

Publications

1. Wekerle, C., Q. Wang, W.-J. von Appen, S. Danilov, V. Schourup-Kristensen, and T. Jung (2017), *Eddy-resolving simulation of the Atlantic Water circulation in the Fram Strait with focus on the seasonal cycle*, J. Geophys. Res. Oceans, 122, 8385–8405.

2. Schourup-Kristensen, V., Wekerle, C., Wolf-Gladrow, D. A., and C. Völker: *Arctic Ocean biogeochemistry in the high resolution FESOM 1.4-REcoM2 model*, under review, Progress in Oceanography.

Publications (in prep.)

1. Wekerle, C., T.Krumpen, T.Dinter, W.-J. von Appen, and I. Salter: *Catchment area of sediment traps in the Fram Strait*, in prep.
2. Schourup-Kristensen, V., Wekerle, C., Völker, C., Wolf-Gladrow, D. A. and Hauck, J: *The Arctic carbon cycle in the multi resolution model FESOM-REcoM2*, in prep.
3. Fadeev, E., Salter, I., Bienhold, C., Schourup-Kristensen, V., Metfies, K., Engel, A., Piontek, J., Nöthig, E.-M. andBoetius, A.: *Bacterial assemblages of surface mixed layer across Fram Strait during sea-ice melting season*, in prep.
4. Wekerle, C., Hattermann, T., Crews, L., Wang, Q.,Danilov, S. and Jung, T.: *Eddy properties and dynamics in the Fram Strait*, in prep.

Presentations

1. Wekerle, C., Wang, Q., Danilov, S., von Appen, W. J., Schourup-Kristensen, V. and Jung, T., *Eddy-resolving simulation of the Atlantic Water recirculation in the Fram Strait*, Talk, DRAKKAR 2017 Annual Workshop, Grenoble, France, 16-18 January 2017.
2. Wekerle, C., Wang, Q., Danilov, S., von Appen, W. J., Schourup-Kristensen, V. and Jung, T., *Eddy-resolving simulation of the Atlantic Water circulation in the Fram Strait*, Invited talk, Youmares, Kiel, 13-14 September 2017.
3. Wekerle, C., Hattermann, T., Wang, Q., Danilov, S., von Appen, W.-J., and Jung, T., *Eddy dynamics and properties in the Fram Strait*, Poster, Forum for Arctic Modeling& Observational Synthesis, Woods Hole, USA, 24-27 October 2017.
4. Schourup-Kristensen, V., Wang, Q. and Castellani, G.: *Arctic sea-ice algae and model resolution*, Poster, Forum forArctic Modeling &Observational Synthesis, Woods Hole, USA, 24-27 October 2017.
5. Schourup-Kristensen, V., Wekerle, C., Wolf-Gladrow, D. A., and C. Völker: *Strong eddy control oft he post-bloom nutrient supply to the surface water of the Norwegian Sea*, Ocean Sciences Meeting, Portland, OR, 12-16 February 2018.

References

Arrigo, K. R., and G. L. van Dijken (2015), Continued increases in Arctic Ocean primary production, Progress in Oceanography, 136, 60–70.

Assmy, P., and et al. (2017), Leads in Arctic pack ice enable early phytoplankton blooms below snow-covered sea ice, Scientific Reports, pp. 1–9.

Bauerfeind, E., Nöthig, E.-M., Beszczynska-Möller, A., Fahl, K., Kaleschke, L., Kreker, K., Wegner, J. (2009). Particle sedimentation patternsin the eastern Fram Strait during 2000–2005: Results from the Arctic long-term observatory HAUSGARTEN, Deep Sea Research, Part I, 56 (9), 1471–1487.

Castellani, G., Losch, M., Lange, B. and Flores, H. (2017), Modeling Arctic sea-ice algae: Physical drivers of spatial distribution and algae phenology, J. Geophys. Res.

Comiso, J., C. Parkinson, R. Gersten, and L. Stock (2008), Accelerated decline in the Arctic sea ice cover, Geophys. Res. Lett., 35.

5.18 ***hbk00045:*** Determination of vertically resolved trends in the stratospheric ozone from SCIAMACHY limb measurements

HLRNProject ID:	hbk00045
Run time:	IV/2015 – II/2018
Project Leader:	Dr. Alexei Rozanov
ProjectScientists:	C. Arosio, N. Rahpoe
Affiliation:	Institute of Environmental Physics, University of Bremen

Overview

Importance of the stratospheric ozone layer has been widely discussed by the scientific community. Playing a key role in the radiative budget of the Earth's atmosphere the stratospheric ozone also protects the biosphere from the harmful UV radiation and is closely related to stratospheric circulation and meteorology. After anthropogenic emissions of several strong ozone depleting substances have been ruled out by the Montreal Protocol and its amendments, the severe ozone decline discovered in early eighties of the last century (widely known as Antarctic ozone holes) began to slow down and even some indications of the ozone recovery have been inferred from observations. In the recent time the vertical distribution of stratospheric ozone trends has been moved into the focus. Analyzing vertically resolved time series of tropical ozone, scientists agree in their conclusions that a significant ozone recovery is seen in the upper stratosphere (above 30-35 km) outside the tropical region and in the lower tropical stratosphere. On the contrary, significant ozone depletion is observed in tropics at altitudes about 35 km. A discussion if the latter phenomenon has purely dynamic or also chemical reasons is currently ongoing in the scientific community. Being vertically integrated these opposite trends result in a slightly positive contribution which explains the signatures of a recovery seen in the observations of ozone total column.

In the framework of this project global vertical distributions of ozone obtained from measurements of the scattered solar light in the limb viewing geometry from the space-borne SCIAMACHY (SCanning Imaging Absorption spectroMeter for Atmospheric CHartograohY) instrument onboard the European satellite Envisat are analyzed. Previous activities performed within this project resulted in a significant improvement of the retrieval algorithm by fixing identified data quality issues. Processing of the global data set over the entire operation time of the SCIAMACHY instrument is currently completed to a large extent. The obtained results were used in the recently published trend studies [Sofieva et al., 2017; Steinbrecht et al., 2017]. The final goal of the project is to improve the general knowledge on stratospheric ozone behavior needed for a better understanding of chemical and dynamic processes in the Earth's atmosphere.

Results

One of the most crucial issues related to obtaining reliable estimations for long-term variations of the atmospheric speciesis the stability of the data record. To assess the stability of the new SCIAMACHY limb V3.5 data set, measurements from Aura-MLS instrument of NASA are used as the reference. This choice is justified by the fact that no drift issues were reported in MLS validation so far and, thus, this instrument is considered to be stable and its data can be used to assess the stability of new data sets. As significant drifts with respect to the MLS data record were identified in the previous SCIAMACHY limb ozone product, we illustrate the achieved improvementsby comparing both the new (V3.5) and old (V2.9) data sets to the results from

MLS. An example comparison for the tropical middle stratosphere is presented in Fig. 1. This region has been selected because of the unexpected negative ozone trends identified before. The left panel of the figure shows time series of the ozone monthly zonal mean number densities obtained from MLS (blue) and SCIAMACHY (red) measurements. Here, only the SCIAMACHY data set V3.5 is shown. The right panel presents the relative differences between the SCIAMACHY and MLS data for the new (blue) and old (cyan) SCIAMACHY retrieval versions. A multivariate linear regression analysis of the obtained differences detects a drift of about -5% per decade with respect to MLS data for the old retrieval version and about -0.7% per decade for the new one. With typical uncertainties of ozone trends of 1 - 3% per decade the drift detected in the new data version is not significant. A similar improvement in the data record quality with respect to the drift is observed in most of the relevant latitude and altitude ranges (not shown here).

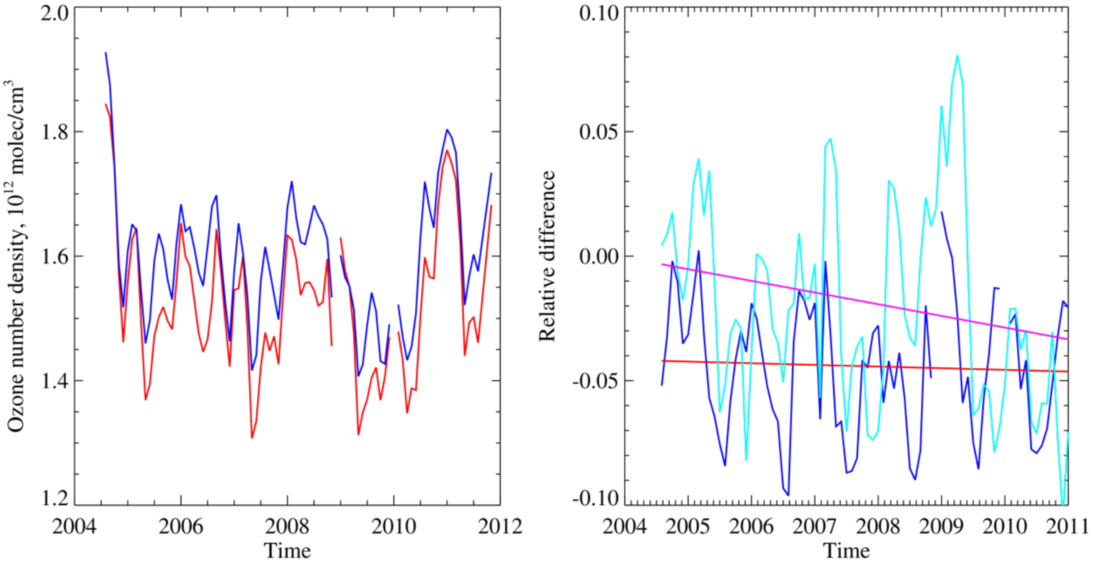

Fig. 4: Comparison of the ozone tropical (5°S - 5°N) zonal monthly mean time series at 35 km from coincident SCIAMACHY and MLS measurements. Left: tropical zonal monthly mean time series from MLS (blue) and SCIAMACHY V3.5 (red) data. Right: relative difference between SCIAMACHY V3.5 and MLS (blue) as well as SCIAMACHY V2.9 (cyan) and MLS data. Red and magenta lines show the linear fit terms for data sets V3.5 and V2.9, respectively.

Although not yet fully completed, the data set from the retrieval version 3.5 created in the framework of this project has been used tore-evaluate the ozone trends from SCIAMACHY limb measurements and compare them to the previous results. The same multivariate linear regression approach including seasonal terms (6 and 12 months sine and cosine functions) as well as proxies for QBO (Quasi-Biennial Oscillation) and ENSO (El Niño–Southern Oscillation) was used to obtain the trends from both new and old SCIAMACHY ozone data records. The resulting long-term variations in the stratospheric ozone are shown in Fig. 2 (please note different color scales). While general signatures remain the same (e.g., negative trends around 33 km altitude, hemispherical asymmetry), the overall magnitude of the detected trends is substantially reduced. The negative peak in the tropical middle stratosphere is now at -15% per decade (instead of -26% as calculated from V2.9 data record) which agrees much better with the results from other instruments.

The new SCIAMACHY limb V3.5 ozone data set was used in the framework of the ESA Ozone-CCI project(http://www.esa-ozone-cci.org/) to obtain a merged datarecord from three European (GOMOS, MIPAS, SCIAMACHY) and three Canadian (ACE-FTS, OSIRAS, SMR) satellite instruments. This merged data set, in combination with historical SAGE II record and the most resent OMPS data, was used to estimate the trends in the stratospheric ozone for longer time periods from 1997 to 2016 by Sofieva et al. (2017) and from 2000 to 2016 by Steinbrecht et al. (2017). Although the results presented in these papers are not directly comparable to those shown in Fig. 2 because of different time periods, the qualitative behavior observed in the middle stratosphere is very similar: a clear ozone recovery is seen in the extra-tropical regions above about 35 km, while a tendency to the ozone loss remains observed around 35 km in tropics.

Besides the trend studies, the new SCIAMACHY limb ozone data set was used to investigate the behavior of the tropospheric ozone columns over the Arabian Sea area by Jia et al. (2017).

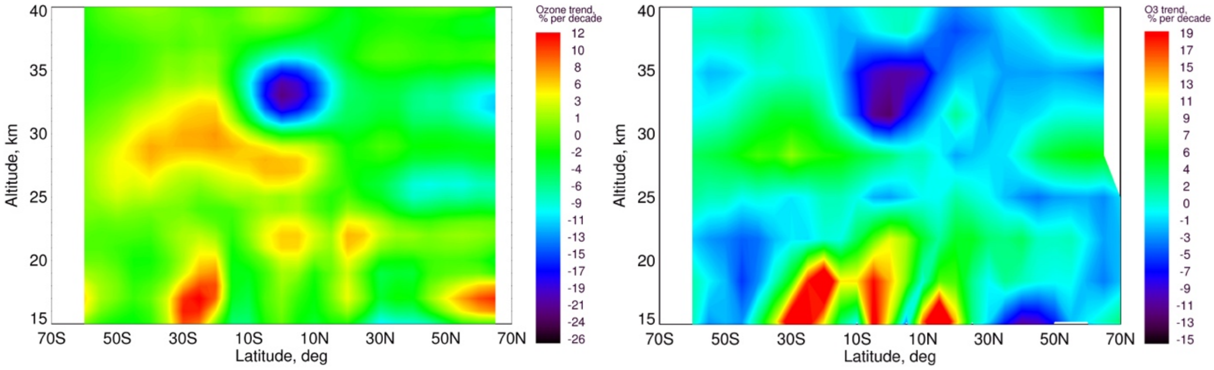

Fig. 5: Ozone trends obtained from SCIAMACHY limb data. Left: previousretrieval version, V2.9. Right: new retrieval version, V3.5.

Outlook

As it was discovered during the reporting period, the current retrieval (V3.5) fails to run under the polar mesospheric clouds (PSC) conditions which usually take place in the summer at high latitudes. This affects the data at high latitudes (about 2/5 of the entire geographical coverage of SCIAMACHY) for about 4 months per year (around the summer time). To fix this problem an additional correction for PSCs is currently under implementation.

Furthermore, an influence of the stratospheric aerosol on the observed ozone trends and a misinterpretation of the increased stratospheric aerosols as clouds and subsequent removal of the corresponding observations remain issues. The work on these issues is ongoing.

Publications

1. Jia, J., Ladstätter-Weißenmayer, A., Hou, X., Rozanov, A., and Burrows, J. P.: Tropospheric ozone maxima observed over the Arabian Sea during the pre-monsoon, Atmos. Chem. Phys., 17, 4915-4930, doi:10.5194/acp-17-4915-2017, 2017.
2. Sofieva, V. F., Kyrölä, E., Laine, M., Tamminen, J., Degenstein, D., Bourassa, A., Roth, C., Zawada, D., Weber, M., Rozanov, A., Rahpoe, N., Stiller, G., Laeng, A., von Clarmann, T., Walker, K. A., Sheese, P., Hubert, D., van Roozendael, M., Zehner, C., Damadeo, R., Zawodny, J., Kramarova, N., and Bhartia, P. K.: Merged SAGE II, Ozone_cci and OMPS ozone profile dataset and evaluation of ozone trends in the stratosphere, Atmos. Chem. Phys., 17, 12533-12552, https://doi.org/10.5194/acp-17-12533-2017, 2017.
3. Steinbrecht, W., Froidevaux, L., Fuller, R., Wang, R., Anderson, J., Roth, C., Bourassa, A., Degenstein, D., Damadeo, R., Zawodny, J., Frith, S., McPeters, R., Bhartia, P., Wild, J., Long, C., Davis, S., Rosenlof, K., Sofieva, V., Walker, K., Rahpoe, N., Rozanov, A.,

Weber, M., Laeng, A., von Clarmann, T., Stiller, G., Kramarova, N., Godin-Beekmann, S., Leblanc, T., Querel, R., Swart, D., Boyd, I., Hocke, K., Kämpfer, N., MaillardBarras, E., Moreira, L., Nedoluha, G., Vigouroux, C., Blumenstock, T., Schneider, M., García, O., Jones, N., Mahieu, E., Smale, D., Kotkamp, M., Robinson, J., Petropavlovskikh, I., Harris, N., Hassler, B., Hubert, D., and Tummon, F.: An update on ozone profile trends for the period 2000 to 2016, Atmos. Chem. Phys., 17, 10675-10690, https://doi.org/10.5194/acp-17-10675-2017, 2017.

Presentations

1. A. Rozanov, C. Arosio, N. Rahpoe, K.-U. Eichmann, and J.P. Burrows: Improved ozone retrieval form SCIAMACHY limb measurements, 9th Atmospheric Limb Workshop, Saskatoon, SK,C anada, 12-14 June, 2017.
2. A. Rozanov, C. Arosio, K.-U. Eichmann, E. Malinina, V. Sofieva, K. Weigel, N. Rahpoe, V. Rozanov, H. Bovensmann and J. P. Burrows, Remote sensing of the Earth’s atmosphere in limb viewing geometry: recent developments at the University of Bremen, International Symposium om Atmospheric Radiation and Dynamics, 27-30 June 2017 in Saint-Petersburg-Petrodvorets, Russia.

5.19 *hbk00055*: Investigating the biogeochemistry of the high latitudes during the period of rapid change: modeling and satellite retrievals

HLRNProject ID:	hbk0055
Run time:	IV/2017 – III/2018
Project Leader:	Prof. Dr. A. Bracher[1]
Project Scientists:	S. Losa, M. A. Soppa, M. Losch
Affiliation:	Alfred-Wegener-Institut Helmholtz Centre for Polar and Marine Research, Bremerhaven

[1] also professor at University of Bremen

Overview

The aim of this computing project is to obtain long-term (over decades) time series of ocean biogeochemical model simulations and satellite retrievals to analyse the changes in biodiversity and biogeochemical cycling observed over the last 20-30 years in the Polar regions (the Southern and Arctic Oceans) and to improve our understanding of possible interactions between the open water, sea ice, snow, ocean biogeochemistry and ecosystem and chemical composition of the Atmospheric Boundary Layer under the recently observed climate changes. Within the HLRN project, the coloured dissolved organic matter (CDOM) and phytoplankton dynamics as well as phytoplankton diversity in response to Arctic Amplification are simulated with a version of the biogeochemical model Darwin (Dutkiewicz et al., 2015) coupled to the Massachusetts Institute of Technology General Circulation Model (MITgcm, MITgcm Group, 2012). Satellite retrievals of chlorophyll “a” concentrations (Chla) for various phytoplankton functional types (PFTs) - diatom, coccolithophores, cyanobacteria - are derived based on synergistic use (SynSenPFT, Losa et al., 2017) of multi-spectral-based (Soppa et al. 2014, 2016) and hyper-spectral-based (Bracher et al. 2009, Sadeghi et al. 2012) phytoplankton absorption information. For independent evaluation of the model and satellite retrieved PFT data we use *in situ* marker phytoplankton pigments determined with high precision liquid chromatography (HPLC) sampled and compiled by AWI "Phytooptics" team in cooperation with other researchers from AWI since 2009 onwards and within the currently running HGF-project FRAM in the Arctic Ocean (Greenland Sea, Laptev Sea, Central Arctic).

Results

Within this computing project, a version of SynSenPFT Chlorophyll “*a*” concentration (Chla) product combining hyper- and multispectral-based satellite retrievals has been obtained for diatom, coccolithophores and cyanobacteria for the period of August 2002 – March 2012 (Losa et al. 2017). To further improve the SynSenPFT algorithm and product we have performed several experiments considering the spatial radius of the hyper-spectral data influence that would allow increasing the weight of the hyperspectral information in the synergistic product. Figure 1 depicts monthly mean diatom Chla obtained with OC-PFT, PhytoDOAS and SynSenPFT (with a small so far radius of PhytoDOAS data influence introduced) for the Arctic (ARCT) Longhurst’s biogeochemical province (Longhurst 1998). It shows that the use of such a radius allows to get the OC-PFT Chla nudged towards the PhytoDOAS information surrounding when there are no PhytoDOAS retrievals at the analysed location.

The allocated NPLs were also used for Darwin-MITgcm model sensitivity studies. The calibration of a 6-PFTs version of the Darwin-MITgcm has allowed to improve significantly the simulated phenology and dominance of the observed PFTs in the Southern Ocean (Figure 2, 3) and provide recommendations for the Arctic Ocean set up (including the impact of CDOM on distribution of PFTs). For the Southern Ocean, the experiments demonstrate model's skills in simulating some of the observed spatial distributions of *Phaeocystis ant.* (Alvain et al., 2008), however, the competition between to types of haptophytes (coccolithophores and *Phaeocystis ant.*) still remains a delicate issue. The results of our sensitivity studies have shown that simulating a too early (relative to what is observed) appearance of diatom blooms in the Southern Ocean – a general feature of all (global ocean) biogeochemical models (as well in the Darwin model set up presented in the study by Dutkiewicz et al. 2015) – could be explained by the fact that the models do not represent well the observed diversity in diatom size: smaller and "slightly silicified and fast growing" diatoms observed at the lower latitudes and larger cell size of "strongly silicified slowly growing cells" at high latitudes (Quéguiner 2013, Deppeler&Davidson, 2017). To tackle this problem, we have introduced two size classes of diatoms (large and small), which leads to improvement of the model – observations agreement for the Southern Ocean PFT phenology and spatial distribution (Soppa et al., 2016, Alvain et al., 2008).

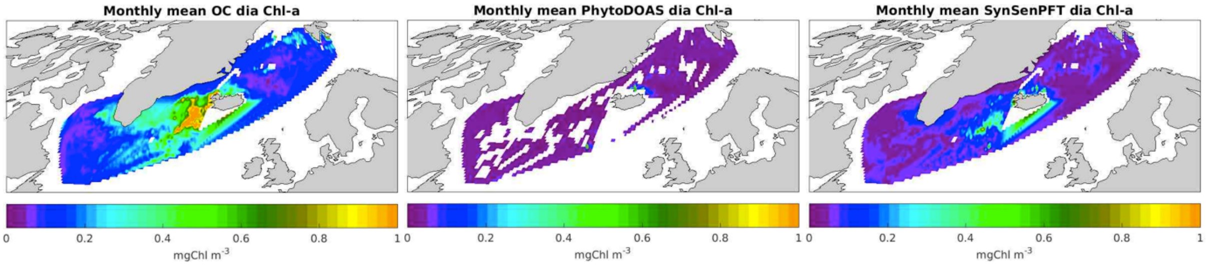

Fig. 1: June 2010 monthly mean Chla of diatoms in ARCT Longhurst's biogeochemical province: left – based on multi-spectral OC-PFT (Soppa 2014, 2017); middle – PhytoDOAS hyper-spectral PFT retrievals (Bracher et al. 2009, Sadeghi et al. 2012a); right – SynSenPFT synergistically combining the PhytoDOAS PFT retrievals and OC-PFT.

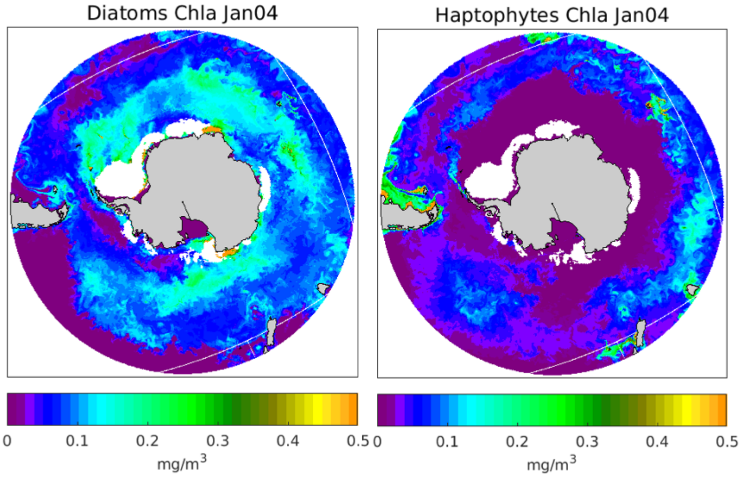

Fig. 2: Spatial distribution of the diatoms and haptophytes chlorophyll *"a"* in the Southern Ocean for January 2004.

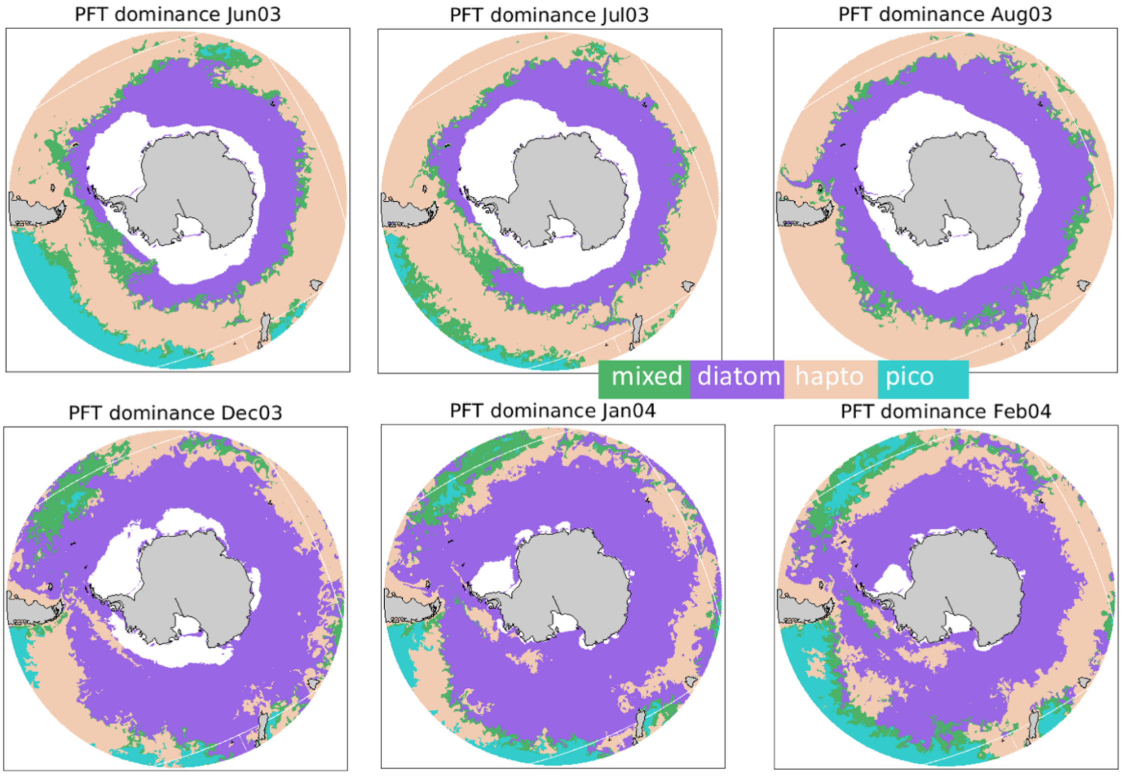

Fig. 3: Spatial distribution of the dominant PFTs in the Southern Ocean (pico represents *Prochlorococcus*), to be compared against Alvain et al. 2008 and Dutkiewicz et al. 2015.

Outlook

The SynSenPFT (Losa et al., 2017) will be further extended and updated to account for more information from current hyper-spectral (OMI) measurements and new multispectral Sentinel-3 data with better spatial and temporal coverage. The combined long time series of model and satellite-derived information on PFTs and CDOM absorption will be used to investigate existing relationships and feedbacks between the Arctic climate change, the ocean biogeochemistry and atmospheric oxidative capacity, which is one of the scientific tasks of the related project "Arctic Amplification: Climate Relevant **A**tmospheric and Surfa**C**e Processes, and Feedback Mechanisms **(AC)**^{3}" within the establishment of Transregional Collaborative Research Centre TR 172. The time series of the satellite PFT Chla retrievals and MITgcm-Darwin biogeochemical model integrations (over the period of 1991 – 2016) for the Southern Ocean are to support the DFG research "Antarctic phytoplankton in response to environmental changes studied by a synergetic approach using multi- and hyper-spectral satellite data (PhySen)" within the framework of the DFG-Priority Program 1158 "Antarctic Research".

Publications

1. Losa, S. N., Soppa, M. A., Dinter, T., Wolanin A., Brewin R. J. W., Bricaud A., Oelker, J., Peeken I., Gentili B., Rozanov V. V., Bracher, A. (2017). *Corrigendum: Synergistic exploitation of hyper- and multispectral Sentinel measurements to determine Phytoplankton Functional Types (SynSenPFT)*, Frontiers in Marine Science*, 4, 258. Doi: 10.3389/fmars.2017.00258*
2. Losa, S. N., Soppa, M. A., Dinter, T., Wolanin A., Brewin R. J. W., Bricaud A., Oelker, J., Peeken I., Gentili B., Rozanov V. V., Bracher, A. (2017). *Synergistic exploitation of hyper- and multispectral Sentinel measurements to determine Phytoplankton Functional Types (SynSenPFT)*, Frontiers in Marine Science*, 4, 203. Doi: 10.3389/fmars.2017.00203.*

Presentations

1. Losa, S. N., Soppa, Oelker, M. A., Losch, M., Dinter, T., Richter, A., Brache, A. and Burrows, J. P., *Antarctic phytoplankton in response to environmental changes studied by a synergistic approach using multi- and hyper-spectral satellite data (PhySyn)*, DFG Koordinations-Workshop SPP 1158, Erlangen, 20 – 22 September 2017.
2. Losa, S. N., Soppa, M. A., Oelker, J., Dinter, T., Losch, M., Dutkiewicz, S., Richter, A., Rozanov, V. V., Burrows, J. P., Bracher, A. *Estimating the high latitude phytoplankton diversity based on multi- and hyper-spectral satellite retrievals*. International Ocean Colour Science (IOCS) Meeting, Lisbon (Portugal), 15 – 18 May 2017.
3. Losa, S. N., Soppa, M. A., Oelker, J., Dinter, T., Hellmann, S., Losch, M., Dutkiewicz, S., Richter, A., Rozanov, V. V., Burrows, J. P., Bracher, A. *Investigating the Arctic phytoplankton variability and diversity based on modeling and satellite retrievals*. (AC)^3 Science Conference, Bremen, 27 – 29 March 2017.
4. Losa, S. N., Oelker, Soppa, M. A., J., Dinter, T., Losch, M., Dutkiewicz, S., Richter, A., Burrows, J. P., Bracher, A. *Investigating the Antarctic phytoplankton diversity based on modeling and satellite retrievals*. EGU General Assembly, Vienna, Austria, 23–28 April 2017.

References

1. Bracher A., Vountas M., Dinter T., Burrows J.P., Röttgers R., Peeken I. (2009) *Quantitative observation of cyanobacteria and diatoms from space using PhytoDOAS on SCIAMACHY data*. Biogeosciences 6: 751-764.
2. Deppeler S. L. and Davidson A. T. (2017). *Southern Ocean Phytoplankton in a Changing Climate*. Front. Mar. Sci. 4:40. doi: 10.3389/fmars.2017.00040.
3. Dutkiewicz, S., Hickman, A. E., Jahn, O., Gregg, W. W., C. B. Mouw, C. B., and M. J. Follows (2015) *Capturing optically important constituents and properties in a marine biogeochemical and ecosystem model*. Biogeosciences 12, 4447-4481.
4. Longhurst. A. (1998) Ecological Geography of the Sea, Academic press.
5. Menemenlis, D., Campin, J.-M., Heimbach, P., Hill, C., Lee, T., Nguyen, A., Schodlock, M., and H. Zhang (2008) *High resolution global ocean and sea ice data synthesis*, Mercator Ocean Quartely Newsletter, 31, 13–21.
6. MITgcm Group (2012), *MITgcm Manual*, Online documentation, MIT/EAPS, Cambridge, MA 02139, USA.
7. Quéguiner, B. (2013), *Iron fertilization and the structure of planktonic communities in high nutrient regions of the Southern Ocean*, Deep Sea Research Part II: Topical Studies in Oceanography, 90: 43–54, doi: 10.1016/j.dsr2.2012.07.024.
8. Sadeghi, A., Dinter, T., Vountas, M., Taylor, B. B., Soppa, M. A., Peeken, I., and A. Bracher (2012). *Improvements to the PhytoDOAS method for identification of coccolithophores using hyperspectral satellite data*. Ocean Sciences 8:1055-1070.
9. Soppa, M. A., Hirata, T., Silva, B., Dinter, T., Peeken, I., Wiegmann, S., Bracher, A. (2014) *Global Retrieval of Diatom Abundance Based on Phytoplankton Pigments and Satellite Data*. Remote Sensing, 6(10), 10089-10106.
10. Soppa, M. A., Peeken, I., and Bracher, A. (2017). *Global chlorophyll "a" concentrations for diatoms, haptophytes and prokaryotes obtained with the Diagnostic Pigment Analysis of HPLC data compiled from several databases and individual cruises*. doi:10.1594/PANGAEA.875879.
11. Soppa, M., Völker, C. and Bracher, A. (2016). *Diatom Phenology in the Southern Ocean: Mean Patterns, Trends and the Role of Climate Oscillations*, Remote Sensing, 8 (420), 1–17.

5.20 ***hbk00057:*** Persistent ozone depletion in the tropical stratosphere: identifying possible reasons

HLRNProject ID:	hbk00057
Run time:	I/2017 – II/2018
Project Leader:	Dr. Alexei Rozanov
Project Scientists:	E. Galytska
Affiliation:	Institute of Environmental Physics, University of Bremen

Overview

The crucial role of the stratospheric ozone for the thermal balance of the Earth's atmosphere as well as for the atmospheric dynamics, biosphere and human health determines the continuous interest of the scientific community to the state of the stratospheric ozone layer. After the anthropogenic emission of halogenated ozone depleting species has been ruled out by Montreal Protocol and its amendments the severe ozone decline discovered in early eighties of the last century began to slow down and even some indications of the ozone recovery have been inferred from observations (Newchurch et al., 2003; WMO 2007, 2011; Yang et al., 2006). However, when analyzing the vertically resolved time series of ozone in the tropics, the ozone recovery is seen in the middle to lower stratosphere (below about 30 km) while a significant ozone depletion is observed at altitudes of about 35 km (Eckert et al., 2013; Gebhardt et al., 2014; Kyrölä et al., 2013, Sofieva et al., 2017). Being vertically integrated these opposite changes result in a slightly positive trendwhich explains the signatures of a recovery seen in the observations of the ozone total column.

In relation to the expected impact of the Montreal Protocol and its amendments, the negative trends in the tropical stratospheric ozone observed around 35 km are quite surprising and not sufficiently explained so far. Investigations of measurements of ozone and N_2O from HALOE, MLS and ACE-FTS instruments have recently been done by Nedoluha et al. (2015) showing an observed decrease in N_2O associated with an increase in NO_y which can cause the observed depletion of ozone.

This study is focused at the investigation of the vertical distributions of NO_2 and BrO retrieved from SCIAMACHY limb measurements to assess if the behavior of a further member of NO_y family (NO_2) is consistent with the findings of Nedoluha et al. (2015) and if halogen species might have a significant contribution to the ozone depletion mechanisms in this latitude/altitude region. The investigation includes modeling studies using a Chemical Transport Model (CTM) to evaluate if the observed behavior of the species can be reproduced by the model and if the observed trends in the tropical stratospheric ozone can be explained by the observed trends in both NO_2 and BrO. Furthermore, possible mechanisms of the ozone destruction will be investigated by analyzing (anti-)correlations between the time series of different species. Due to a complex interaction between different chemically active species and dynamic processes a supporting modeling study is essential for the interpretation of the obtained results. A consideration of BrO is believed to be important as on the one hand it is an ozone depleting species and on the other hand it reacts with nitrogen species to form inactive reservoir species. Therefore, this additional knowledge enables us to constrain CTM in a better way.

Results

As only 70% of the requested computing time was approved in the original application while full-lengths time series were needed to calculate trends and initiate the model investigations with the SLIMCAT/TOMCAT CTM in collaboration with the University of Leeds, UK, a reduced quality retrieval was performed for NO_2 at first. This decision was justified by the fact that substantially shorter time series are not useful for a calculation of trends as the associated error becomes unacceptable, while uncertainty in each single data point is less crucial. The shortcomings of the reduced quality retrieval were reduced spectral and field of view sampling as well as neglecting the influence of the stratospheric aerosol and surface albedo. While the errors due to the first two simplifications are rather random, the latter two might results is a certain drift of the resulting time series. Nevertheless the obtained results were useful to initiate the modeling studies.

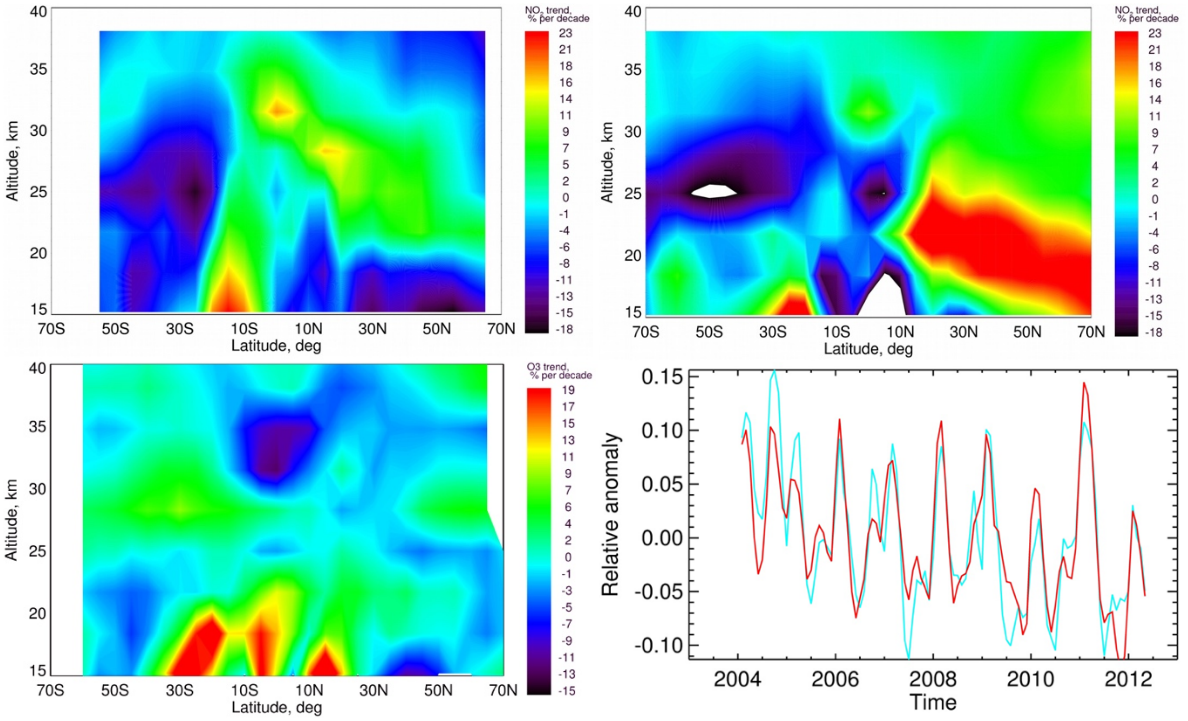

Fig. 6: Upper panels:NO_2 trends from January 2004 to April 2012 from SCIAMACHY observations (left) and SLIMCAT model (right). Lower left panel: stratospheric ozone trends retrieved from SCIAMACHY limb measurements (V3.5). Lower right panel: normalized time series of ozone (cyan) inverse normalized time series of NO_2 (red) at 34 km in tropics (10˚S - 10˚N). See text for details how to calculate the plotted time series.

Fig. 6 shows NO_2 trends from January 2004 to April 2012 from SCIAMACHY observations (preliminary results from the reduced quality data set) in the upper left panel and from SLIMCAT modelsimulations in the upper right panel. The plot reveals that both observations and model show similar trend structures, although some quantitative differences are observed. For the altitude and vertical range of the main interest (30-35km, tropics) one observes an increase in NO_2 amounts by 5-16% per decade from the observations and 5-14% from the model. The lower left panel of Fig. 6 shows the ozone trend derived from the SCIAMACHY limb measurements, which were obtained in the framework of the project hbk00045 at the Institute of Environmental Physics, University of Bremen. It is clearly seen from the plot that the location of high negative trends in ozone (30-35 km altitude range, 10˚S - 10˚N latitude band) is essentially the same as that of high positive trends in NO_2. The lower right panel of Fig. 6 shows in cyan the normalized time series of ozone at 34 km, calculated as $\hat{T}_{O_3} = \frac{T_{O_3}}{\overline{T}_{O_3}} - 1$, and in red the inverse normalized time series of NO_2 at the same altitude, calculated as $\hat{T}_{NO_2} = 1 - \frac{T_{NO_2}}{\overline{T}_{NO_2}}$. Here, T is the monthly zonal mean time series of ozone or NO_2 (depending on the subscript) and $\overline{T}$ denotes the averaging of the corresponding time series over the whole observation period. All data were averaged within 10˚S - 10˚N latitude range. One clearly sees a very well correlation of the plotted time series, which means a high anti-correlation of the observed time series of ozone and NO_2. The observed strong anti-correlation between the behavior of the ozone and NO_2 amounts provides an indication that the ozone depletion in the altitude/latitude range of interest is mainly due to NOx chemistry. Preliminary investigations with the SLIMCAT model show that the observed increase of NO2 is most probably due to dynamic reasons. The investigations are however still in progress. A corresponding paper is in preparation.

Outlook

The full quality retrieval of vertically resolved NO_2 time series from SCIAMACHY limb observations is currently in progress. The obtained results will be used to assure that the remaining differences in the observed and modeled trends are not related to the shortcomings of thereduced quality retrieval. Furthermore, modeling activities are to be continued to assess the ozone and NO2 trends and analyze possible driving mechanisms. Furthermore, vertically resolved time series of BrO will be obtained using an improved retrieval algorithm. The obtained data will be used to analyze the role of bromine compounds in the tropical stratospheric ozone budget and investigate if the observed BrO amounts in the stratosphere agree with the model predictions.

Presentations

Galytska, E., Chipperfield, M.P., Rozanov, A., Dhomse, S., Burrows, J.P., Stiller, G.: *Understanding decadal NO_2 and O_3 changes in the tropical stratosphere by means of chemistry-transport models*, Annual Science Meeting of Institute for Climate and Atmospheric Science, 2 November 2017, Leeds, UK.

References

Eckert, E., von Clarmann, T., Kiefer, M., Stiller, G. P., Lossow, S., Glatthor, N., Degenstein, D. A., Froidevaux, L., Godin-Beekmann, S., Leblanc, T., McDermid, S., Pastel, M., Steinbrecht, W., Swart, D. P. J., Walker, K. A., and Bernath, P. F.: *Drift-corrected trends and periodic variations in MIPAS IMK/IAA ozone measurements*, Atmos. Chem. Phys., 14, 2571-2589,2014.

Gebhardt, C., Rozanov, A., Hommel, R., Weber, M., Bovensmann, H., Burrows, J. P., Degenstein, D., Froidevaux, L., and Thompson, A. M.: *Stratospheric ozone trends and variability as seen by SCIAMACHY from 2002 to 2012*, Atmos. Chem. Phys., 14, 831-846, doi:10.5194/acp-14-831-2014, 2014.

Kyrölä, E., Laine, M., Sofieva, V., Tamminen, J., Päivärinta, S.-M., Tukiainen, S., Zawodny, J., and Thomason, L.: *Combined SAGE II-GOMOS ozone profile data set for 1984-2011 and trend* *analysis of the vertical distribution of ozone*, Atmos. Chem. Phys., 13, 10645-10658, doi:10.5194/acp-13-10645-2013, 2013.

Nedoluha, G. E., D. E. Siskind, A. Lambert, and C. Boone, *The decrease in mid-stratospheric tropical ozone since 1991*, Atmos. Chem. Phys., 15, 4215-4224, 2015, doi:10.5194/acp-15-4215-2015.

Newchurch, M. J., Yang, E.-S., Cunnold, D. M., Reinsel, G. C., Zawodny, J. M., and RussellIII, J. M.: *Evidence for slowdown in stratospheric ozone loss: First stage of ozone recovery*, J. Geophys. Res., 108, 4507, doi:10.1029/2003JD003471, 2003.

Sofieva, V. F., Kyrölä, E., Laine, M., Tamminen, J., Degenstein, D., Bourassa, A., Roth, C., Zawada, D., Weber, M., Rozanov, A., Rahpoe, N., Stiller, G., Laeng, A., von Clarmann, T., Walker, K. A., Sheese, P., Hubert, D., van Roozendael, M., Zehner, C., Damadeo, R., Zawodny, J., Kramarova, N., and Bhartia, P. K.: *Merged SAGE II, Ozone_cci and OMPS ozone profile dataset and evaluation of ozone trends in the stratosphere*, Atmos. Chem. Phys., 17, 12533-12552, https://doi.org/10.5194/acp-17-12533-2017, 2017.

WMO: Scientific Assessment of Ozone Depletion: 2006, *Global Ozone Research and Monitoring Project Report 50*, World Meteorological Organization, Geneva, www.wmo.int/pages/prog/arep/gaw/ozone2006/ozoneasstreport.html, 2007.

WMO: Scientific Assessment of Ozone Depletion: 2010, *Global Ozone Research and Monitoring Project Report 52*, World Meteorological Organization, Geneva, www.unep.ch/ozone/AssessmentPanels/SAP/ScientificAssessment2010/00-SAP-2010-Assement-report.pdf, 2011.

Yang, E.-S., Cunnold, D. M., Salawitch, R. J., McCormick, M. P., Russell III, J. M., Zawodny, J. M., Oltmans, S., and Newchurch, M. J.: *Attribution of recovery in lower-stratospheric ozone*, J. Geophys. Res., 111, D17309, doi:10.1029/2005JD006371, 2006.

5.21 *hbk00058:* Klimasimulationen der letzten glazialen Termination

HLRN-Projektkennung:	hbk00058
Laufzeit:	III/2017 – II/2018
Projektleiter:	Prof. Michael Schulz
Projektbearbeiter.	Dr. Matthias Prange, Dr. Pepijn Bakker
Institut / Einrichtung:	MARUM – Zentrum für Marine Umweltwissenschaften, Universität Bremen

Überblick

Die letzte eiszeitliche Termination (21.000-11.000 Jahre vor heute) stellt eine Schlüsselperiode für das Verständnis von globalen Klimaveränderungen dar. Diese Phase ist das geologisch am besten dokumentierte Beispiel für eine massive Reorganisationdes Erd- und Klimasystems, bei der gewaltige Eismassen vom amerikanischen und eurasischen Kontinent, aber auch von der Antarktis abschmolzen und sich der globale Meeresspiegel infolgedessen um rund 120 m hob. Globale Temperaturen stiegen um mehrere Grad Celsius und der atmosphärische Kohlendioxid-Gehalt nahm um fast 100 ppmv zu. Dieser Übergang vom Letzten Glazialen Maximum (LGM) in die jetzige Zwischeneiszeit (Interglazial) geschah jedoch nicht gleichmäßig, sondern war vielmehr durch mehrere abrupte Teilübergängege kennzeichnet. Dabei wurde die extreme Kaltphase in nördlichen Breiten des Heinrich-Stadials 1 (ca.18.000-14.700 Jahre vor heute) von der wärmeren Periode des Bölling-Alleröd-Interstadials (ca. 14.700-12.800 Jahre vor heute) abgelöst, bevor es mit dem Jüngeren-Dryas-Stadial (12.800-11.700 vor heute) vorübergehend wieder kälter wurde. Während dieser Klimaschwankungen auf der Jahrtausendskala reagierten die beiden Hemisphären zu weiten Teilen entgegengesetzt hinsichtlich Temperatur- und Niederschlagsveränderungen. Hierfür werden Schwankungen in der atlantischen Umwälzzirkulation (Atlantic Meridional Overturning Circulation, AMOC) verbunden mit Störungen der nordatlantischen Tiefenwasserbildung verantwortlich gemacht: Eine schwache Zirkulation transportiert weniger Wärme in den Nordatlantik und führt somit zu einer Abkühlung der hohen nördlichen Breiten. Obwohl ein grundsätzliches Verständnis der Klimaphasen derletzten Termination vorhanden ist, sind zahlreicheProzesse und deren Wechselwirkungen nur ansatzweise verstanden. Unter anderem sollen folgende Fragestellungen in diesem Projekt untersucht werden:

- Wie hängen Stabilitätseigenschaften der AMOC von den sich verändernden Randbedingungen ab?
- Inwieweit reagiert die Ozeanzirkulation nichtlinear auf äußere Störungen?
- Kann der Ozean tieffrequente (d.h. Jahrhundert- bis Jahrtausendskala) Klimavariabilität ohne äußere Antriebe (d.h. intern) generieren?
- Welche Rolle spielt die Kryosphäre für die AMOC-Stabilität und inwieweit verstärken Meereiseffekte den Einfluss vonAMOC-Schwankungen auf das globale Klima?

Als erster Schritt zur Untersuchung des Stabilitätsverhaltens der Ozeanzirkulation und atmosphärischer Wechselwirkungen wurden Klimamodell-Experimente mit vorgeschriebenen variierenden Eisschilden und Schmelzwasserflüssen durchgeführt. Dieses von den großen nordamerikanischen und eurasischen Eisschilden stammende Schmelzwasser wird meist als hauptverantwortlich für die starken AMOC- und Klimaschwankungen der letzten eiszeitlichen Termination betrachtet, indem es die Dichte des Oberflächenwassers im Nordatlantik soweit reduzierte, dass sich in weiten Gebieten kein Tiefenwasser mehr bilden konnte.

Methodik

Wir verwenden Version 1.2 des Community Earth System Model (CESM1.2). Die atmosphärische Modellkomponente hat eine horizontale Gitterauflösung von ca. 2° und 26 Schichten in der Vertikalen, während das Ozeanmodell mit einem 1°-Gitter auf 60 Niveaus läuft. Zunächst wurde untersucht, inwiefern die Stabilität der AMOC von den drei wichtigsten, sich während der eiszeitlichen Termination ändernden Randbedingungen abhängt: der Größe der nordhemisphärischen Eisschilde, der atmosphärischen Treibhausgaskonzentration sowie den Erdorbitalparametern. Hierzu wurden Schmelzwasserexperimente unter LGM (21.000 Jahre vor heute, im Folgenden 21 ka) und deglazialen (15.200 Jahre vor heute mit wesentlich kleineren nordamerikanischen und europäischen Eisschilden, im Folgenden 15,2 ka) Randbedingungen durchgeführt und untersucht. In beiden Fällen beträgt die Schmelzwasserzufuhr 100 mSv (1 $Sv=10^6$ m^3/s) und wurde 200 Jahre lang konstant in den Nordatlantik eingetragen, um anschließend abrupt wieder beendet zu werden. Nach einer weiteren Integration von mehreren hundert Jahren wurde eine zweite Schmelzwasserstörung eingebracht, identisch der ersten, um das transiente Verhalten der ozeanischen Zirkulation besser untersuchen zu können und die Signifikanz der Ergebnisse zu testen. Zusätzlich wurden weitere Sensitivitätsexperimente durchgeführt, um die Ursachen für mögliche Unterschiede in der AMOC-Stabilität zu identifizieren. In diesen sogenannten “single forcing experiments” wurden nacheinander LGM Treibhausgaskonzentrationen und Erdorbitalparameter unter ansonsten “15,2 ka”-Randbedingungen verwendet, sowie “15,2 ka”-Eisschilde unter ansonsten LGM-Randbedingungen. Unter allen Konfigurationen wurden Schmelzwasserexperimente (100 mSv, 200 Jahre) durchgeführt. Ferner wurden Sensitivitätsstudien durchgeführt, in denen der Schmelzwassereintrag in verschiedenen Regionen stattfindet (nördlicher Nordatlantik, Europäisches Nordmeer, Nordpolarmeer).

Erste Ergebnisse

Unsere Untersuchungen zeigen, dass die AMOC, unabhängig von den Treibhausgas-, Erdorbital- und Eisschildrandbedingungen während der Termination monostabil bleibt, d.h. massive Schmelzwassereinträge oder andere Störungen sind nicht in der Lage, die Ozeanzirkulation beständig (d.h. auch nach Beendigung der Störung) in einen anderen Zustand zu versetzen. Dennoch haben die Schmelzwassereinträge zumindest vorübergehend einen starken, abschwächenden Effekt (von ca. 22 Sv auf 6 Sv unabhängig von den Randbedingungen) auf die AMOC (Abb. 1). Die Region, in welcher der Schmelzwassereintrag erfolgt, spielt eine überragende Rolle für die Abschwächung der AMOC. Schmelzwassereinträge in den nördlichen Nordatlantik haben dabei einen weitaus stärkeren Effekt auf die AMOC als beispielsweise gleichgroße Einträge ins Nordpolarmeer.

Nach dem Verschwinden der Schmelzwassereinträge erholt sich die AMOC wieder. Ein wesentlicher Unterschied zwischen den LGM und Deglazial-Experimenten ist dabei die Zeitspanne bis zum Einsetzen des Erholungsprozesses. In beiden Fällen erhöht sich der AMOC-Transport nur geringfügig in den ersten ca. 100 Jahren nach Beendigung der

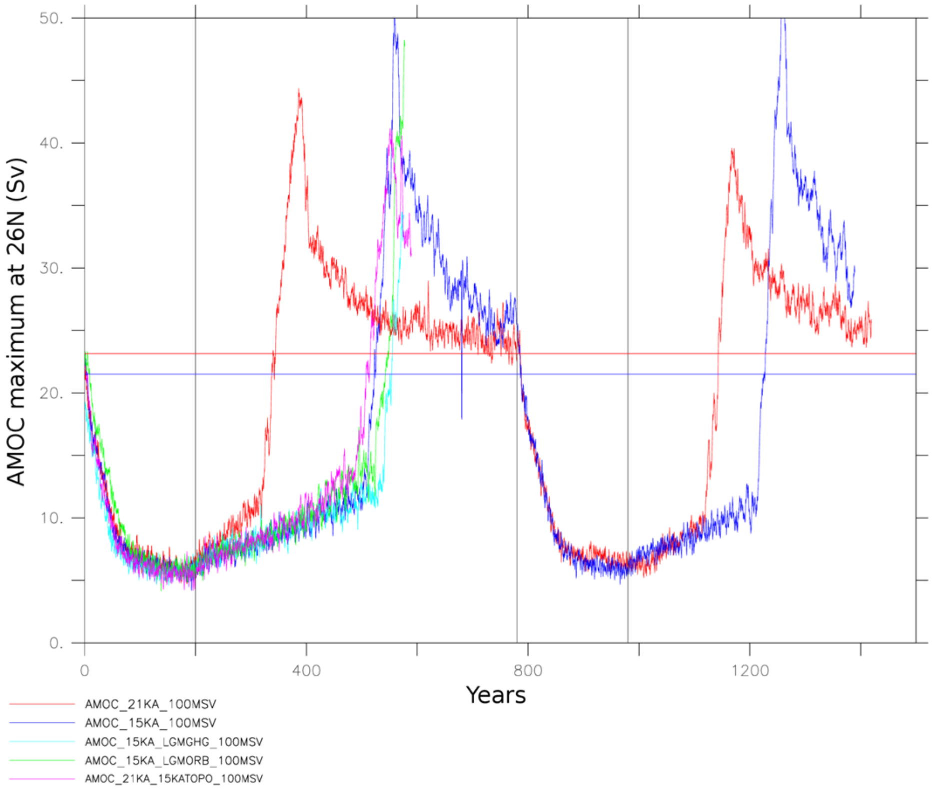

Abb. 1: Simulierte zeitliche Entwicklung der AMOC-Stärke (entspricht in etwa der Produktionsrate von nordatlantischem Tiefenwasser). Rote und blaue Kurven entsprechen den LGM- (21 ka) bzw. Deglazial- (15,2 ka) Experimenten, denen zwei Schmelzwasserepisoden von 100 mSv (Schmelzwassereintrag in den nördlichen Nordatlantik) aufgeprägt wurden (angezeigt durch vertikale Linien, d.h. Modelljahre 0-200 und 790-990). Horizontale Linien zeigen die AMOC-Stärke der ungestörten LGM- (rot) und Deglazial- (blau) Simulationen an. Weitere Kurven zeigen die Ergebnisse verschiedener Sensitivitätsexperimente: Deglazial mit 21 ka Treibhaus-gaskonzentrationen (hellblau), Deglazial mit 21 ka Erdorbitalparametern (grün) und LGM mit 15,2 ka Eisschildkonfiguration (violett).

Schmelzwasserzufuhr. Anschließend zeigt das LGM-Experiment eine rapide Verstärkung der AMOC, einen Überschwinger und schließlich wieder eine langsame leichte Abschwächung bis die ursprüngliche AMOC-Stärke vor Beginn der Schmelzwasserstörung wieder erreicht ist (Abb. 1). In der Deglazial-Simulation zeigt sich ein ähnlicher Verlauf, allerdings ist das rapide Wiedererstärken der AMOC um ca. 200 Jahre verzögert. Diese Abfolge wiederholt sich qualitativ nach der zweiten Schmelzwasserstörung. Zur Untersuchung der Faktoren, die den Unterschied in den AMOC-Erholungszeiten unter LGM und Deglazial-Bedingungen bestimmen, wurden mehrere Sensitivitätsexperimente durchgeführt. Es zeigt sich, dass die Höhe des nordamerikanischen Eisschildes hierfür ausschlaggebend ist (der Eisschild ist bei 15,2 ka deutlich kleiner und niedriger als bei 21 ka), während Unterschiede in den Treibhausgaskonzentrationen und Erdorbitalparametern nur einen geringen Einfluss haben (Abb. 1). Insgesamt zeigt sich, dass die verzögerte AMOC-Erholung im Deglazial-Experiment eine deterministische Eigenschaft des Klimasystems mit einer 15,2 ka Eisschildkonfiguration ist. Die gekoppelten Meereis-Ozean-Prozesse, die zum Überschwinger und Wiedererstärken der AMOC führen, werden zurzeit weiter untersucht. Zusammenfassend können unsere ersten

Ergebnisse aber bereits wichtige Antworten auf die anfangs gestellten Fragen liefern: Tieffrequente interne (ozeanische) Schwankungen im deglazialen Klima konnten in dieser Konfiguration des CESM nicht gefunden werden, abrupte Kälteperioden wie das Heinrich-Stadial 1 und die Jüngere Dryas wären demzufolge am wahrscheinlichsten durch Schmelzwassereinträge induziert, wobei die Länge der Kälteperioden durch Höhe und Ausdehnung der Eisschilde beeinflusst wurde. Die AMOC-Störungen führten zu Lufttemperaturabnahmen von bis zu 10°C in hohen nördlichen Breiten des Atlantiks, wobei Meereiseffekte durch meridionale Verlagerung der Meereiskante und damit einhergehende Veränderungen der Albedo und turbulenter Wärmeflüsse zwischen Ozean und Atmosphäre eine wichtige Rolle als Verstärkungsmechanismus spielten. Unsere nächsten Untersuchungen werden sich mit Eisschild-Klima-Wechselwirkungen während der letzten glazialen Termination befassen. Hierzu koppeln wir CESM1.2 an ein dynamisch-thermodynamisches Eisschildmodell.

Das Projekt ist Teil des Arbeitspaketes 1.3 (WP1.3 – Long transient simulations) der durch das BMBF finanzierten nationalen Klimamodellierungsinitiative „PalMod – From the Last Interglacial to the Anthropocene“.

Vorträge / Poster

P Bakker, M Prange, I Rogozhina, *Sensitivity ofthe LGM climate to the uncertainty in PMIP4 ice sheet boundary conditions*, 1st PMIP4 conference, Stockholm, 25.09.-29.09.2017

5.22 *hbk00059:* Joint state-parameter estimation for the Last Glacial Maximum with CESM1.2

HLRN Project ID:	hbk00059
Run time:	05/2017 – 02/2018
Project Leader:	Prof. Dr. M. Schulz
Project Scientists:	J. García-Pintado
Affiliation:	Fachbereich Geowissenschaften, MARUM-- Zentrum für Marine Umweltwissenschaften, Universität Bremen

Overview

The PALMOD project, funded by BMBF, seeks to understand climate system dynamics and variability during the last glacial cycle. Specific topics are: i) to identify and quantify the relative contributions of the fundamental processes which determined the Earth's climate trajectory and variability during the last glacial cycle, ii) to simulate with comprehensive Earth System Models (ESMs) the climate from the peak of the last interglacial (the Eemian warm period) up to the present, including the changes in the spectrum of variability, and iii) to assess possible future climate trajectories beyond this century during the next millennia with sophisticated ESMs tested in such a way.

Relevant to this computing project proposal, an expected major outcome of the first (4-yr) phase of PALMOD is to obtain a comprehensive data synthesis of paleoclimatic conditions during the last glacial cycle, associated with explicit estimates of uncertainty. This involves combining in the best possible ways the outcome of long-term climate model simulations with the last generation of multi paleo proxy data (planktic foraminifera, diatoms, dinoflagellates, radiolaria, geochemical proxies as Mg/Ca in planktic foraminifera shells, etc.). For this, we are using a global climate model; the Community Earth System Model version 1.2 (CESM1.2), and assimilating homogenized multi-proxy observations, generated within the scope of PALMOD, into CESM. Ensemble reconstructions from the coupled model at the LGM are being analysed along with a transient higher resolution simulation of the post LGM-deglaciation.

Results

A number of analyses have been done in HLRN in the last year within this proposal. These involve synthetic tests to evaluate approaches for joint state-parameter estimation for multi-decadal paleoclimate reanalyses, and tests based on real of coral-based SST of the last millenium as basis to evaluate the approach to build the forward operator mapping model SST into coral Sr/Ca and coral dO^{18} records, extracted from the PAGES2k database.

Regarding the synthetic tests, the evaluation of the approaches to conduct joint state-parameter estimation is relevant as despite the computational availability of supercomputers as HLRN, complex ESMs as CESM are still very expensive to run. Also CESM, as other ESMs, does not have an adjoint code available, which limits the for assimilation of paleo-proxy data. As the high computational demand limits the number of runs that can be conducted for specific model configurations, in preparation for LGM run, a battery of tests have been conducted for preindustrial conditions, assimilating synthetic proxy data with the characteristics of the MARGO database (MARGO Project Members, 2009), whose results have been summarised in García-Pintado and Paul (submitted to Geoscientific Model Development). The MARGO data base, despite representing the state-of-the-art of multiproxy data-based syntheses for the

LGM, still is a sparse set of observations, where some big areas of the global ocean remain unobserved. Figure 1 shows the MARGO locations, indicating its various types of available data proxies.

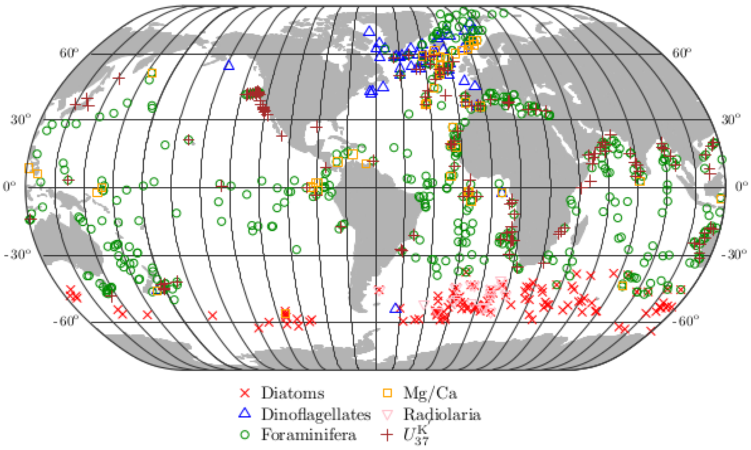

Fig. 1: MARGO database coverage (MARGO Project Members, 2009).

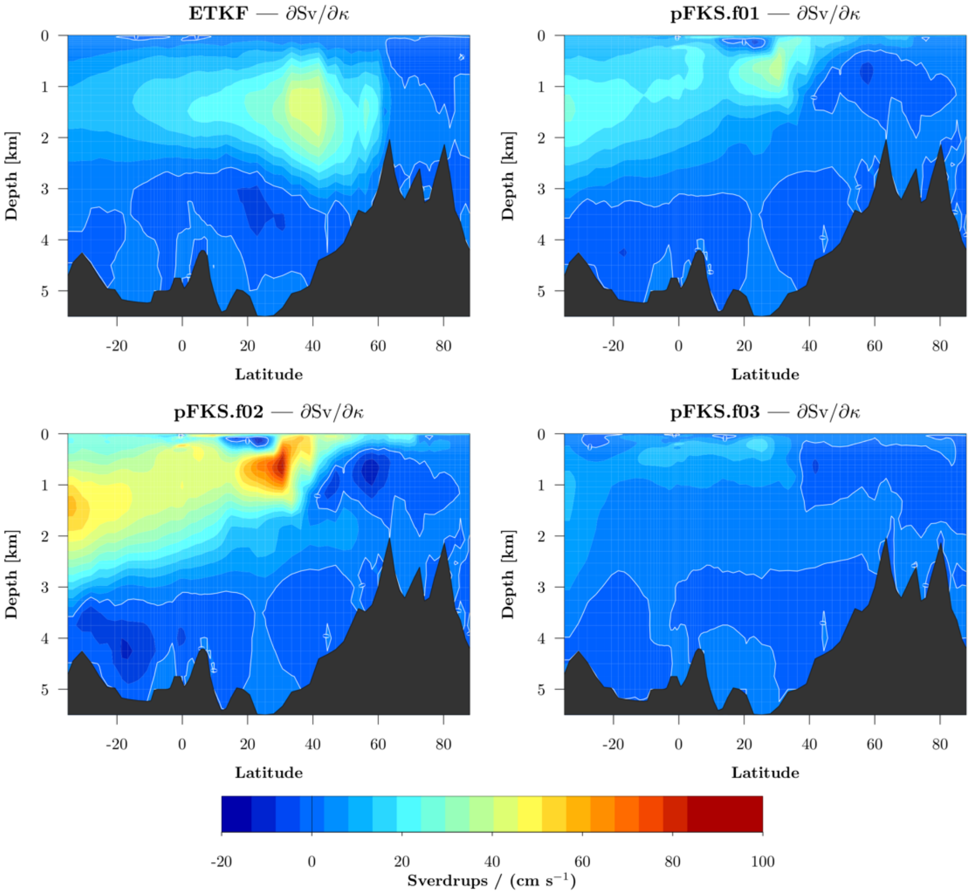

Fig. 2: CESM synthetic experiment. Sensitivity of the AMOC to the background vertical diffusion parameter of the KPP scheme in the ocean model estimated from an ensemble with m=60 members (ETKF), and estimated by the more limited conditional sampling along three loops in an iterative scheme (pFKF).

The results of these analyses have first served to evaluate the sensitivity of the multi-decadal climate, as provided by CESM simulations, to a number of selected model parameters in relationship with the global energy balance. As an example, for a given model setup, Figure 2 shows the sensitivity of a 20-year mean Atlantic Meridional Overturning Circulation (AMOC) to a parameter (κ) controlling the vertical diffusion in the model ocean component.

The MARGO-like observations were then assimilated into the CESM background, estimated as a 20-yr mean climatic fields, with a number of schemes based on the Kalman filter. As an example, Figure 3 shows the absolute decrease in bias resulting from an ETKF and a so-called parameter space Kalman smoother (García-Pintado and Paul, submitted)).

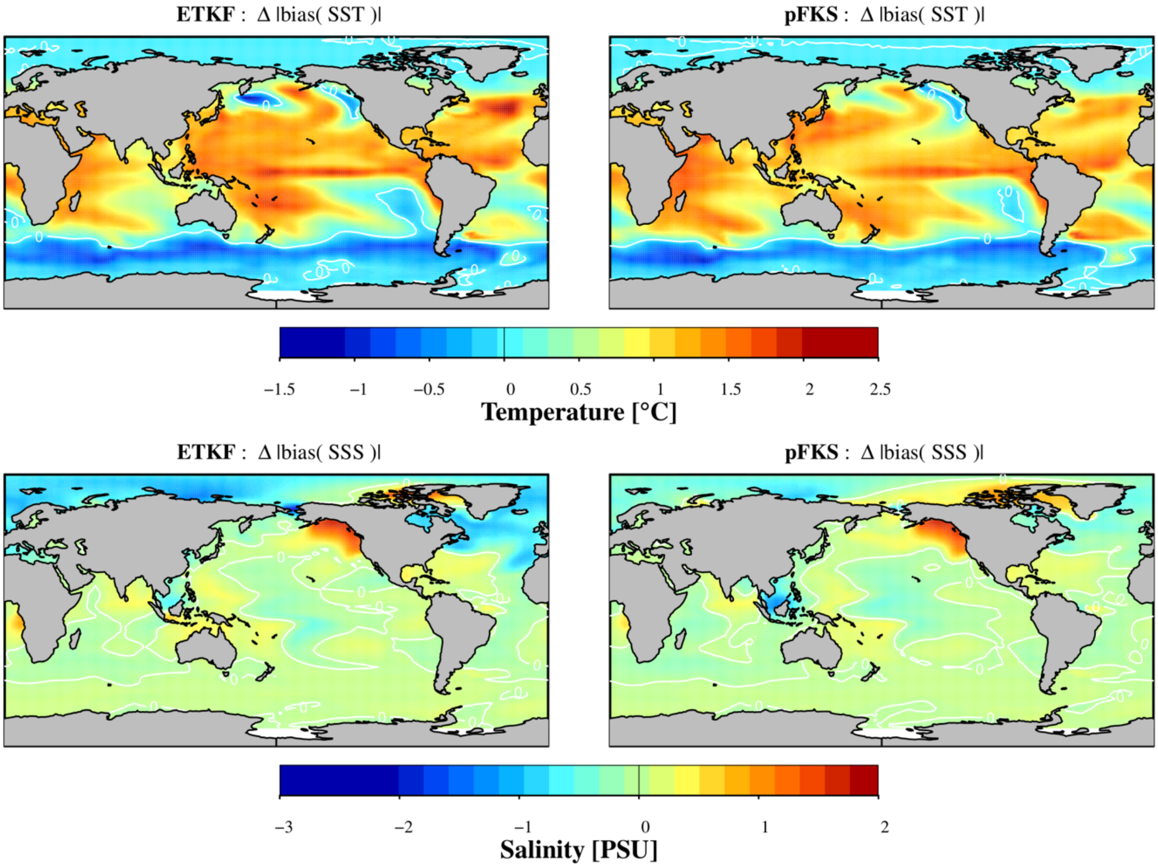

Fig. 3: CESM synthetic experiment. Absolute bias reduction for SST and SSS as a result of a new integration with the parameters estimated with the $ETKF_{60}$ and the pFKS. The statistics are the absolute bias between the background and the truth minus the absolute bias between the analysis and the truth. Thus, positive values are a net bias reduction.

Both schemes, the ETKF with 60 members ($ETKF_{60}$) and the pFKS, illustrated in Figure 3 show a general and very similar bias reduction and similar patterns in both sea surface temperature (SST) and sea surface salinity (SSS) as a result of the assimilation of the MARGO-like observations. However, the pFKS resulted from half the computational requirements of that requested for the ETKF. Both schemes reveal a lack of climate constraining by the sparse observations in high latitudes. This points out to the requirement of additional paleo-proxy observations or specific localisation schemes for dealing with the issue while retaining the log-range but significant and physical correlations. The additional experiments conducted with real coral-based proxy climate observations are now under study, and corresponding results will be described in future reports. Also the model has been setup and preliminary simulations have been conducted with LGM forcings, which are currently under evaluation.

Outlook

A new set of simulations and sensitivity tests are currently being evaluated at the T31 spectral resolution of atmospheric component of CESM (CAM5), for which a version including stable isotopes has been recently developed by NCAR-NASA and has been made available to the project. Upon the obtained results, as compared with the previous Finite Volume solvers, the decision has to be made about a final model configuration for the transient runs. The learning process from runs conducted up to this date is being evaluated for the design of the final assimilation scheme for the climate field reconstruction of the LGM, given available observations within PALMOD.

Publications

J. García-Pintado, A. Paul, *Parameter space Kalman smoothers for multi-decadal climate analysis in high resolution coupled Global Circulation Models*, Geoscientific Model Development (submitted)

References

MARGO Project Members [C. Waelbroeck, A. Paul, M. Kucera, A. Rosell-Melé, M. Weinelt, R. Schenider, A.C. Mix and 45 others] (2009) *Constraints on the magnitude and patterns of ocean cooling at the Last Glacial Maximum*. Nature Geosci. 2, 127-132, doi:10.1038/ngeo411.

5.23 hbk00060: North Pacific Ocean circulation and biogeochemistry in warming climate since the Last Glacial Maximum

HLRN Project ID:	hbk00060
Run time:	III/2017 – II/2018
Full project time:	08.2017 – 07.2020
Project Leader:	Prof. G. Lohmann
Project Scientists:	Dr. X. Gong, Dr. P. Scholz, Dr. V. Schourup-Kristensen, Dr. L. Lembke-Jene, Prof. Dr. R. Tiedemann
Affiliation:	Alfred Wegener Institute Helmholtz Center for Polar and Marine Research, Bremerhaven, Germany IUP, University Bremen, Bremen, Germany

Overview

North Pacific Ocean plays import roles in Earth climate system development, influencing climate not only thermally but also through currents and water mass distributions, also importantly via its biogeochemical processes. Moreover, paleoclimate and paleoceanogrpahic studies have suggested the varying roles of the North Pacific in changing climate and largely dependent on background climate conditions particularly. In this project, concerning the modern, instrumental observations of the on-going global warming, we aim to simulate the physical processes of the North Pacific overturning and its control onto the biogeochemical processes during the past climates through cold to warm phases since the last glacial maximum (LGM).

Strategically, our project correlates to the BMBF project: *“WTZ China–NOPAWAC-North Pacific Ocean in Warming Climates During the Quaternary”* (01.08.2017 - 31.07.2020). In addition, our work in this project succeeds from our previous HLRN projects, including ‘Climatic evolution in the marginal seas of the Northwest Pacific Ocean since the last glacial period until present day: changes in the formation of North Pacific Intermediate Water formation and their implications on the Pacific realm’ (HLRN project: hbk0042) and ‘Glacial-interglacial change of the biogeochemical process in the Pacific subarctic oceans’ (HLRN project: hbk0054).

Scientifically, we addressed our interest on the dependence of the North Pacific Ocean stratification on the warming background climate states, and its manipulation of the North Pacific marine primary productivity, remineralization and mid-depth anoxia. In particular, we focus on the oceanic CO_2 storage and its regulation by the biological vs. physical carbon pump.

Our main task in this project, according to our scientific targets, is to use the standalone ocean model Finite Element Sea Ice–Ocean Model (FESOM) and the coupled ocean-sea ice-biogeochemical FESOM-REcoM model to simulate three paleo-time slices: Mid Holocene (MH, 6ka), Early Holocene (EH, 9ka) and Last Glacial Maximum (LGM, 21ka), in addition to the Present-Day (PD) climate conditions. Concerning the simulation resource and computing time, we firstly run the stand-alone FESOM model to quasi-equilibrium states for each proposed climate, and then utilize the ocean state to do the simulations using coupled ocean-sea ice-biogeochemical FESOM-REcoM model

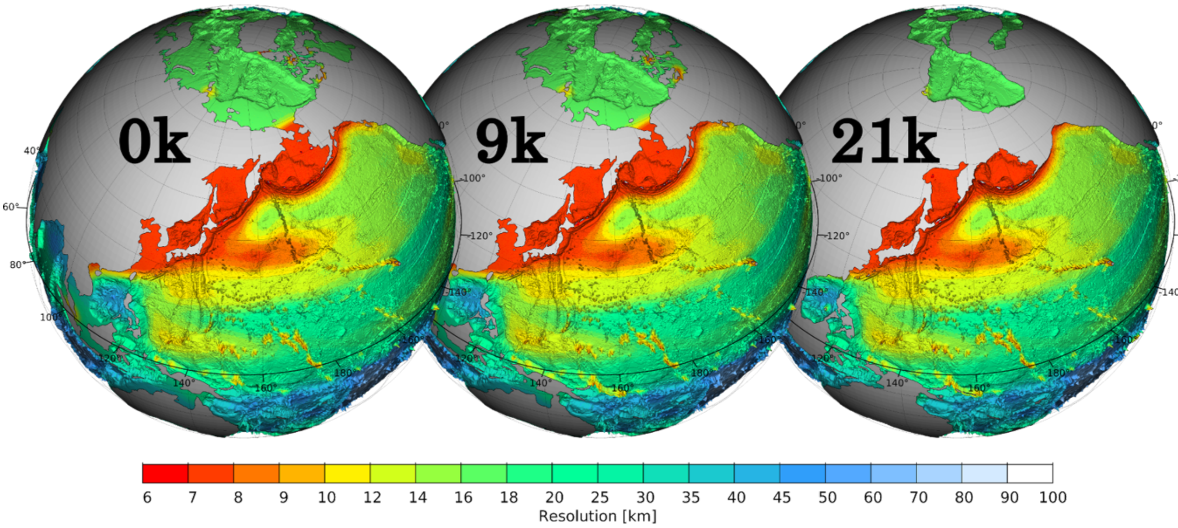

Fig. 1.: Mesh resolution of the northwestern Pacific FESOM configuration for time-slice experiments of today's climate (0k), the early Holocene (9k), and the Last Glacial Maximum (21k). The minimum mesh resolution in the Sea of Okhotsk, in the Sea of Japan and in the Bering Sea is about 6 to 8 km.

Achievements

We've successfully conducted the simulations for the PD, MH, LGM climates with the EH experiment on-going, using the FESOM ocean-standalone modeland on the basis of the grid mesh in Fig. 1. Specifically, our work reached the following two milestones:

- We've created a strategic way in preparing initial fields, coastal and atmospheric forcing for a paleo simulation using FESOM model.
- Using the high-to-6km resolution grid mesh, we successfully simulated the PD, MH and 21ka B.P. oceans to quasi-equilibrium states, and now ready to launch FESOM-REcoM experiments.

Our high-resolution FESOM, MH experiment presents warmer climate compared to the Present-day conditions, while LGM experiment shows much colder surface ocean. This matches our atmospheric forcing and also the paleoceanographic evidences. The simulated warmer North Atlantic of MH refers to a stronger Atlantic Meridional Overturning Circulation (AMOC) compared to the PD, leading to a larger advection of tropical, relatively warmer water northwards (Fig. 2). In parallel, for the same physical constrain, the tropical Atlantic, more saline water is also brought into the subpolar Atlantic Ocean. In comparison, our LGM simulation reveals higher salinities of the LGM ocean globally, due to an intended addition of 1psu into the ocean concerning the 120m-lowered sea level during HS-1. Moreover, pounced increase of sea surface salinities in the Arctic Ocean and subpolar Atlantic Ocean are controlled by the stronger AMOC of LGM, correlated to deepened winter mixed layer depths in the northern North Atlantic Ocean and Nordic Seas (not shown here). Moreover, determined

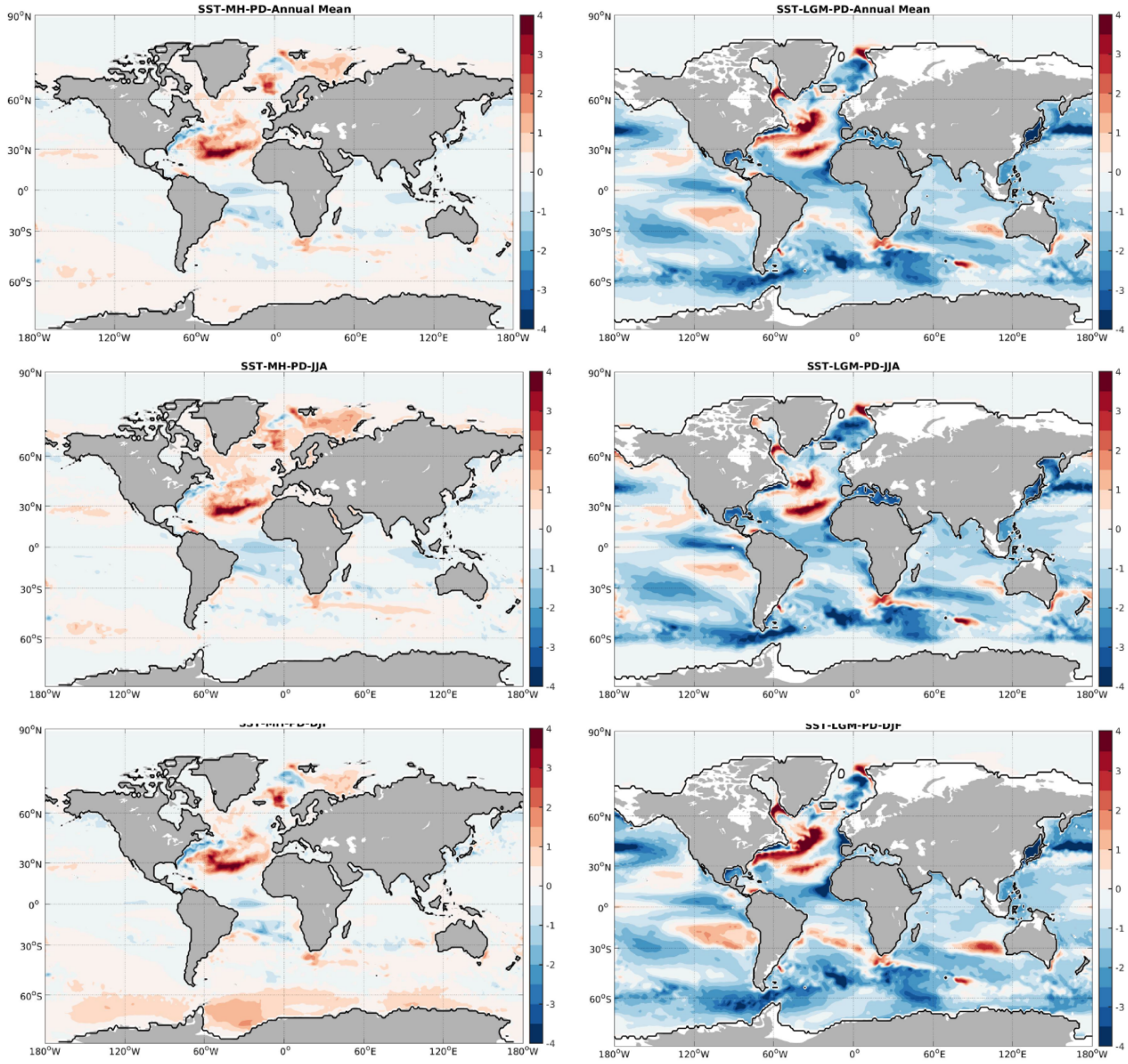

Fig. 2.: FESOM-simulated sea surface temperature (SST) anomalies of the MH and LGM, compared to the PD conditions.

by the extreme cold surface atmosphere, the LGM SSTs are colder than the PD conditions in general, with pronounced lower SSTs due to polar amplification (Fig. 3).

In particular, over the NW Pacific regions where we apply the most high resolutions to 4-6km, the regional sea ice is characterized by significant change from the PI conditions (Fig. 4). Because sea ice is the key factor in regulating surface halocline, we expect strong consequence of its regulation in the North Pacific Intermediate Water (NPIW) formations, and thus North Pacific oxygen minimum zone prevailing to tropical 400m depths. Further analysis will go to this direction.

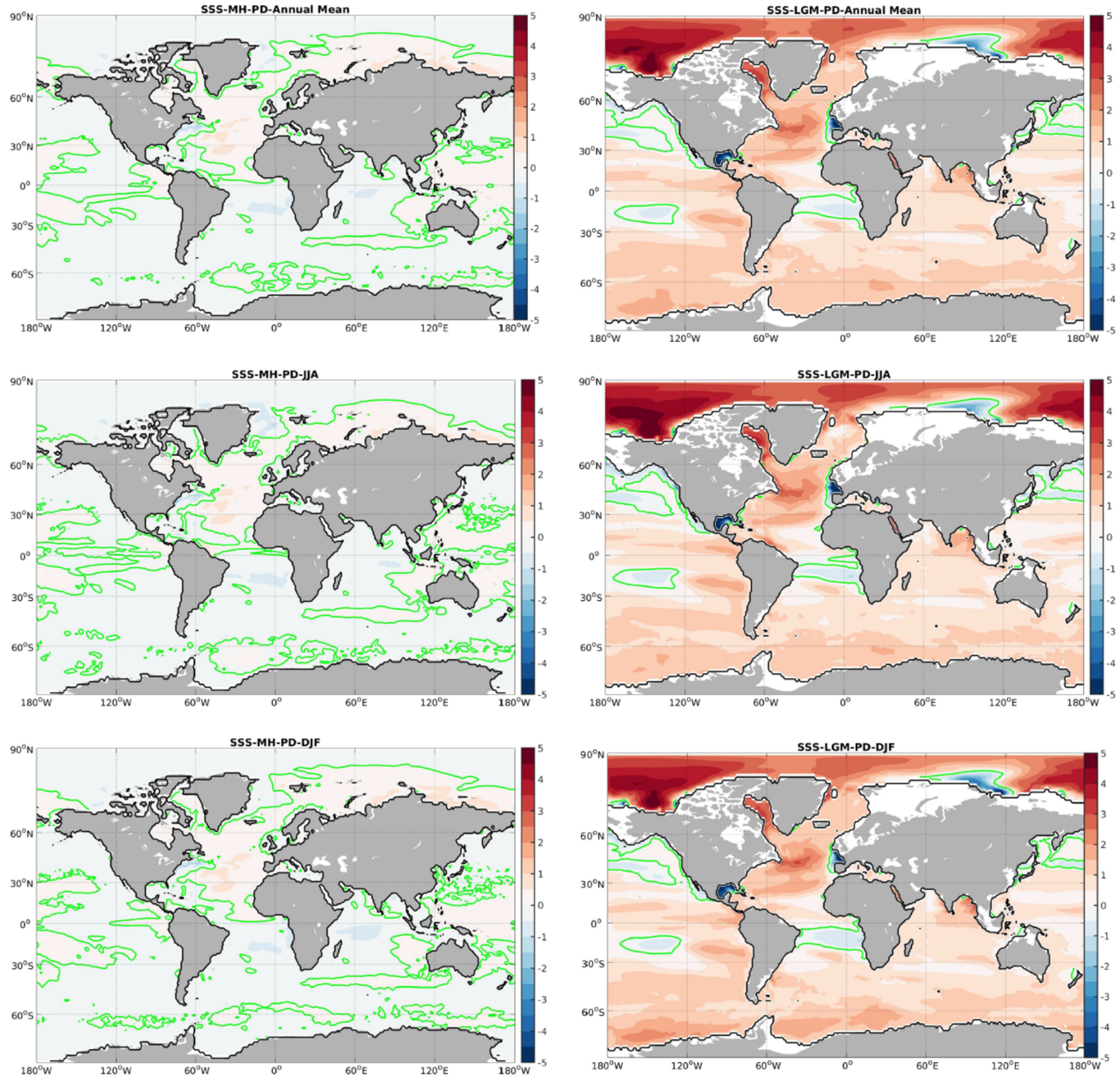

Fig. 3.: FESOM-simulated sea surface salinity (SSS) anomalies of the MH and LGM, compared to the PD conditions.

Perspective of continuation in a following HLRN project

Seceding from our results, our work next step will focus on the following directions:

- To validate the PD experiment, with focus on the surface North Pacific and N-S transect 180E, i.e. throughout the Pacific Ocean.
- To analysis the anomalies of the ocean stratification between PD, MH and LGM.
- A continuation ofthe EH experiment by another 120 years.
- Use the stand-alone FESOM outdata to force the FESOM-REcoM experiment for the four time slides: PD, MH, EH and LGM.

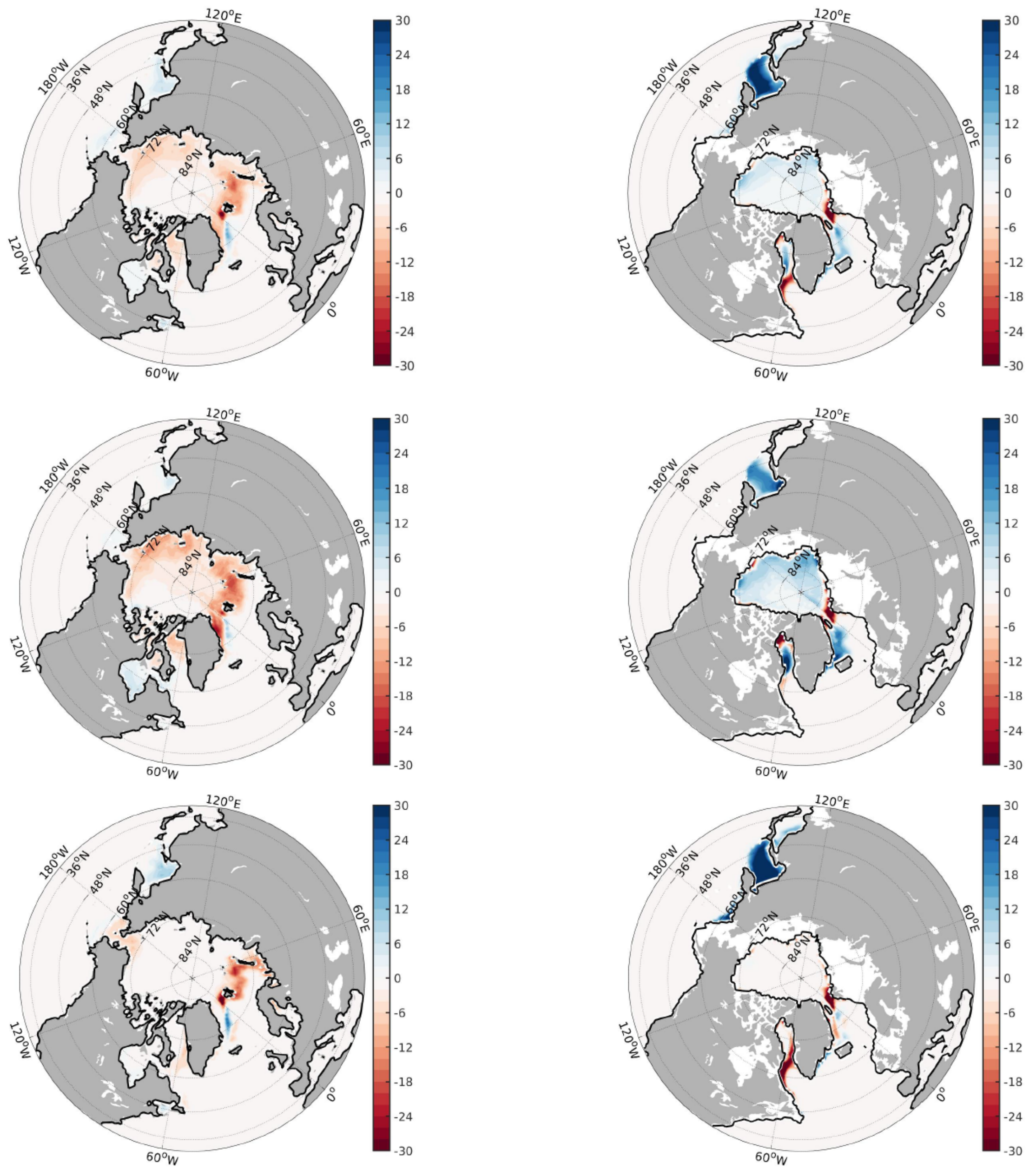

Fig. 4.: FESOM-simulated sea ice concentration (SIC) anomalies of the MH and LGM, compared to the PD conditions.

To finish the following simulation work, we will continue our application to HLRN about computing resource until the end of the BMBF project: *“WTZ China–NOPAWAC-North Pacific Ocean in Warming Climates During the Quaternary”* (01.08.2017 - 31.07.2020). Our next proposal will be submitted by April 28th, 2018.

5.24 *hbp0029:* Carrier dynamics and optical properties of transition metal dichalcogenides

HLRN-Projektkennung:	hbp0029
Laufzeit:	IV/2015 – IV/2018
Projektleiter:	Dr. rer. nat. Michael Lorke Prof. Dr. Frank Jahnke
Projektbearbeiter.	Dr. rer. nat. Alexander Steinhoff Dr. rer. nat. Matthias Florian M. Sc. Daniel Erben
Institut / Einrichtung:	Institut für Theoretische Physik, Universität Bremen

Introduction

Monolayers of transition metal dichalcogenides (TMDCs) are today one of the busiest research areas of semiconductor physics. From a fundamental viewpoint, one of the most intriguing features of TMDCs is the large binding energies and strong optical response exhibited by excitons in these materials. Fascinating prospects arise from the possibility to manipulate Coulomb interaction in atomically thin materials via their dielectric environment. The aim of this project is to investigate carrier dynamics and optical properties of TMDCs using state-of-the-art many-body methods to gauge the potential of devices for light emission.

Results

Excitons versus Electron-Hole Plasma in Monolayer TMDCs

The electronic and optical properties of semiconductors in the presence of excited carriers are strongly determined by many-particle renormalization and screening effects. These effects are very different in an exciton gas than in a plasma of unbound electrons and holes since excitons are more or less neutral compound bosonic particles. Below a critical carrier density, the Mott density, excitons and plasma can coexist in a quasi-equilibrium state. For these reasons, it is highly desirable to quantify the relative importance of excitonic and plasma effects over a wide range of electron-hole excitation densities and to learn how it can be manipulated from the outside.

In publication [1], we show that the thermodynamic balance of excitons and electron-hole plasma can be efficiently tuned via the dielectric environment as well as charge carrier doping. We observe entropy ionization of excitons at low excitation densities and a Mott transition to a fully ionized plasma at high densities between $3\text{x}10^{12}$ cm^{-2} and $1\text{x}10^{13}$ cm^{-2} depending on experimental parameters. Below the Mott transition, excitons become dominant with maximal fractions of excitons between 70 % and more than 99.9 %, see Fig. 1. Moreover, we find that excitonic screening, although two orders of magnitude less efficient than free-carrier screening at comparable excitation densities, plays an important role in the description of the exciton-plasma balance.

We propose the observation of these effects by studying exciton satellites in photoemission and tunneling spectroscopy, which are sensitive to the single-particle spectral functions, thus containing information about the degree of exciton ionization and the extent of exciton wave functions in reciprocal space.

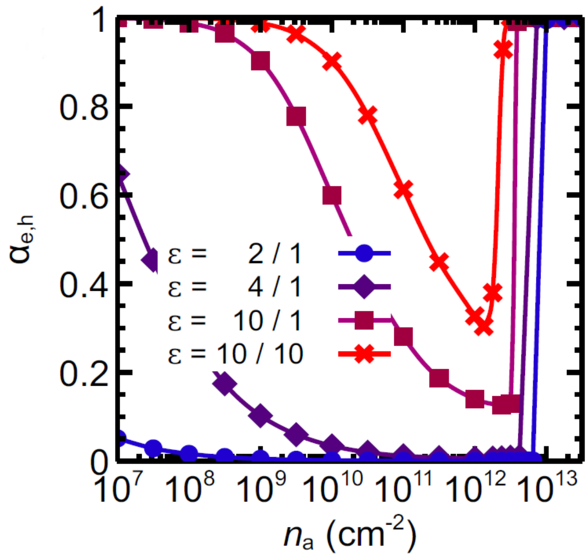

Fig. 1: Degree of exciton ionization at T=300 K for WS_2 in different dielectric environments with dielectric constant ε of bottom/top environment as a function of excitation density n_a, where a denotes electrons or holes.

In general, a fully ionized plasma (α=1) is found above the Mott density, excitons dominate below the Mott density (α=0) and ionization appears again at low densities due to entropy effects. Dielectric screening from the environment is an efficient tuning knob for the degree of ionization due to the strong impact of dielectric screening on the exciton binding energies.

Dielectric Impact of Layer Distances on Trion Binding Energies in van der Waals Heterostructures

Van der Waals heterostructures (vdWH) can be designed by stacking single layers of two-dimensional materials with different properties. vdWH range from commonly investigated single transition metal dichalcogenide (TMD) layers on substrates like hBN or SiO_2 to nearly endless more complex combinations. In the exciting field of two-dimensional materials, they are being heavily investigated with the prospect to design crystals with customized optoelectronic properties.

In publication [2], we provide evidence for the strong impact of the interface between adjacent layers on the optical and electronic material properties. In a simplified picture often suggested in the literature, layers are connected by an ideal plane boundary. However, a finite gap separates the layers in which the density of polarizable medium is reduced due to the mere van der Waals interlayer bonding. As a consequence, field lines passing this gap are more weakly screened in comparison to those passing the adjacent material. Since Coulomb effects are very strong in these materials, the impact of the layer distance both on the band gap and on excitonic binding energies is large.

A direct way to quantify the strength of the Coulomb interaction between carriers is given by the trion binding energy, here understood as the energetic separation between the exciton and the charged exciton transitions in semiconducting TMDs. By combining spectroscopic measurements of trion binding energies in high-quality TMDs on various substrate combinations with a solution of a three-particle Schrödinger equation based on the full GW band structure, we provide quantitative evidence for the sensitivity of the Coulomb interaction to the interlayer gap.

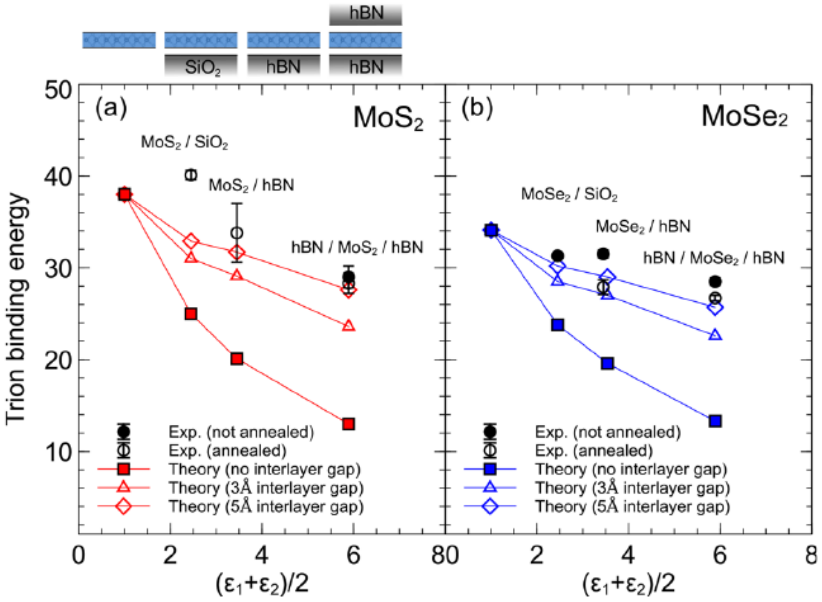

Fig. 2: Trion binding energies determined from experiment for different vdWH before (closed symbols) and after (open symbols) annealing are shown together with theoretical results that have been obtained for corresponding structures and accounting for different sizes of interlayer gaps.

Outlook

Ongoing work is concerned with the impact of competing exciton and plasma phases on the optical properties of atomically thin TMDCs, including excitation-induced dephasing of optical transitions as well as optical gain.

Publications

1. A. Steinhoff, M. Florian, M. Rösner, G. Schönhoff, T. O. Wehling, F. Jahnke, *Exciton fission in monolayer transition metal dichalcogenide semiconductors,* Nature Communications **33**, *1166 (2017)*
2. M. Florian, M. Hartmann, A. Steinhoff, J. Klein, A. W. Holleitner, J. J. Finley, T. O. Wehling, M. Kaniber, C. Gies, Nano Letter *(2018)* DOI:10.1021/acs.nanolett.8b00840

5.25 *hbp0030:* Correlation Effects in strongly correlated crystals: From ab-initio to model studies

HLRN Project ID:	hbp00030
Run time:	IV/2015 – III/2017
Project Leader:	Prof. Dr. Tim Wehling
Project Scientists:	Malte Schüler, Elham Khorasani
Affiliation:	Institut für theoretische Physik, Bremen Center for Computational Physics

Overview

The metal-insulator transition (MIT) in vanadium dioxide (VO_2) between rutile-type (R) and monoclinic-type (M1) is a highly discussed topic in both theoretical and experimental condensed matter physics. It is accompanied with significant changes in the structural, electronic and optical properties, which can be triggered by different external stimuli (thermal, electrical, or optical) near room temperature. Because the MIT is associated with changes in the electrical resistance over several orders of magnitude, VO_2 appears as very promising material, e.g., for sensor applications. Since both electron correlations and lattice deformation play a role in the MIT, VO_2 has become a model system for investigating the complex physics of metal insulator transitions from the viewpoint of fundamental theory. Over the last years, two mechanisms have been proposed: in the Mott-Hubbard picture, a pure electronic mechanism, electron-electron correlations cause the MIT, while in the Peierls picture, a temperature-driven mechanism (due to crystalline lattice deformations) induces it.

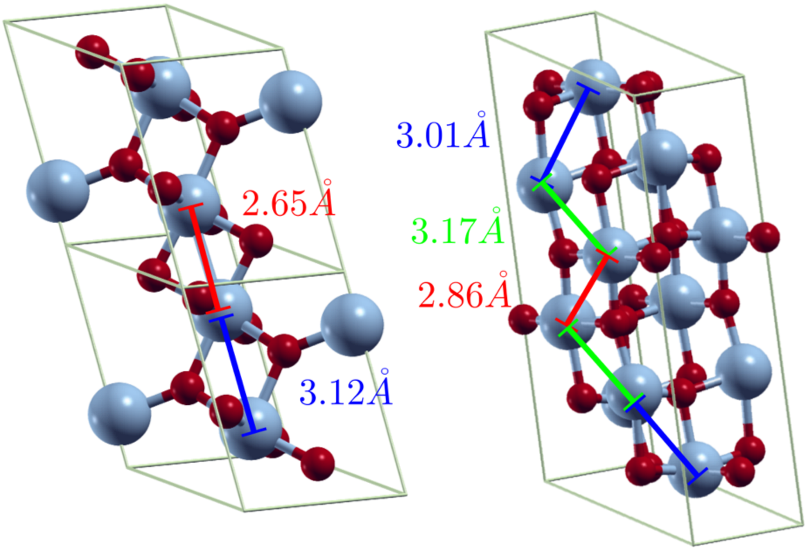

Fig. 1: Schematic of VO_2 in the M1 phase (left) and the high-temperature B-phase (Right). Vanadium ions are shown as gray spheres; small red spheres represent oxygen ions.

The phase diagram of VO_2 is very complex and comprises further phases such as the so-called metastable B-phase. VO_2(B) exhibits a metal-insulator transition somewhat below room temperature. While the MIT across the B-phase VO_2 has been studied by a few theoretical and experimental methods, the role of electron correlations, in triggering the MIT between the low temperature and high temperature phases has remained elusive. We concentrate on VO_2 in

M1 and B phase and investigate how structural changes alter the electronic structure and especially the effects stemming from electronic correlations. We perform LDA+DMFT calculations in order to grasp the electronic correlation effects and structural complexity of VO_2 on equal footing.

Results

We have accomplished LDA+DMFT calculations for the R-phase, which where meant to benchmark our implementation with respect to results published by Tomczack et al. (2007). We have used an implementation of the continous time quantum Monte Carlo (CT-QMC) algorithm in the software library TRIQS [https://triqs.ipht.cnrs.fr/1.4/applications/cthyb/]. We indeed successfully reproduced the calculations, which is presented in terms of the spectral function in Fig. 2. Since CT-QMC works on imaginary times, spectral information on the real axis (as shown in Fig. 2) has to be obtained through an analytic continuation, which limits the resolution, especially far from the Fermi energy. Our calculations show that VO_2 in R-phase is a correlated metal.

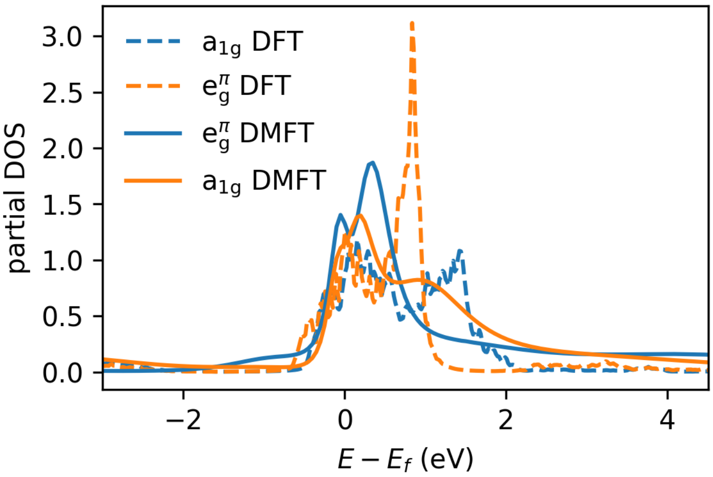

FIG. 2: Partial DOS for R phase for VO_2 as calculated within the DMFT(CTQMC) method. Dashed lines are DFT and solid lines DMFT results.

We have also performed CT-QMC calcutations for the M-phase, where we aimed to benchmark the cluster extension of CT-QMC against the results from Tomczack et al. (2007). It turned out that this problem is not suitable for a CT-QMC algorithm – in contrast to a Hirsh-Fye QMC approach chosen by Tomczack et al.. We have encountered a serious sign problem which rendered any sensible simulation impossible. We therefore decided to take an alternative approach and to replace the CT-QMC algorithm with an exact diagonalization approach which relies on a discretization of the continuous bath hybridization function by a small number of bath states. This is done via fitting of the bath hybridization function on imaginary frequencies. A great advantage of this method is the direct access to real frequency properties.

Again, we have benchmarked our implementation of the exact diagonalization approach for the R-phase of VO_2. The resulting spectral function of the local lattice Green function is presented in Fig. 3. A shrinkage of the band-width, i.e. localization due to interaction effects, can be nicely seen. We find qualitative agreement with the CT-QMC result. A comparison between CT-QMC and exact diagonalization for R-phase is of great important, in order to understand the implications of the different approximations made. Importantly, the resolution of the spectal function in Fig. 3 is the same for the DFT and the DMFT spectral function.

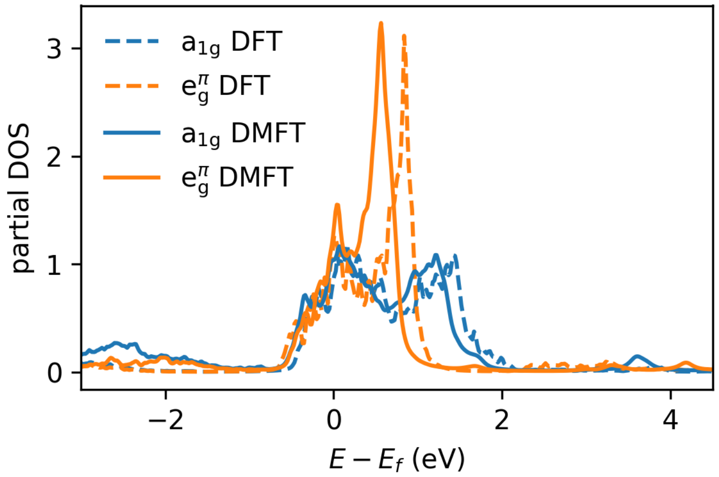

FIG. 3: Partial DOS forVO_2 as calculated within the DMFT(ED) method. Dashed lines are DFT and solid lines DMFT results.

Outlook

In the next step we plan to tackle the M- and B-phase of VO_2 with our implementation of the exact diagonalization method. We will investigate the role of dimerized and non-dimerized V atoms on correlation effects in the B-phase. Ultimately, we aim to calculate transport properties in order to assess the real world applicability of the metal-insulator transition taking place in the B-phase.

Presentations

1. E. Khorasani, Half-day workshop RTG *"Quantum Mechanical Materials Modelling QM^3"*, April 26, 2017, Bremen

Poster Presentations

1. Kick-off Workshop – RTG, "Quantum Mechanical Materials Modelling QM^3", February 28-March 2, Bremen, Germany.
2. NGSCES 2017: The New Generation in Strongly Correlated Electron Systems, September 4-8, 2017, at ICFO, Barcelona
3. CECAM-Workshop, Charge carrier dynamics in nanostructures: optoelectronic and photo-stimulated processes, October 9 - 13, 2017, Bremen, Germany.
4. Autumn School on Correlated Electrons: The Physics of Correlated Insulators, Metals, and Superconductors, September 25-29, 2017, Jülich, Germany.

5.26 **hbp0035: 3 D Simulation eines Interferometers unter Berücksichtigung optischer Abbildungsfehler für ein Bose-Einstein Kondensat**

HLRN-Projektkennung:	hbp00035
Laufzeit:	I/2017– IV/2017
Projektleiter:	Prof. Dr. Claus Lämmerzahl
Projektbearbeiter.	Dr. Ertan Göklü, Janis Roßkamp
Institut / Einrichtung:	Universität Bremen/ZARM

Überblick

In einem klassischen Interferometer wird ein Lichtstrahl in zwei Strahlen aufgeteilt, die einen unterschiedlichen Weg zurücklegen, bevor sie anschließend überlagert werden und interferieren. Das Interferenzmuster ist abhängig vom Gangunterschied der Lichtstrahlen. Dadurch können kleine Änderungen zwischen den Weglängen der beiden Strahlen detektiert werden.

Nach dem Welle-Teilchen Dualismus hat Materie Welleneigenschaften, sodass die Lichtstrahlen in einem Interferometeraufbau durch Atome (bzw. Materiewellen) ersetzt werden können. Die Rolle der Strahlteiler und des Spiegels werden durch Laser übernommen. Diese Art von Interferometern werden Atominterferometer genannt. Die Sensitivität von Atominterferometern wird stetig verbessert, sodass diese eine große Rolle bei Hochpräzisionsmessungen von physikalischen Größen spielen.

Neben Messungen von fundamentalphysikalischer Größen wie der Feinstrukturkonstante oder der Gravitationskonstante, können Atominterferomter auch als Gravimeter und Gyroskop verwendet werden. Hochpräzise Messungen erfordern eine genaue Kenntnis über systematische Effekte, die die Interferometerphase beeinflussen.

Einer der größten unbekannten Effekte ist der Einfluss optischer Abbildungsfehler der Laser auf die Messung. Diese werden durch optische Elemente, wie beispielsweise Spiegel erzeugt.

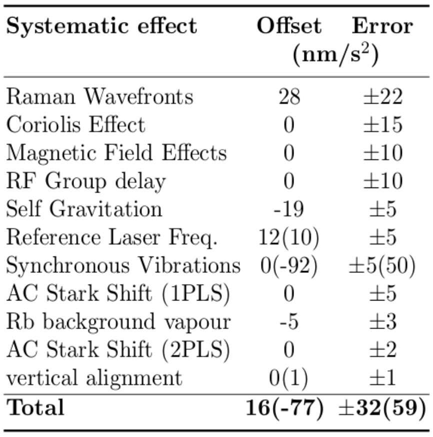

Systematic effect	**Offset**	**Error**
	(nm/s^2)	
Raman Wavefronts	28	±22
Coriolis Effect	0	±15
Magnetic Field Effects	0	±10
RF Group delay	0	±10
Self Gravitation	-19	±5
Reference Laser Freq.	12(10)	±5
Synchronous Vibrations	0(-92)	±5(50)
AC Stark Shift (1PLS)	0	±5
Rb background vapour	-5	±3
AC Stark Shift (2PLS)	0	±2
vertical alignment	0(1)	±1
Total	**16(-77)**	**±32(59)**

Tabelle 1: Liste systematischer Effekte, wobei die größte Messungenauigkeit durch Phasenfehler verursacht wird. Aus C. Freier et al. Mobile quantum gravity sensor with unprecedented stability, Journal of Physics: Conference Series 2016

Modifizierte Zielsetzung

Im Jahr 2016 wurde in diesem Projekt der Einfluss kleinskaliger Phasenfehler untersucht (siehe Abschlussbericht). Die Phasenfehler wurden dabei zufällig mittels zwei Parameter, Korrelationslänge und Rauheit, erzeugt, da im Experiment i.a. keine detaillierten Kenntnisse über kleinskalige Phasenfehler vorliegen. Es ist daher nur möglich Aussagen über den Einfluss auf die Interferometerphase zu treffen, wenn über viele Realisierungen gemittelt wird.

Zum Zeitpunkt der Fertigstellung des letzten Berichts lagen noch nicht alle Simulationsergebnisse vor, bzw. waren teilweise noch nicht ausgewertet. Nimmt man diese hinzu, so ergibt sich durch die Mittelung über die Realisierungen ein kleinerer Phasenfehler als im letzten Bericht angegeben. Dieser ist vernachlässigbar klein gegenüber der angestrebten Messgenauigkeit der PRIMUS-Apparatur.

Daher wurde die ursprüngliche Zielsetzung modifiziert und (vorerst) von dem Vorhaben abgerückt, Zwei-Spezies Simulationen für kleinskalige Phasenfehler durchzuführen. Stattdessen wurden großskalige Fehler für eine Atomsorte analysiert.

Im Gegensatz zu kleinskaligen Fehlern, führen großskalige Fehler zu einem nicht vernachlässigbaren Beitrag, wie in Tabelle 1 zu erkennen. Dort führen Wellenfrontaberrationen zu Phasenfehlern in den Raman Wellenfronten der Laser und stellen die größte Fehlerquelle dar. In Abbildung 1 sind klein- und großskalige Phasenfehler gegenüber gestellt. Für die Modellierung großskaliger Fehler müssen keine zufälligen Realisierungen erzeugt werden. Stattdessen kann der Einfluss auf die Interferometerphase mittels Zernike-Polynomen beschrieben werden.

Für die Berechnung des Fehlerbeitrages dieser Störungen wurde ein analytisches Modell entwickelt. Eine darauf basierende Näherungslösung schätzt diese Fehler ab und sorgt darüber hinaus für ein besseres physikalisches Verständnis. Dieses analytische Modell ist allerdings nur anwendbar auf eine einzelne Atomsorte; die Behandlung der Dynamik von zwei Atomsorten ist wegen der gegenseitigen Wechselwirkung i.a. viel komplizierter. Daher können die für die Entwicklung des Modells getroffenen Annahmen nicht übernommen werden.

Dies hatte zur Folge, dass am HLRN nun die folgenden Fälle untersucht wurden:

a) Verifikation des analytischen Modells durch Simulationen für verschiedene Interferometer-Setups
b) Simulation von Grenzfällen, die nicht durch das analytische Modell beschrieben werden können und nur mittels numerischer Methoden behandelbar sind.

Diese Schritte waren unabdingbar um (i.) ein besseres Verständnis für auf rein numerischem Wege ermittelten Lösungen für großskaliger Fehler zu erhalten und (ii.) um daraus später Simulations-Code für den Einfluss von großskaligen Fehler auf die Dynamik von Zwei-Spezies Systemen zu entwickeln.

Ergebnisse

Der Einfluss der Phasenfehler auf die Interferometerphase wird durch die Expansion des Wellenpakets verursacht und nimmt somit mit der Interferometerlaufzeit zu. Der Fehler bei der Bestimmung der Interferometerphase wurde daher in Abhängigkeit der Laufzeit T untersucht, indem T zwischen 0 und 50 ms variiert wird. Des Weiteren wurde dieser Fehler in Abhängigkeit von verschiedenen Ordnungen der Zernike-Polynome analysiert.

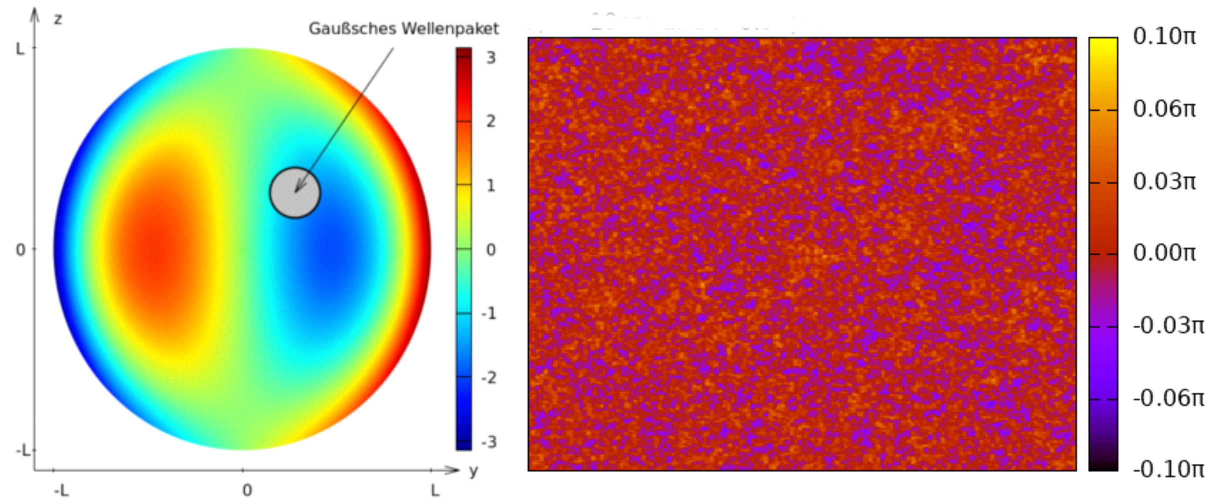

Abbildung 1: Links: großskaliger Fehler (Zernike-Polynom). Rechts: kleinskaliger Fehler (zufällig generiert mit Rauheit und Korrelationslänge)

Ergebnisse zu a)

Für den Laserstrahl und damit für die Zernike-Polynome wird ein Radius L von 1 mm angenommen. Die anfängliche Ausbreitung des Wellenpakets beträgt 10 µm, sodass der Radius der Laserstrahlen sehr viel größer als die Breite des Wellenpakets ist. Die Simulationen wurden für 21 Zernike-Polynome durchgeführt. Exemplarisch sind die Ergebnisse für das Zernike-Polynom in Abbildung 2 dargestellt. In Abbildung 2a) sind die Ergebnisse der analytischen Abschätzung und der Simulation eingetragen. Abbildung 2b) zeigt die relative und absolute Abweichung zwischen beiden Ergebnissen. Es ist zu erkennen, dass die Ergebnisse auch für längere Interferometerlaufzeiten T übereinstimmen. Auch für die übrigen 20 Zernike-Polynome stimmen die Ergebnisse sehr gut überein.

Diese Phasenfehler führen bei einer Messung der lokalen Gravitationsbeschleunigung g zu einem Messfehler in der Größenordnung von und sind damit für Hochpräzisionsmessungen nicht zu vernachlässigen.

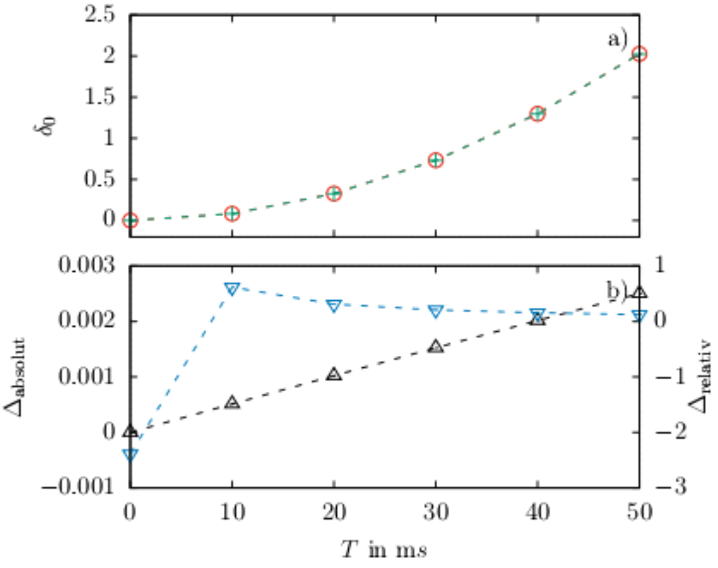

Abbildung 2: Vergleich numerische Simulation und analytische Abschätzung für L=1mm. Numerische Simulation (rot), analytische Näherung (grün), absolute (schwarz) und relative Abweichung (blau)

Ergebnisse zu b)

Nachdem in a) das analytische Modell verifiziert wurde, wird in diesem Abschnitt der Einfluss auf die Interferometerphase für Parameter untersucht, für die die analytische Näherung nicht gültig ist. Dazu wurde der Radius der Zernike-Polynome auf L=50 µm gesetzt. Der Laserradius und die Breite des Wellenpakets liegen dann in der gleichen Größenordnung. Für das Zernike-Polynom sind die Ergebnisse in Abbildung 3 dargestellt. Es ist eine große Abweichung zwischen der analytischen Näherung und der Simulation zu erkennen. Diese Phasenfehler können also nur durch Simulationen untersucht werden.

Bei einer Messung von g führen diese Phasenfehler zu einem Messfehler von und sind damit um 2 Ordnungen größer als die Phasenfehler aus a).

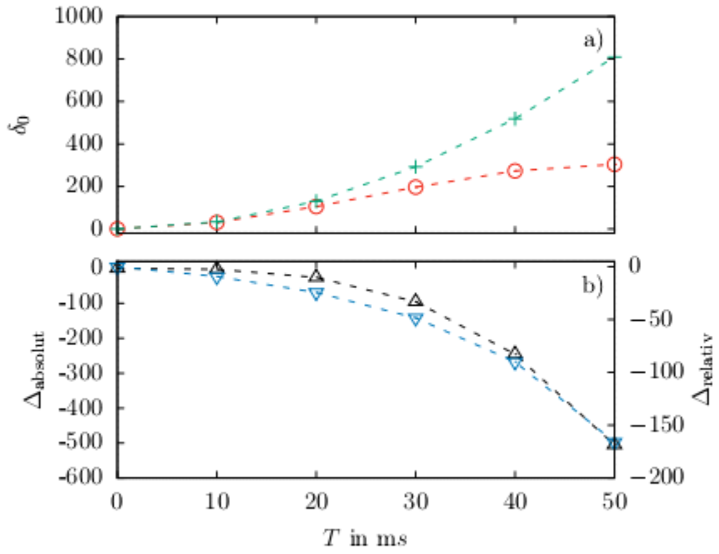

Abbildung 3: Vergleich numerische Simulation und analytische Abschätzung für L=50µm. Numerische Simulation (rot), analytische Näherung (grün), absolute (schwarz) und relative Abweichung (blau)

Ausblick

Der Einfluss von großskaligen Abbildungsfehlern auf die Phase von Atominterferometern ist untersucht worden. Mit den daraus gewonnenen Kenntnissen können nun Zwei-Spezies Atominterferometer betrachtet und der Einfluss der Phasenfehler analysiert werden. Dazu müssen insbesondere die Wechselwirkungen zwischen beiden Atomsorten berücksichtigt werden, da diese die Expansion der Wellenpakete beeinflusst. Die Expansion ist nämlich die Ursache für den Einfluss der Phasenfehler auf die Interferometerphase.

Publikationen

- J.H. Roßkamp, *Auswirkung von optischen Abbildungsfehlern auf die Phase von Atominterferometern,* Master, Universität Bremen, 2018
- Veröffentlichung in Vorbereitung

5.27 hbp0038: Elektronische und Optische Eigenschaften von Halbleiter-Quantenpunkten

HLRN-Projektkennung:	hbp00038
Laufzeit:	II/2017 – I/2018
Projektleiter:	Dr. Michael Lorke
Projektbearbeiter.	Christian Carmesin, Dr. Stephan Michael, Dr. Matthias Florian
Institut / Einrichtung:	Institute for Theoretical Physics, University of Bremen

Motivation

Eine der Herausforderungen der Quanteninformationstechnologie ist die Realisierung deterministischer Einzelphotonenquellen mit hoher Wiederholungsrate und einstellbarer Emissionsenergie [1].

Selbstorganisierte Quantenpunkte (QDs) sind vielversprechende Kandidaten aufgrund des Vorteils der Integrierbarkeit in elektrische Bauteile [2-3].

Zu den aktuellen Herausforderungen gehört die systematische Erweiterung der Emissionsenergien in die verlustarmen Telekom-Bänder bei 1.3 µm und 1.5 µm [4].

Unser Ziel ist es, ein neues und vielversprechendes Materialsystem von InAs/ InAlGaAs/InP-basierten QDs (s. Abb. 1) zu charakterisieren und dominante Beiträge zum Zusammenhang zwischen Morphologie und optischen Eigenschaften zu identifizieren.

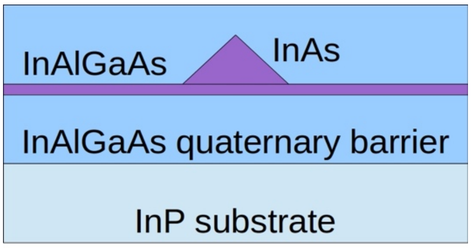

Abb. 1: Schema der verschiedenen Schichten beim Wachstum neuartiger InAs/InAlGaAs/InP-basierter QDs für die Emission im Telekom-Bereich.

Die theoretischen Untersuchungen im Rahmen dieses Projektes wurden in enger Kooperation mit der Arbeitsgruppe von Prof. Dr. Reithmaier aus Kassel (Probenherstellung, optische Charakterisierung) sowie der Arbeitsgruppe von Prof. Dr. Andreas Rosenauer aus Bremen (Transmissions-Elektronen-Mikroskopie (TEM) -Charakterisierung der Proben) durchgeführt, um die elektronischen und optischen Eigenschaften von InAlGaAs-Quantenpunkten systematisch zu analysieren.

Methoden und Ergebnisse

Für elektronische Zustandsberechnungen von Halbleiter-QDs, werden häufig sowohl Kontinuumsmodelle als auch atomistisches TB verwendet. Da die experimentellen Untersuchungen eine TEM Charakterisierung eines einzelnen QDs mit atomarer Auflösung beinhalten, haben wir uns für einen atomistischer TB-Ansatz zur Modellierung entschieden.
Die hierfür verwendete Geometrie ist in Abb. 2 zusammengefasst.

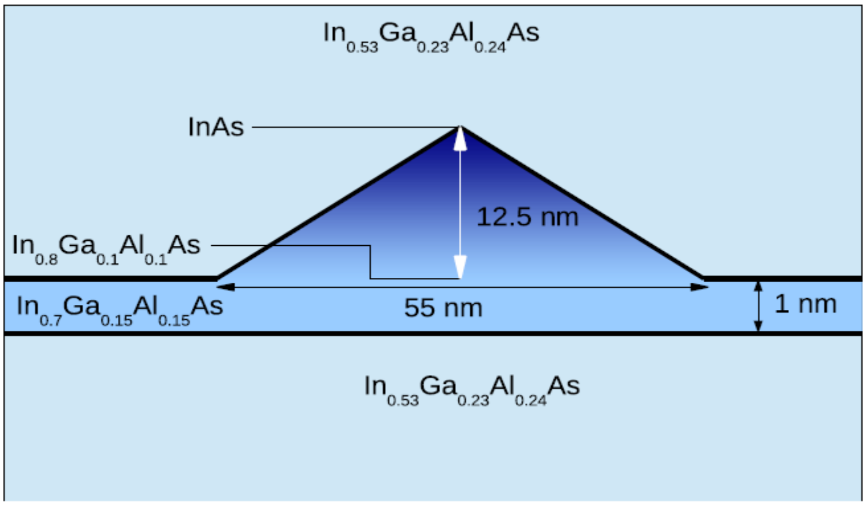

Abb. 2: Geometrie entsprechend der experimentellen Characterisierung. Der pyramidale QD befindet sich auf einer wenige Atome dünnen Benetzungsschicht und zeigt eine linear ansteigende In-Konzentration von unten (helles blau) nach oben (dunkles blau), während die Ga- und Al- Gehalte entsprechend abnehmen. Die Benetzungsschicht hat eine Höhe von 1 nm und einen reduzierten In-Gehalt gegenüber dem Boden des QD. Das QD-Benetzungsschichtsystem ist in ein quaternäres Barrierenmaterial mit einer noch kleineren In-Konzentration (hellblau) eingebettet.

Für die in Abb. 2 dargestellete Struktur wurde zunächst das Verspannungsfeld anhand der Valence-Force-Field-Methode berechnet (s. Abb. 3).

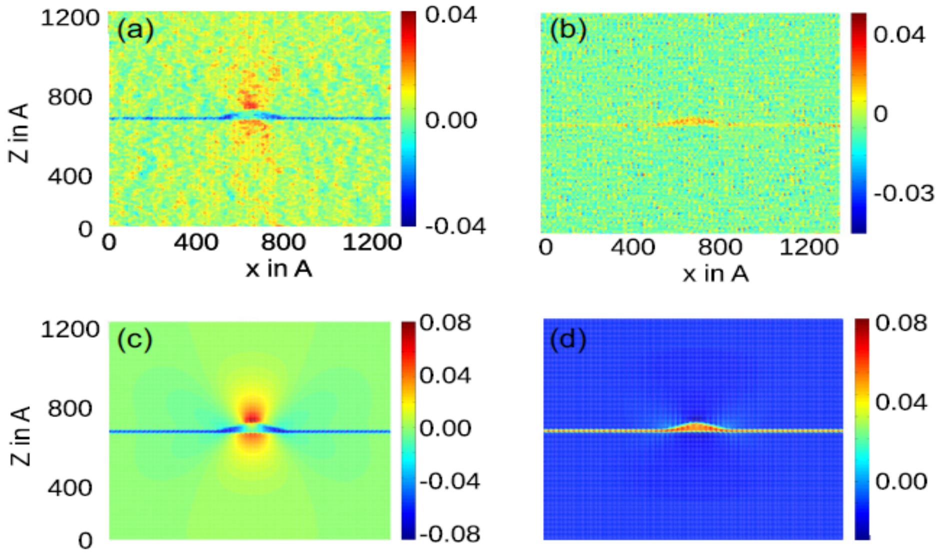

Abb. 3: (a) und (b) Berechnete Verspannungs-komponenten entlang eines Querschnitts durch das Zentrum des untersuchten quaternären QDs. (c) und (d) Verspannungs-komponenten für einen binären InAs/GaAs QD der gleichen Größe und Form zum Vergleich.

Dabei werden sowohl die Bindungslängen als auch die Bindungswinkel verändert und neue Atompositionen berechnet. Aufgrund der ausgelenkten Atompositionen entsteht ein Verspannungsfeld, das über eine verallgemeinerte Harrison-Regel in das Tight-Binding-Modell als Modifikation der Kopplungsmatrixelemente einfließt. Das Tight-Binding-Modell bildet auf einem atomaren Gitter die experimentell bestimmte Geometrie des Quantenpunktes ab, wobei der Einbau von In-Atomen durch konkrete zufällige Realisierungen gemäß dem aus TEM-

Untersuchungen bestimmten Konzentrationsprofil berücksichtigt wird. Dabei wird an jedem atomaren Gitterplatz ein Satz lokalisierter orbitaler Basisfunktionen mit je zwei Spinrichtungen sowie Spin-Orbit-Kopplung berücksichtigt. Die Diagonalisierung des Tight-Binding-Hamiltonians liefert die Eigenenergien und Eigenzustände der gebundenen Elektronen- und Loch-Zustände im QD. Die Energiedifferenez zwischen dem tiefsten gebundenen Elektron und Loch definiert die Quasiteilchen-Bandlücke.

Ausgehend von der in Abb.2 dargestellten Struktur haben wir die Einflüsse von Größen- und In-Konzentrationsschwankungen auf die Emissionsenergie untersucht. Für die Analyse von Größenfluktuationen haben wir in verschiedenen Rechnungen einzelner QDs die Größe variiert, indem jeweils ein konstantes Verhältnis von Durchmesser zu Höhe für jeden QD beibehalten wurde.

Für eine Analyse der Konzentrationsfluktuationen haben wir in verschiedenen Berechnungen für einzelne QDs die In-Konzentration an der Basis des QDs variiert, wobei die Größe unverändert blieb. Hierbei nahm bei jeder Berechnung die In-Konzentration linear zu bis 100% an der Spitze, während Ga und Al gleichmäßig auf die verbleibenden Kationgitterplätze verteilt wurden. Die Ergebnisse zu dieser Untersuchung sind in Abb 4. dargestellt.

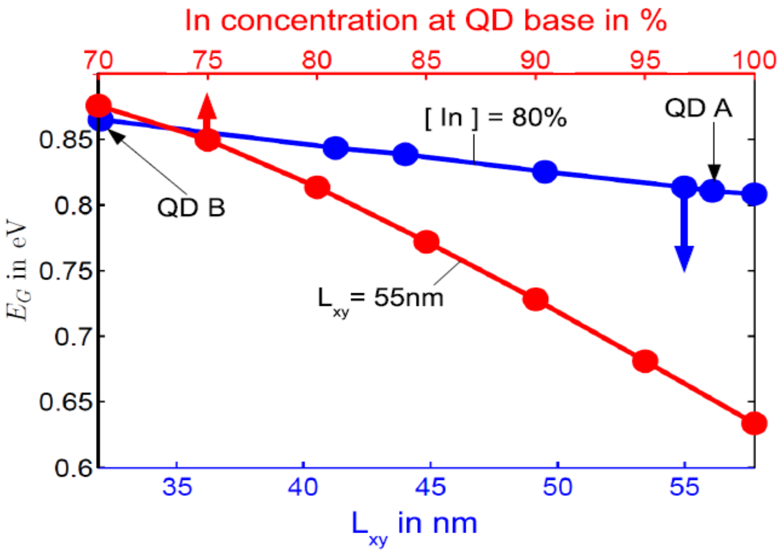

Abb. 4: Variation der Quasiteilchen-Bandlücke E_G für verschiedene QD Seitenlängen der rechteckigen Basis mit konstantem Verhältnis von Durchmesser zu Höhe (untere Achse) und für verschiedene In-Konzentrationen (obere Achse) an der Basis der Pyramide.

Man erkennt, dass Konzentrationsfluktuationen (rot) einen erheblichen Einfluss auf die Übergangsenergien hatten, wogegen, die Größenfluktuationen (blau) einen vergleichbar geringen Einfluss zeigten.

Der Grund für den vergleichsweise geringen Einfluss der Größenfluktuationen ist, dass es sich um einen relativ großen Quantenpunkt mit einem Durchmesser von 55nm an der Basis handelt. Für solche vergleichsweise großen Quantenpunkte ist nicht zu erwarten, dass Größenfluktuationen von +-10% einen erheblichen Einfluss auf die Emissionsenergie haben. Dies kann intuitiv mit dem einfachen Potenzialtopf-Modell veranschaulicht werden, bei dem der Einfluss der Emissionsenergie mit mit dem Radius r abnimmt. Legt man dieses vereinfachte Modell zugrunde, so entspricht die Situation des relativ großen Quantenpunktes der Asymptote der $1/r^2$ Abhängigkeit des Potentialtopf-Modells.

Der relativ starke Einfluss der In-Konzentration kann zusätzlich damit veranschaulicht werden, dass sich die Bandlücken von InAs (~0.5eV) und die von AlAs (~3.0eV) sowie GaAs (~1.3eV) relativ stark unterscheiden und somit der In-Anteil im Quantenpunkt die Emissionsenergie maßgeblich beeinflusst.

Für das Emissionsspektrum des vorliegenden Quantenpunktensembles, das aus selbstorganisiert gewachsenen Quantenpunkten mit unterschiedlichen Größen und In-Konzentrationen besteht, bedeuten die Ergebnisse, dass Änderungen der Emissionsenergie durch starke Größenfluktuationen und bereits geringe Konzentrationsfluktuationen hervorgerufen werden können.

Da für die Quanteninformationstechnologie eine scharfe Emission im Telekom Band eine wichtige Eigenschaft darstellt, ist es von Interesse die Einflüsse auf die Emissionsenergie der Quantenpunkte zu untersuchen und zu verstehen.

Ausblick

In einem Folgeprojekt ist geplant, die im Rahmen dieses Projektes entwickelten Methoden, Erkenntnisse und Untersuchungsabläufe auf ein alternatives Materialsystem für den Telekombereich mit geringeren Konzentrationsfluktuationen anzuwenden.

Publikationen

C. Carmesin, M. Schowalter, M. Lorke, D. Mourad, T. Grieb, K. Müller-Caspary, M. Yacob, J. P. Reithmaier, M. Benyoucef, A. Rosenauer, and F. Jahnke, Phys. Rev. B 96 (2017) 235309

Literatur

[1] Z. Y. Zhang, A. E. H. Oehler, B. Resan, S. Kurmulis, K. J. Zhou, Q. Wang, M. Mangold, T. Süedmeyer, U. Keller, K. J. Weingarten, and R. A. Hogg. *1.55 µm inas/gaas quantum dots and high repetition rate quantum dot sesam mode-locked laser.* Scientific Reports, 2, 2012.

[2] Dieter Bimberg, Marius Grundmann, and Nikolai N Ledentsov. *Quantum dot heterostructures*. John Wiley & Sons, 1999

[3] Zhiliang Yuan, Beata E Kardynal, R Mark Stevenson, Andrew J Shields, Charlene J Lobo, Ken Cooper, Neil S Beattie, David A Ritchie, and Michael Pepper. *Electrically driven single-photon source*. Science, 295(5552):102-105, 2002

[4] L. Brusberg, C. Herbst, M. Neitz, H. Schröder and K. D. Lang, in 2014 The European Conference on Optical Communication (ECOC) (2014), pp. 1–3, ISSN 1550-381X.

5.28 hbp0041: Multi-Messenger Signals from compact Objects

HLRN Project ID:	hbp00041
Run time:	I/2017 – IV/2018
Project Leader:	Prof. Dr. C. Lämmerzahl, Prof. Dr. S. Rosswog
Further collaborators:	Davide Gizzi, Lorenzo Native, Emilio Tejeda
Affiliation:	ZARM, Universität Bremen; Oskar Klein Centre for Cosmoparticle Physics, Stockholm University, Stockholm, Sweden

Overview

- Mergers of two compact objects (neutron stars or black holes) are the prime targets of existing **gravitational wave** detectors. Four decades of preparatory work were crowned in 2015 with the first detections of merging binary black holes. In August 2017, the merger of two neutron stars was observed, both in gravitational and electromagnetic waves. This first **"multi-messenger" detection** conclusively settled several questions that have puzzled astrophysics for decades. For these reasons the event was celebrated as the "Breakthrough of the year 2017" by the Science Magazine.
- The event confirmed in particular that neutron star mergers are the major production site of the **heaviest elements in the Universe** (like platinum, gold or uranium), as predicted by one of the PIs of this project (SR).
- The **electromagnetic emission** that was observed helped to localize the event and it was consistent with our earlier predictions that were obtained via simulations on HLRN. Our recent HLRN simulations have helped to give a physical interpretation to the recently observed events.

Introduction

Stars with more than eight solar masses end their lives in cataclysmic fireworks called supernovae. During theexplosion their luminosity rivals those of whole galaxies. Supernovae eject most of their mass into space where it forms the basis for the next generation of stars. The stellar centres, however, become enormously compressed and – if the star was not too massive – the explosion produces a neutron star, or otherwise a black hole of a few solar masses. Neutron stars can be thought of as gigantic atomic nuclei: with a mass of about 1.4 solar masses and radii of only 12 km their central densities substantially exceed the density in atomic nuclei ($\rho_{nuc} = 2.7 \times 10^{14}\, gcm^{-3}$).

In some cases two such exotic stars orbit as a binary system around their common centre of mass. Due to their enormous compactness, such stars can revolve around each other at very small separations and in such systems strong-field gravity effects become important, making such systems excellent laboratories to test theories such as Einstein's theory of General Relativity. In fact, the first – though indirect – evidence for the existence of gravitational waves came exactly from such a system and it earned its discoverers, Russel Hulse and Joseph Taylor, the Nobel Prize for Physics in 1993. One implication of the emission of gravitational waves is that the binary orbit shrinks further until the stars finally merge. This releases gigantic amounts of gravitational energy, more than the Sun could radiate away during the whole

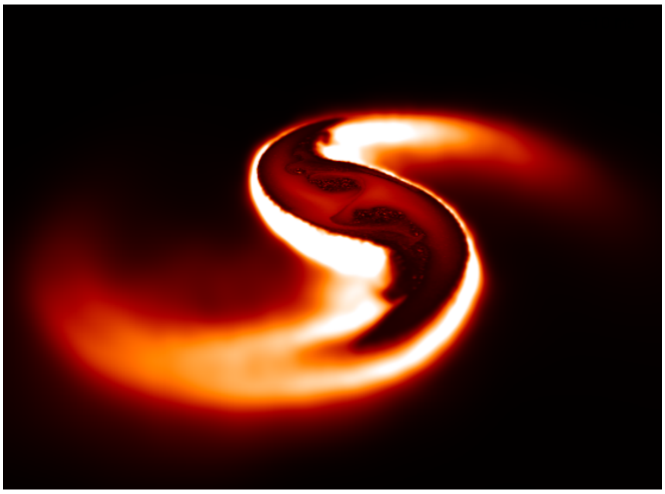

Figure 1: Merger of two 1.2 $M_\odot$ neutron stars. Shown are volume renderings of the density. To allow a view inside, only the lower part of the matter distribution is visualized. From Rosswog et al. (2018b).

lifetime of the Universe. On August 17, 2017 such a neutron star merger has for the first time been detected: the American LIGO detectors recorded the "chirping" (i.e. increasing in frequency and amplitude) gravitational wave signal for about one minute and 1.7 seconds later a short Gamma-ray Burst was detected. During the following weeks fireworks all across the electromagnetic spectrum were observed. This watershed event marks the beginning of the era of multi-messenger astrophysics where event can be observed via two different messengers (photons and gravitons) that convey complementary information. Already the one event revealed: a) mergers of neutron stars emit gravitational waves in agreement with Einstein's General Relativity, b) they cause bright cosmic explosions called Gamma-ray Bursts, c) they forge the heaviest elements in the Universe (such as gold or platinum). Moreover, the delay between the gravitational wave peak and the gamma-ray burst has been used to constrain the speed at which gravitational waves travel: it is equal to the speed of light within one part in 10^{15} !

For these reasons this detection was elected by the Science Magazine as the "Breakthrough of the year 2017".

Recent Results

We have performed a very large set of simulations where we have explored the parameter space of neutron star mergers with unprecedented breadth and numerical resolution. An example of such a simulation is shown in Fig. 1. Such a merger ejects ~ 1% of a solar mass in extremely neutron rich matter. These are ideal conditions for the formation of heavy elements via ``rapid neutron capture''. A major focus in the last year has been this type of element formation and in particular the electromagnetic transients (called "macronovae") that are produced by the radioactive decays of the freshly produced nuclei. We had explored their detectability starting from hydrodynamic simulations that were followed up by nuclear network calculations and the prediction of electromagnetic flashes to finally predict the detectability of such flashes with different instruments in a large study that appeared in May 2017 [5].

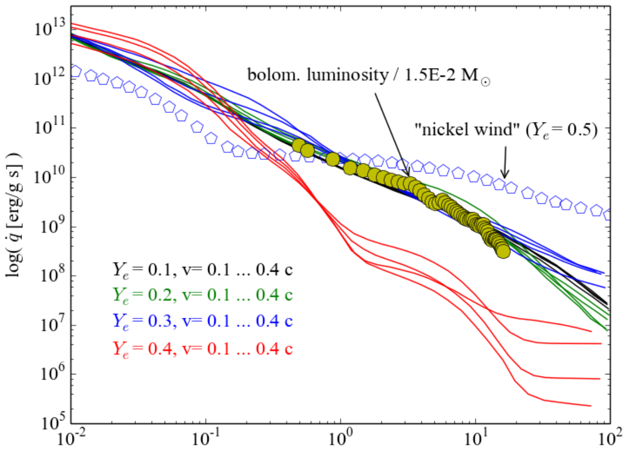

Figure 2: Interpretation of the first neutron star merger detected in both gravitational and electromagnetic waves. To evolution of the total ("bolometric") electromagnetic radiation flow (yellow circles) accurately agrees with the results from "rapid neutron capture" nucleosynthesis calculations (black, blue and green lines). This beautiful agreement proves in particular that neutron star mergers are the major production site of heavy elements in the Universe. For a detailed discussion see Rosswog et al. (2018a).

In August 17 2017 such electromagnetic flashes were detected for the first time in the aftermath of a gravitational wave signal in overall agreement with our theoretical predictions. The decay of the total ("bolometric") lightcurve proves in particular that the heaviest elements in the Universe have been forged in the neutron star collision, see Fig. 2. The detection caused an enormous amount of research activity. To illustrate this, on the day after the official announcement of the event, October 16 2017, more than 80 papers discussing various aspects of the merger event appeared on the preprint archive. Due to this fundamental discovery the major focus of our most recent HLRN simulations was on understanding the specific parameters of this first multi-messenger event. Our recent HLRN simulations have helped to give a physical interpretation to the recently observed events.

Outlook

The era of multi-messenger astrophysics has begun in August 2017. The gravitational wave observatories LIGO/VIRGO are currently being upgraded to higher sensitivity and they are expected to start the next scientific observation run (called "O3") in autumn 2018. In their upgraded version, an even larger cosmic volume will be reachable and one can expect to "harvest" detections at a large rate. The physical understanding of the observations will require a careful comparison against the best available simulation models. In order to be ready for the expected flood of exciting new observations we prepare by further enhancing the degree of realism of our multi-physics simulation tools.

Publications in 2017 resulting from HLRN simulations

[1] *Swift and NuSTAR observations of GW170817: Detection of a blue kilonova.* P. Evans et al., Science 358, 1565 (2017)

[2] *Illuminating gravitational waves: A concordant picture of photons from a neutron star merger,* M. Kasliwal et al., Science 358, 1559 (2017)

[3] *Lanthanides or Dust in Kilonovae: Lessons Learned from GW170817,* C. Gall et al., ApJ 849, L19 (2017)

[4] *The first direct double neutron star merger detection: implications for cosmic nucleosynthesis,* S. Rosswog, et al., arXiv:1710.05445 (2018)
[5] *Detectability of compact binary merger macronovae,* S. Rosswog et al., Classical and Quantum Gravity, 34j4002 (2017)
[6] *Tidal disruptions by rotating black holes: relativistic hydrodynamics with Newtonian codes* E. Tejeda et al., MNRAS 469, 4483 (2017)
[7] The *Properties of Short Gamma-Ray Burst Jets Triggered by Neutron Star Merger* A. Murguia-Berthier et al., ApJ 835, L34 (2017)

Selection of scientific talks where this work was presented

- Plenary talk, Hadrons and Nuclei, German Physical Society; Bochum, March 2018
- Deciphering the Violent Universe; Cancun, Mexico, December 2017
- Piercing the Sphere of Influence; Cambridge, UK, September 2017
- Gravitational Wave Physics and Astronomy; Annecy, France, June 2017
- Nuclear Astrophysics in the Gravitational Wave Era; Trento, Italy, June 2017
- Conference Neutron Star Mergers: from gravitational waves to nucleosynthesis; Hirschegg, Austria, January 2017

5.29 **hbp0045: Non-local manipulation of correlation effects in2D Transition Metal Dichalcogenides**

HLRN Project ID:	hbp00045
Run time:	II/2017 – I/2019
Project Leader:	Prof. Dr. T. O. Wehling
Project Scientists:	C. Steinke, Dr. E. Kamil, J. Berges
Affiliation:	Institut für Theoretische Physik and Bremen Center for Computational Materials Science, Universität Bremen

Overview

Recent theoretical [1] and experimental works [2] have introduced the idea of a novel type of heterojunctions within two-dimensional (2D) materials based on the idea of manipulation of the Coulomb interaction through laterally structured substrates as depicted in Fig. 1. These so called *Coulomb-engineered* heterostructures show spatial property changes, like different band gaps, within an otherwise homogeneous monolayer.

For many applications the band alignment in heterojunctions is important. By means of ab-initio calculations we studied this alignment in Coulomb-engineered transition metal dichalcogenides (TMDCs) for different substrates. We see that we can have different alignments depending on the monolayer and substrate combination. How to manipulate these types of alignment by strain, defects or vacancies is still under investigation.

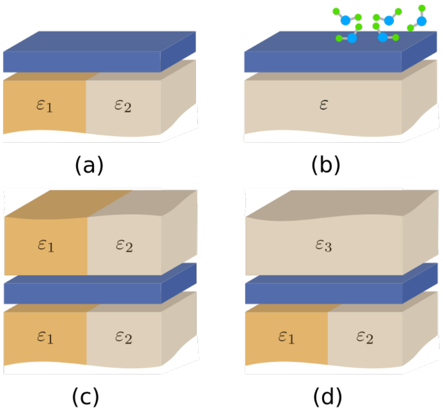

Fig.1: Sketches of a monolayer (blue) in different laterally structured environments.

Not only the band alignment but also effects resulting from the interface of the substrates are of great interest. We study monolayers partially covered with hBN. First calculations show unexpected and interesting results with large effects of edge states of the substrate, which need further studying. As these calculations are numerically very demanding we will apply material-realistic model approaches to understand the effects of spatially changing screening at the interface and away from it in homogeneous monolayers.

Not only in the bulk but also for thicknesses down to the monolayer, metallic TMDCs constitute a prominent showplace for competing many-body instabilities such as superconductivity [3], charge-density waves [4] and magnetism [5] as well as Mott insulating phases [6]. For example, in $NbSe_2$ a coexistence of superconducting and charge order has been found experimentally [7]. In this context, we have shown that even though the observed phase diagrams are complex, the underlying mechanisms are captured by a compact unifying theoretical framework. We apply the *constrained random-phase approximation* (cRPA) [8] and *constrained density-functional perturbation theory* (cDFPT) [9] to the metallic monolayers H-MX_2 with $M \in \{ \text{V, Nb, Ta} \}$ and $X \in \{ \text{S, Se} \}$ and summarize the material specifics with a small number of representative Coulomb and electron-phonon interaction parameters.

Effective lattice models, constructed from available tight-binding Hamiltonians using cRPA and cDFPT parameters, will be further investigated with efficient many-body approaches like Quantum Monte Carlo or Green's function based perturbative schemes. These studies will provide a systematic theoretical description of the emergence of many-body instabilities in the metallic transition metal dichalcogenides.

Results

Coulomb-engineered heterostructures

Substrates can significantly change the quasi-particle band gap due to screening of the Coulomb interaction. When a monolayer is put on top of a laterally structured substrate, there will be regions away from the interface, where its effect becomes small and the system will have „homogeneous“ properties. For instance, when WS_2 is partially capped with graphene, regions with a local band gap of quasi free-standing WS_2 and regions with a reduced band gap due to the screening induced by graphene can be found. In these systems, similar to pn-junctions, the bands have to align in different regions. As the type of heterostructure is very important for practical applications, we investigated the band alignment for different semiconducting TMDCs and substrates. As the tungsten-based semiconductors show a large spin-orbit splitting, spin-orbit coupling is considered for WS_2 and WSe_2. The resulting band positions are shown in Fig 2.

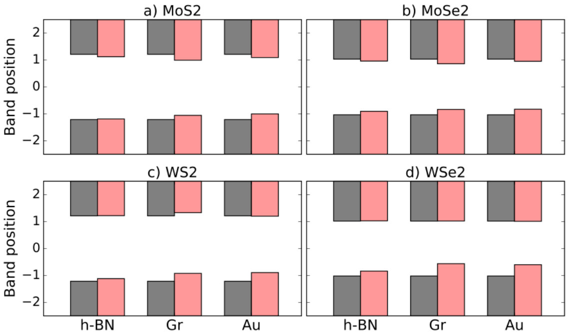

Fig. 2: Band positions at the K-point of different semiconducting TMDCs placed on hexagonal boron nitride (hBN), graphene (Gr) and gold (Au) (red bars) compared to corresponding free-standing monolayers (grey bars).

In all studied systems, the band gap decreases depending on the substrate. In MoS_2 the band alignment always shows a type-I behavior, i.e., the energy of the conduction band is lowered while the energy of the valence band is increased in comparison to free-standing MoS_2. The band gap modulation is smallest for a hBN substrate (~ 100 meV), which is an insulator and thus screens lesser than Au, which shows the largest band gap reduction (~ 300 meV).

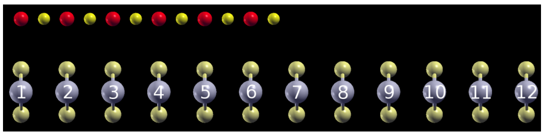

Fig.3 : Side view of supercell with a laterally structured substrate (hBN–vacuum) for MoS_2.

In WS_2 the type of alignment depends on the substrate. For graphene we see a clear type-II heterojunction, whereas for hBN and Au the conduction band is only weakly affected. This is also the case for all chosen substrates for WSe_2. The origin of this behavior still needs to be investigated.

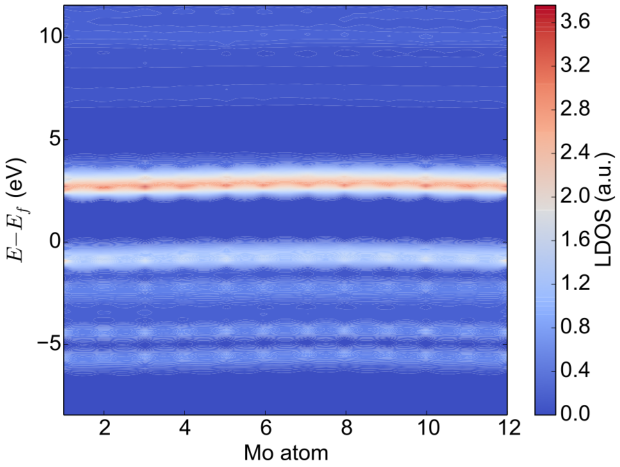

Fig. 4: Spatially resolved local density of states of *d*-orbitals of Mo around the Fermi energy for all Mo-atoms in the supercell. Maxima in the the conduction and valence band of the LDOS correspond to red and light blue areas.

On top of that we started to investigate interface effects in Coulomb-engineered heterostructures. First results of a system with a laterally structured substrate are shown in Fig. 4. Therefore, we considered a supercell consisting of 12 primitive unit cells of MoS_2 with six of them covered with hBN (see Fig. 3). We show the local density of states (LDOS) of the three *d*-orbitals (d_{xy}, $d_{x^2-y^2}$, d_{z^2}) around the Fermi energy for every Mo atom.

Remarkably, there is no clear spatial band gap modulation visible, only a slight bend of the maximum in the conduction band. The quasi-particle band gap seems to be nearly constant through the whole supercell.

These ab-initio results were unexpected as model calculations as well as experimental data show a band gap shift in distance of the interface and need further investigation.

Realistic description of competing interactions in metallic TMDCs

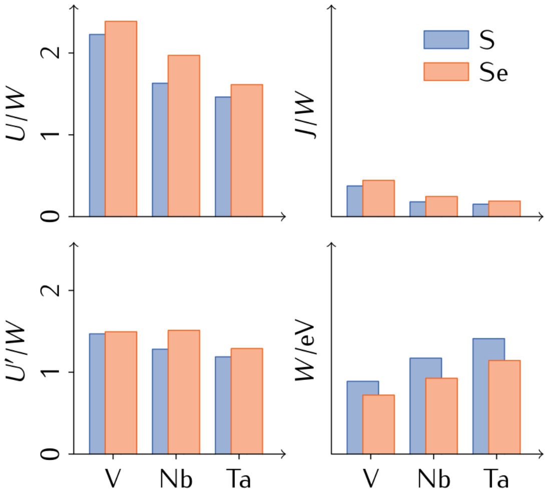

Fig. 5: Kanamori parametrization of the local Coulomb interaction for different TMDCs. *U* and *U′* are the intra- and inter-orbital interactions without exchange while *J* governs inter-orbital processes with exchange. *W* is the electronic bandwidth.

We further used the HLRN computing time to perform calculations pertaining to the constrained random-phase approximation (cRPA) [8] implemented in *VASP* [11] to investigate the metallic monolayer TMDCs. In these materials, the so-called *correlated subspace*, which determines the material specifics, consists of three electronic bands close to the Fermi level with primarily M-d_{z^2}, -d_{xy} and -$d_{x^2-y^2}$ orbital character. An effective lattice model for this subspace was obtained as follows: The Wannier Hamiltonian that reproduces the three bands was constructed using the *Wannier90* [12] package. In a second step, the corresponding partially screened momentum-dependent Coulomb interaction tensor was evaluated within the cRPA. This excludes the screening effects from within the correlated subspace, to be treated later in the process of solving the model.

As an example for these results, in Fig. 5, the cRPA estimation of the screened local Coulomb interaction (minimal parameters through Kanamori parametrization) for all the metallic TMDCs is plotted. It exhibits a systematic behavior of the strength of electronic correlations as one scans through different transition metals and chalcogens in TMDCs.

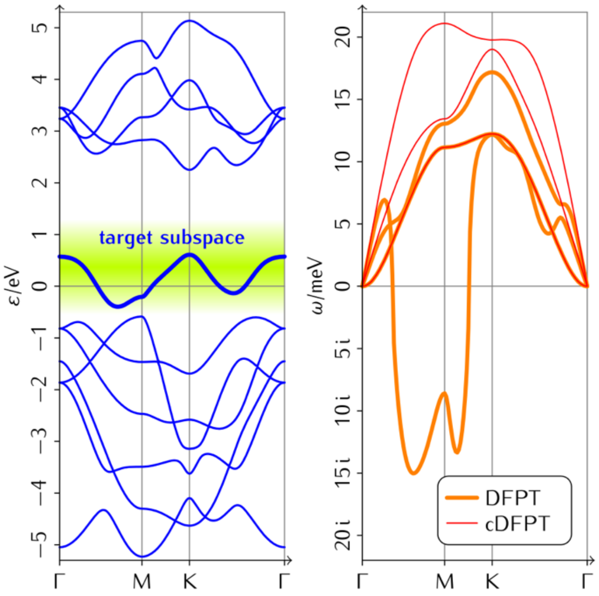

Fig. 6: Application of cDFPT to NbSe$_2$. Left: Electron dispersion. Right: Acoustic phonon dispersion according to (c)DFPT, including (excluding) the response of the target subspace.

Analogous to the aforementioned cRPA method used to calculate the partially screened Coulomb interaction parameters, we recently also use constrained density-functional perturbation theory (cDFPT) to obtain partially screened phonon dispersions and electron-phonon couplings. This promising downfolding method has been introduced in 2015 by Nomura and Arita [9] as a modification of density functional perturbation theory (DFPT) [10] as implemented in *Quantum ESPRESSO* [13] and has only been applied to very few material systems by now.

In Fig. 6, the application of cDFPT is visualized using the example of NbSe$_2$: Regular DFPT yields soft phonon modes, indicating structural instability, which disappear upon exclusion of the metallic band from the electronic response to phononic lattice distortion.

Outlook

As we are the first group calculating these new kind of heterojunctions, we still have to face some challenges to understand the underlying physics. There are two major open topics we want to investigate regarding Coulomb-engineered heterojunctions: Firstly, we want to investigate how to control the band alignment and with that guide experiments towards novel applications. For that, we want to study the impact of strained substrates, defects and vacancies as in experiment crystals are not perfectly grown most of the time. By means of RPA calculations we will examine the dielectric function of the different substrates and systems. Secondly, we want to understand how to describe heterojunctions induced by laterally structured environments and nail down why we see unexpected results in our current calculations. We want to develop new model Hamiltonians which can material-realistically describe these heterojunctions without the need of even larger supercells.

We will also study the effect of screening on the Coulomb interaction as we go from bulk to monolayer thicknesses. This will provide a systematic evidence of whether or not free-standing monolayers are good examples of strongly correlated systems.

Since the effect of screening is reduced in free-standing monolayers, we will also investigate the effect of the environment on the properties controlled by the Coulomb interaction like magnetism and superconductivity.

Presentations

1. Christina Steinke, Malte Rösner, Dmitry Ryndyk, Tim Wehling, *Material Realistic Description of Coulomb-engineered Two-dimensional Materials,* APS March Meeting, Los Angeles, March 8, 2018 and DPG Frühjahrstagung, Berlin, March 16, 2018
2. Gunnar Schönhoff, Malte Rösner, Ebad Kamil, Jan Berges, Tim Wehling, *Realistic Description of Competing Interactions in Metallic TMDCs,* APS March Meeting, Los Angeles, March 8, 2018 and DPG Frühjahrstagung, Berlin, March 15, 2018
3. Ebad Kamil, Jan Berges, Gunnar Schönhoff, Malte Schüler, Tim Wehling, *Theory of Mott physics in 1T-*$NbSe_2$*: An LDA+DMFT study,* APS March Meeting, Los Angeles, March 8, 2018 and DPG Frühjahrstagung, Berlin, March 15, 2018

Posters

1. Gunnar Schönhoff, Malte Rösner, Ebad Kamil, Jan Berges, Tim Wehling, *Competing Interactions in Metallic TMDCs,* ICTP School on Electron-Phonon Physics from First Principles, Trieste, March 20, 2018

References

[1] M. Rösner et al., Nano Lett. **16**, 2322 (2016)
[2] A Raja et al., Nature Communcations **8**, 15251 (2017)
[3] R. F. Frindt, Phys. Rev. Lett. **28**, 299 (1972)
[4] M. M. Ugeda et al., Nature Physics **12**, 92 (2016)
[5] Y. Ma et al., ACS Nano **6**, 1695 (2012)
[6] Y. Nakata et al., NPG Asia Materials **8**, e321 (2016)
[7] X. Xi et al., Nature Nanotechnology **10**, 765 (2015)
[8] F. Aryasetiawan et al., Phys. Rev. B **74**, 125106 (2006)
[9] Y. Nomura et al., Phys. Rev. B **92**, 245108 (2015)
[10] S. Baroni et al., Rev. Mod. Phys. **73**, 515 (2001)
[11] G. Kresse and J. Hafner, Journal of Physics: Condensed Matter **6**, 8245 (1994)
[12] A. A. Mostofi et al., Computer Physics Communications **178**, 685 (2008)
[13] P. Giannozzi et al., Journal of Physics: Condensed Matter **21**, 395502 (2009)